University of Cape Town

The Broad Spectral Energy Distributions of Accreting White Dwarfs

Author:
Tamara Jayne Lancaster

Student Number:
LNCTAM002

December 13, 2022

Abstract

Cataclysmic Variable stars (CVs) are excellent examples of multi-wavelength objects. They have been detected at all frequencies, from radio to γ-ray. However, while large sets of multi-wavelength data exist, few studies have been performed on the broad spectral energy distributions (SEDs) of these objects. I perform such a study here, and present the largest collection of broad CV SEDs yet constructed.

I define a sample of well-studied, nearby cataclysmic variables of several different CV classes, and gather existing multi-wavelength data over a broad frequency domain. I identify the contributions to the spectrum and compare the spectra between classes. I then use the SEDs to constrain the mass accretion rates by modelling the accretion disc as a series of concentric annuli, each of which radiates as a black body with effective temperature appropriate to the radius of that annulus. The resulting best-fit accretion rates are compared to published values of mass accretion rates for the systems.

My method of modelling the emission from a CV accretion disc as a sum of black-bodies produces accretion rate estimates that are reliable to within a factor of 5 for those systems that have steady state discs. However, the data are significantly underfitted by these simple models in all cases.

While this method is a useful tool for modelling spectra and finding accretion rates, it cannot be applied to a small amount of data quickly and simply. It must be performed on as large a dataset as possible, and other contributions to the spectrum must be accounted for. As a result, an attempt to obtain accretion rate estimates for a larger, volume-limited sample of non-magnetic CVs was unsuccessful.

I also investigate the ratios of flux densities in different wavebands. My data reveal two previously reported correlations, namely that shorter period CVs have higher X-ray to optical flux ratios and that magnetic CVs are X-ray bright compared to non-magnetic CVs. In addition, I find that polars are radio bright compared to IPs and non-magnetic CVs, and illustrate this, for the first time.

Acknowledgements

I acknowledge and thank my supervisors, Patrick Woudt[1] and Magaretha Pretorius[2], for their support during the pursuit of this degree. Thanks to Deanne L. Coppejans[3], for providing necessary radio data, and Dante Hewitt[2], for his assistance with coding and equations. Thanks must also go to Dylan Forbes-Wilkinson[4], for his assistance in interpreting my results, and Alexandra Lancaster[5] and Michelle van der Merwe[6], for their support and encouragement during this process.

Financial support for my studies came from the South African Astronomical Observatory, The National Astrophysics and Space Science Programme, and the National Research Foundation.

This publication makes use of data products from the Two Micron All Sky Survey, which is a joint project of the University of Massachusetts and the Infrared Processing and Analysis Center/California Institute of Technology, funded by the National Aeronautics and Space Administration and the National Science Foundation.

I have made use of data products from the Wide-field Infrared Survey Explorer, which is a joint project of the University of California, Los Angeles, and the Jet Propulsion Laboratory/California Institute of Technology, funded by the National Aeronautics and Space Administration

This work is based in part on observations made with the Spitzer Space Telescope, which was operated by the Jet Propulsion Laboratory, California Institute of Technology under a contract with NASA.

This dissertation makes use of data obtained as part of the INT Photometric H Survey of the Northern Galactic Plane (IPHAS, www.iphas.org) carried out at the Isaac Newton Telescope (INT). The INT is operated on the island of La Palma by the Isaac Newton Group in the Spanish Observatorio del Roque de los Muchachos of the Instituto de Astrofisica de Canarias. All IPHAS data are processed by the Cambridge Astronomical Survey Unit, at the Institute of Astronomy in Cambridge. The bandmerged DR2 catalogue was assembled at the Centre for Astrophysics Research, University of Hertfordshire, supported by STFC grant ST/J001333/1.

[1]Department of Astronomy, University of Cape Town

[2]South African Astronomical Observatory, P.O. Box 9, Observatory 7935, South Africa

[3]Department of Astrophysics/IMAPP, Radboud University, P.O. Box 9010, 6500 GL Nijmegen, The Netherlands

[4]Faculty of Humanities, University of Cape Town

[5]Orthopaedic Biomechanics Lab, Division of Biomedical Engineering, Department of Human Biology, University of Cape Town

[6]Department of Geology, Stellenbosch University, South Africa

Contents

Contents **3**

List of Figures **7**

List of Tables **8**

1 Introduction **9**

2 Cataclysmic Variables **12**
2.1 Roche Potential . . . 12
2.1.1 Roche Lobes . . . 13
2.1.2 Roche Geometry . . . 14
2.1.3 Lagrangian Points . . . 14
2.2 Types of Binaries . . . 16
2.2.1 Detached Binary . . . 16
2.2.2 Contact Binaries . . . 16
2.2.3 Semi-Detached Binary . . . 16
2.3 White Dwarfs . . . 18
2.3.1 The Chandrasekhar Limit . . . 19
2.4 Red Dwarfs . . . 19
2.5 Accretion . . . 20
2.5.1 Accretion Disc . . . 20
2.5.2 Keplerian Discs . . . 21
2.5.3 Alpha Disc Model . . . 22
2.5.4 Boundary Layer . . . 23
2.5.5 Bright Spot . . . 24
2.5.6 Disc Circularisation . . . 24
2.5.7 Tidal Effects . . . 24
2.6 Mass Transfer . . . 24
2.6.1 Gravitational Radiation . . . 25
2.6.2 Magnetic Braking . . . 25
2.7 Types of CVs . . . 27
2.7.1 Non-Magnetic CVs . . . 27
2.7.2 Magnetic CVs . . . 30
2.8 Origin of CVs . . . 33
2.9 The Spectral Energy Distributions of CVs . . . 33
2.9.1 White Dwarf . . . 35
2.9.2 Red Dwarf . . . 35
2.9.3 Stellar Spectra . . . 35

2.9.4 Accretion Disc . . . 35
2.9.5 Inclination . . . 39
2.9.6 Boundary Layer . . . 39
2.9.7 Bright Spot . . . 39
2.9.8 Jets . . . 39
2.9.9 Accretion Column . . . 40
2.9.10 Combined Spectrum . . . 41

3 Emission Mechanisms **42**
3.1 Thermal Radiation . . . 42
3.2 Compton Scattering . . . 43
3.3 Inverse Compton Scattering . . . 44
3.4 Bremsstrahlung Radiation . . . 45
3.5 Cyclotron Radiation . . . 47
3.6 Synchrotron Radiation . . . 49

4 Methods **54**
4.1 Data Archives . . . 54
4.1.1 Barbara A. Mikulski Archive for Space Telescopes . . . 54
4.1.2 NASA/IPAC InfraRed Science Archive . . . 55
4.1.3 High Energy Astrophysics Science Archive Research Center . . . 55
4.1.4 XMM-Newton Science Archive . . . 55
4.2 Data Sources . . . 56
4.2.1 *Extreme Ultraviolet Explorer* . . . 59
4.2.2 *Far Ultraviolet Spectroscopic Explorer* . . . 59
4.2.3 *International Ultraviolet Explorer* . . . 59
4.2.4 *Neil Gehrels Swift Observatory* . . . 59
4.2.5 *Berkeley Extreme and Far-ultraviolet Spectrometer* . . . 60
4.2.6 *Wisconsin Ultraviolet Photo-Polarimeter Experiment* . . . 60
4.2.7 *Johns Hopkins Ultraviolet Telescope* . . . 60
4.2.8 *Tübingen Echelle Spectrograph* . . . 61
4.2.9 Two Micron All-Sky Survey . . . 61
4.2.10 *Wide-field Infrared Survey Explorer* . . . 61
4.2.11 *Hipparcos* . . . 61
4.2.12 *Global Astrometric Interferometer for Astrophysics* . . . 61
4.2.13 *Galaxy Evolution Explorer* . . . 62
4.2.14 *Spitzer Space Telescope* . . . 62
4.2.15 Skymapper Southern Sky Survey . . . 62
4.2.16 Panoramic Survey Telescope and Rapid Response System . . . 63
4.2.17 Sloan Digital Sky Survey . . . 63

4.2.18 INT/WFC Photometric H-Alpha Survey of the Northern Galactic Plane . . . 63
4.2.19 UKIRT Infrared Deep Sky Survey . . . 64
4.2.20 Subaru Telescope . . . 64
4.2.21 Visible and Infrared Survey Telescope for Astronomy . . . 64
4.2.22 Palomar Observatory Sky Survey II . . . 65
4.2.23 All Sky Automated Survey for SuperNovae . . . 65
4.2.24 *Röntgensatellit* . . . 65
4.2.25 *X-ray Multi-Mirror Mission* . . . 65
4.2.26 HUNt for Dynamic and Explosive Radio transients with meerKAT 66
4.2.27 Karl G. Jansky Very Large Array . . . 66
4.3 Data Processing . . . 67
4.4 Algorithms . . . 69
4.4.1 Primary Spectra . . . 69
4.4.2 Secondary Spectra . . . 69
4.4.3 Accretion Disc Spectra . . . 69
4.4.4 Parameter Inputs . . . 70
4.4.5 Curve Fitting . . . 71
4.4.6 Uncertainties . . . 73
4.4.7 Goodness of Fit . . . 73
4.4.8 Flux Density Ratios . . . 74

5 A Sample of Well-Studied CVs 75
5.1 Nova-Likes . . . 75
5.1.1 V603 Aql . . . 75
5.1.2 V3885 Sgr . . . 76
5.1.3 IX Vel . . . 77
5.1.4 UX UMa . . . 77
5.2 Dwarf Novae . . . 77
5.2.1 SU UMa . . . 77
5.2.2 U Gem . . . 78
5.2.3 Z Cam . . . 78
5.2.4 SS Cyg . . . 78
5.3 Intermediate Polars . . . 79
5.3.1 DQ Her . . . 79
5.3.2 DO Dra . . . 79
5.3.3 AE Aqr . . . 80
5.3.4 EX Hya . . . 80
5.4 Polars . . . 81
5.4.1 AM Her . . . 81
5.4.2 AR UMa . . . 81

5.4.3 BL Hyi . . . 81
5.4.4 VV Pup . . . 82

6 Results and Discussion **83**
6.1 The Sample for Detailed Study . . . 83
6.1.1 Lightcurves . . . 83
6.1.2 Broad SEDs . . . 88
6.1.3 Accretion Rate Estimates . . . 106
6.1.4 A Comparison of the Spectral Properties between CV Classes 109
6.2 Pala et al. (2020) Volume-Limited Sample . . . 117
6.2.1 SED Fits and Accretion Rate Estimates . . . 118
6.2.2 Absolute Magnitude vs. Orbital Period . . . 126
6.3 Overview of Results . . . 127
6.3.1 A Collection of SEDs . . . 127
6.3.2 Estimates of $\dot{M}$ . . . 127
6.3.3 The Radio to Optical Flux Ratios of Polars . . . 130

7 Conclusions **131**

Bibliography **133**

List of Figures

1 Gravity Wells and Roche Equipotentials . . . 13
2 Roche Equipotentials and the Lagrangian Points . . . 14
3 L_1 Accretion Stream Bottleneck . . . 15
4 Roche Lobes . . . 16
5 Types of Binary Star Systems . . . 17
6 Non-Magnetic Accretion . . . 21
7 Bimodal Period Distribution of Cataclysmic Variables . . . 26
8 Magnetic Braking . . . 28
9 Accretion Column . . . 30
10 Intermediate Polar CV . . . 31
11 Intermediate Polar Accretion Curtain . . . 32
12 Polar CV . . . 32
13 Evolution of a Cataclysmic Variable . . . 34
14 Solid Angle of a Circle . . . 36
15 Solid Angle of a Circular Disc . . . 38
16 Spectral Energy Distribution of an Accretion Disc . . . 38
17 Inhomogenous Accretion Flow . . . 40
18 Blackbody Spectrum . . . 43
19 Compton Scattering . . . 44
20 Compton Shift . . . 45
21 Inverse Compton Scattering . . . 46
22 Bremsstrahlung Radiation . . . 46
23 Bremsstrahlung Radiation Spectrum . . . 47
24 Lorentz Force . . . 48
25 Cyclotron and Synchrotron Radiation . . . 49
26 Electron Spiral in a Magnetic Field . . . 50
27 Cyclotron and Synchrotron Radiation Spectrum . . . 52
28 Synchrotron Harmonics . . . 53
29 Synchrotron Radiation Spectrum . . . 53
30 Synchrotron Radiation Spectrum . . . 54
31 *blackbody()* Function Inputs . . . 72
32 Lightcurves of the Nova-Likes . . . 84
33 Lightcurves of the Dwarf Novae . . . 85
34 Lightcurves of the Intermediate Polars . . . 86
35 Lightcurves of the Polars . . . 87
36 Broad SED of V603 Aql . . . 89
37 Broad SED of V3885 Sgr . . . 90
38 Broad SED of IX Vel . . . 91
39 Broad SED of UX UMa . . . 92

40 Broad SED of SU UMa . . . 93
41 Broad SED of U Gem . . . 94
42 Broad SED of Z Cam . . . 95
43 Broad SED of SS Cyg . . . 96
44 Broad SED of DQ Her . . . 97
45 Broad SED of DO Dra . . . 98
46 Broad SED of AE Aqr . . . 99
47 Broad SED of EX Hya . . . 100
48 Broad SED of AM Her . . . 101
49 Broad SED of AR UMa . . . 102
50 Broad SED of BL Hyi . . . 103
51 Broad SED of VV Pup . . . 104
52 Spectral Energy Distributions . . . 107
53 Broad SEDs with Accretion Rates Adjusted by Factors of 2 and 5 . . . 110
54 Maxima and Minima of ASAS-SN g-band Flux Densities for DNe . . . 111
55 Broad Spectra of Observed Systems . . . 112
56 IR to UV Flux Density Ratios . . . 114
57 IR to UV over Radio Flux Density Ratios . . . 115
58 X-Ray Flux Density Ratios . . . 116
59 Visible Flux Density / Radio Flux Density vs. Orbital Period . . . 117
60 Pala et al. (2020) SEDs . . . 119
61 Non-Magnetic Absolute Magnitude vs. Orbital Period . . . 128
62 Magnetic Absolute Magnitude vs. Orbital Period . . . 129

List of Tables

1 Properties of the Data Sources . . . 57
2 Systems and Data Sources . . . 58
3 Properties of CVs in My Sample . . . 76
4 Accretion Rates of CVs in My Sample . . . 108
5 Accretion Rates of CVs in the Pala et al. (2020) Sample . . . 126

1 Introduction

Cataclysmic variables (CVs) are low mass examples of accreting stellar remnants, a class of objects that includes white dwarfs, neutron stars, and black holes. Accretion discs are of fundamental importance in many branches of astronomy, and one of the most commonly occurring structures in the universe. Accretion discs around protostars eventually form into planets, and accretion and outflow in supermassive black holes (SMBH) regulate the growth of galaxies through active galactic nuclei (AGN) feedback mechanisms. It is believed that most stars are members of binary systems. Many binary star systems, at some stage of their evolution, undergo mass transfer, and may form accretion discs. However, accretion discs are often very difficult to study. We cannot observe the process of galaxy and solar system formation because they occur on such large timescales. We can only infer the process of their formation by observing other accretion discs, such as those in cataclysmic variable systems.

CVs are excellent laboratories to study the process of accretion, and offer one of the best opportunities to constrain our understanding of the evolution of all kinds of compact interacting binaries. CVs are numerous, there are several nearby, they are bright, it is possible to directly observe their stellar components, and we can easily measure their physical parameters. The luminosity of high mass transfer systems, such as nova-likes and dwarf novae in outburst, is dominated by the accretion disc, making study of the disc and of the underlying accretion physics much easier.

Many of the phenomena in CVs occur on timescales of minutes to years, while accretion disc activity in supermassive blackholes occurs on much longer timescales. The timescales of accreting stellar mass black holes are similar to CVs, but the shortest timescales are on the order of milliseconds, whereas in the shortest timescales in CVs are on the order of 10s of seconds or minutes. The very short timescales are also hard to study. By investigating and understanding accretion discs in cataclysmic variables, we can gain an understanding of accretion disc physics in other accreting systems, such as black hole accretion, planetary formation, and the formation of galaxies. The study of accretion discs in CVs sheds light on accretion in other systems that are not as readily observed.

Binary systems tend to reveal more about themselves, such as their masses and dimensions, than do single stars. Because the disc is very thin, the observational characteristics of CVs depend quite significantly on the inclination of the system, making estimations of the inclination, as well as other properties that are derived from it, much easier. Those systems that eclipse allow astronomers to derive direct information about the geometry of the systems, and accurately estimate the sizes and luminosities of the stars, as well as their orbital periods and separations. Binary systems are particularly useful for studying stellar mass-radius relations.

CVs are important tools in developing our understanding of evolution and the way that companions affect stellar evolution. They have also been instrumental in our understanding of the processes of magnetic braking and gravitational radiation. Magnetic cataclysmic variables are good candidates for studying the effect of magnetic fields on the process of accretion. The accumulation of hydrogen on the surfaces of white dwarf primaries results in thermonuclear runaway, observed as nova eruptions. This provides astronomers with unique opportunities to study nonequilibrium nuclear reactions.

CVs are one of the plausible progenitors of type Ia Supernovae (SNe). Due to their constant well-determined brightness at the peak of outburst, type Ia SNe are used as "standard candles" that allow astronomers to accurately pinpoint their distance. This has led to the deduction that the expansion of the Universe is accelerating, and is described by the dark energy component of the Universe. CVs are still an area of active research, in particular, much about their evolution, outburst behaviour, the period gap, flickering, and the bright spot is still not known.

Evidence of nova events and variable star observations have been recorded in historical accounts thousands of years old. Amateur astronomy has a long history, and is still a thriving hobby today. Because they are often bright enough to be seen with the naked eye and vary on timescales that can sometimes be observed in a single night, CVs are often of particular interest to amateur astronomers, who have contributed a great deal to their observation, with the result that almost continuous lightcurves over many decades are available for several dozen systems. Because there are too many CVs for professionals to monitor continuously, the record of amateur observations of CVs has been essential to our understanding of them.

While the majority of the contributions of amateur astronomers have been observations in the visual waveband, cataclysmic variables are in fact broad spectrum emitters, having been observed in all wavebands from radio to γ-ray. Much has been learned about low mass X-ray binaries (LMXBs) by studying their broad spectrum SEDs, however, to date there exists no similar study of the broad spectrum SEDs of cataclysmic variables. Such broad spectrum SEDs are the subject of this dissertation.

The first aim of this work was to gather a large set of multi-wavelength data for a sample of well-studied CVs, spanning the main CV classes and the orbital period range of CVs. The SEDs I construct from these data are used to compare systems within each class and the different classes to each other. I also use the SEDs to estimate mass transfer rates for non-magnetic CVs. Finally, I investigate a volume-limited sample, to confirm that the very bright and nearby CVs in my sample of non-magnetic systems are not representative of the intrinsic population.

I start, in Chapter 2, by giving a theoretical background of cataclysmic variables by describing their structure and basic physics, their observed phenomenology and mass transfer mechanisms, as well as summarising their evolution, defining the different CV classes and establishing the physical structures and phenomena that contribute to their spectra. I describe, in Chapter 3, the dominant emission mechanisms that are relevant to accreting binary stars, and in which physical structures the different emission mechanisms take place.

In Chapter 4 I identify my data sources and describe my methods and code. I then, in Chapter 5, define a sample of well-studied, nearby cataclysmic variables spanning the different CV classes.

In Chapter 6 I present and discuss my results, including SEDs for the systems in my sample, as well as SEDs for the Pala et al. (2020) volume-limited sample. I use these data to estimate accretion rates for the systems, and to compare the flux ratios between different wavebands. Finally, Chapter 7 contains my conclusions.

2 Cataclysmic Variables

In this section I describe the structure of cataclysmic variables, their observed phenomenology and mass transfer mechanisms, as well as the different CV classes.

Under the right conditions, clouds of interstellar dust tend to coalesce in space under the force of their own gravity (Mehlin, 1959, ch.2; Hellier, 2007, ch.4). Larger clouds, on the order of thousands of solar masses, have more self-gravitation and are more likely to collapse (Hellier, 2007, ch.4). In gasses temperature increases with pressure, and so these dust clouds slowly collapse into regions of hot, dense interstellar material, forming a cluster of young stars (Mehlin, 1959, ch.2; Serway & Renner et al., 1985, ch.19; Reese, 1999, ch.13; Hellier, 2007, ch.4). Thus stars tend to form close to one another, and are likely to have several close companions (Hellier, 2007, ch.4). They likely find themselves gravitationally bound into multiple star systems such as binaries, triples, pairs of binaries and more complex combinations (Hellier, 2007, ch.4). Single stars are rare (Postnov & Yungelson, 2006; Hellier, 2007, ch.4). Star systems involving three or more stars present an n-body problem, exhibiting chaotic orbital behaviour, and as such often involve unstable orbits, resulting in mergers and ejection of stars from the system (Rubinov, 2004). Hence, most stars can be found in binary systems or in strongly hierarchical triple systems that essentially contain a binary system orbited by a single star at a great distance (Rubinov, 2004).

A binary star system is a system of two stars that are gravitationally bound to each other, orbiting around their common centre of mass (Mehlin, 1959, ch.5). If they are widely separated then they each evolve independently, and do not interact beyond gravitationally (Postnov & Yungelson, 2006; Smith, 2007, ch.4). If they are close enough, they may exchange matter between them, and their evolution will be very different from the case of isolated single stars (Postnov & Yungelson, 2006). The interactive relationship between the two stars is dictated by their Roche lobe geometry.

2.1 Roche Potential

All points in the region of a binary star system will be subject the Roche potential, Φ, the sum of gravitational and centrifugal forces. The Roche potential is given by equations 1, 2, and 3, in which r_1 and r_2 are the position vectors of the two stars (Frank et al., 2002, ch.4). A section in the orbital plane showing the equipotential surfaces of the Roche potential is shown in figure 1.

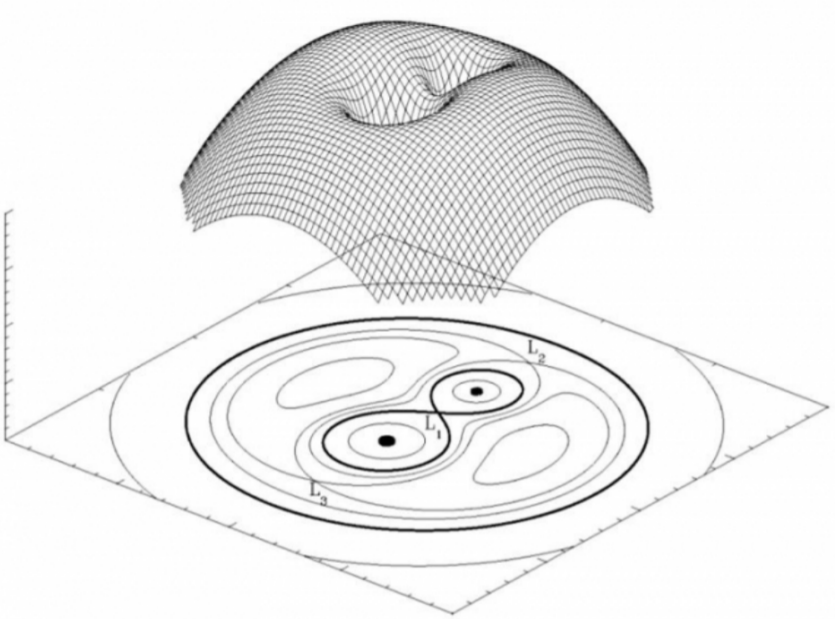

Figure 1: A projection of the Roche potential surface, and a cross section through the orbital plane, that shows the equipotential surfaces, as well as the gravity wells at the mass centres of each star, the Roche lobes (the figure-8 shaped bold line), and some Lagrangian points. The largest lobe belongs to the more massive star. Lagrangian points L_4 and L_5 are not shown. Credit: Marc van der Sluys, http://hemel.waarnemen.com/Informatie/Sterren/hoofdstuk6.html#h6.2

$$\Phi(r) = -\frac{GM_1M_\odot}{|r - r_1|} - \frac{GM_2M_\odot}{|r - r_2|} - \frac{1}{2}(\omega \wedge r)^2 \tag{1}$$

$$\omega = [\frac{(M_1 + M_2)M_\odot}{q^3}]^{\frac{1}{2}}\hat{z} \tag{2}$$

$$q = \frac{M_2}{M_1} \tag{3}$$

2.1.1 Roche Lobes

The largest closed equipotential surfaces that contain the mass of each star are known as Roche lobes (Pretorius, 2004). They are represented in figure 1 by the bold line and illustrated in figure 4. Within this region matter is gravitationally and centrifugally bound to the star (Postnov & Yungelson, 2006; Smith, 2007, ch.4).

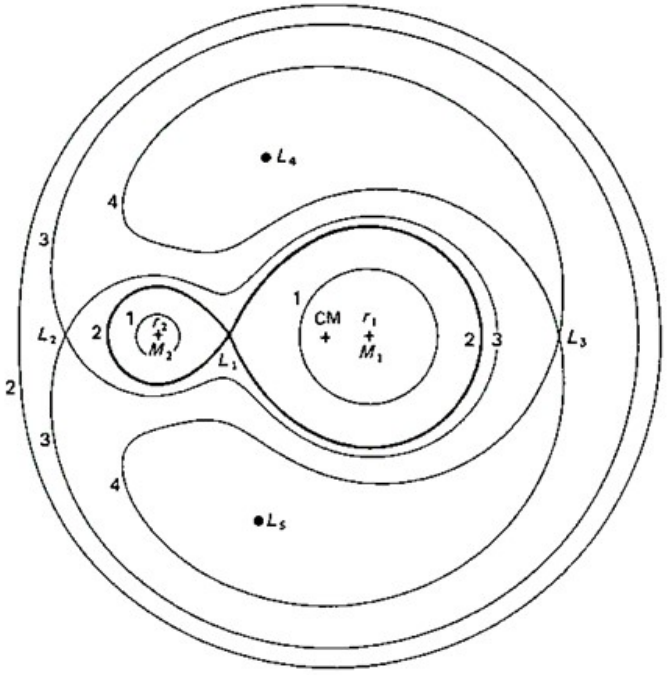

Figure 2: Cross section through the orbital plane of the Roche equipotentials. The centers of mass of the stars ($M_{1\&2}$), and the system (CM) and the Lagrangian points (L_{1-5}) are indicated, and the Roche lobes are denoted by the thick line, line 2. Credit: Frank et al. (2002, ch.4)

2.1.2 Roche Geometry

The shapes of the equipotential surfaces of the Roche potential are dependent only on the ratio of the masses of the stars, $q = M_2/M_1$ (where M_1 and M_2 are the masses of the more and less massive stars respectively), and their size is a function only of the binary separation, a (Warner, 1995, ch.2; Frank et al., 2002, ch.4; Pretorius, 2004). If the difference in the masses of the stars is great, the geometry of the Roche lobes will be significantly asymmetric, and if orbital separation is great, the lobes will be large.

2.1.3 Lagrangian Points

The Lagrangian points are the equilibrium points of the Roche potential (Frank et al., 2002, ch.4). Two orbiting masses have five such points: three metastable saddle points, L_1, L_2, L_3, that lie on the vector between the centers of mass of the orbiting masses (CoM vector), and two stable equilibrium points, L_4 and L_5, that lie symetrically either side of the CoM vector (Warner, 1995, ch.2; Frank et al., 2002,

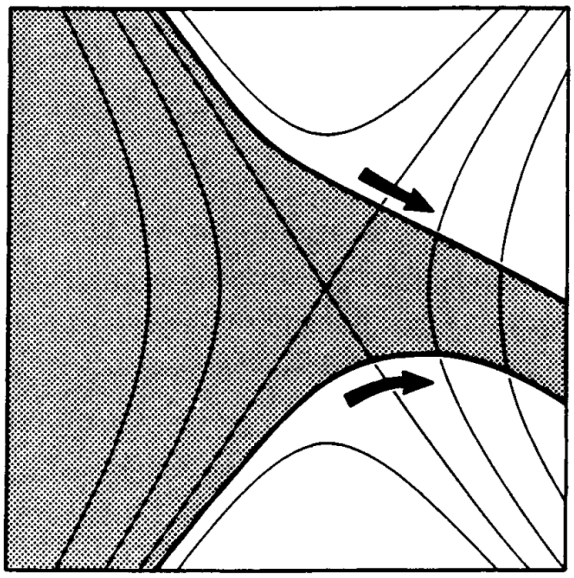

Figure 3: The bottleneck in the flow of the accretion stream as it passes through the L_1 point from the region of the secondary into the region of the primary. Credit: Pringle & Wade (1985)

ch.4). A contour plot of the potential, showing the Lagrangian points, is shown in figure 2. If a stationary point mass at one of the metastable Lagrangian points is slightly perturbed perpendicular to the CoM vector it will return to its original position, but if it is perturbed parallel to the CoM vector it will accelerate in the direction of its velocity (Smith, 2007, ch.4). L_4 and L_5 are stable equilibrium points, point masses at these points that are slightly perturbed in any direction will return the Lagrangian point of origin (Frank et al., 2002, ch.4). The Lagrangian point of particular interest to this work is the L_1 point, as it acts as a bottleneck (see figure 3) for the accretion flow of matter between the two stars, as discussed below (Warner, 1995, ch.2).

The inner Lagrangian point, where the two lobes meet, is known as the 1st Lagrangian point, or the L_1 point (Postnov & Yungelson, 2006; Hellier, 2007, ch.2; Smith, 2007, ch.4). It is a saddle point in the geometry of the equipotential, as can be seen in figure 1. A test particle at this point experiences equal force from both stars, and it is therefore an unstable equilibrium point (Smith, 2007, ch.4). A stationary test particle at this point will remain stationary unless it is perturbed (Smith, 2007, ch.4). If the test particle has velocity it will accelerate in the direction of the velocity. This point is the easiest path by which material can be transferred between the stars (Postnov & Yungelson, 2006; Hellier, 2007, ch.2).

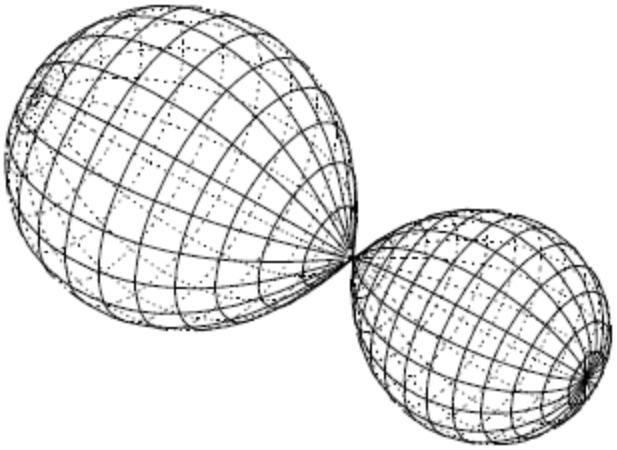

Figure 4: The Roche lobes around a binary star system. This is the gravitational equipotential within which matter is gravitationally bound to the star (Smith, 2007; Postnov & Yungelson, 2006). Where they meet is the L_1 point, an unstable gravitational and centrifugal equilibrium point (Postnov & Yungelson, 2006; Hellier, 2007, ch.2; Smith, 2007, ch.3). Credit: (Smith, 2007, ch.3).

2.2 Types of Binaries

The different types of binaries can be seen in figure 5.

2.2.1 Detached Binary

If both stars underfill their Roche Lobes they simply orbit each other, and there is no transfer of mass (except by stellar wind) (Smith, 2007, ch.3). Provided that neither star evolves to fill its Roche lobe, they evolve independently, like two individual single stars (Smith, 2007, ch.3). This is known as a detached binary (Warner, 1995, ch.2; Pretorius, 2004; Smith, 2007, ch.3).

2.2.2 Contact Binaries

If both stars fill or slightly overfill their Roche lobes they will share mass. This is known as a contact binary (Warner, 1995, ch.2; Smith, 2007, ch.3).

2.2.3 Semi-Detached Binary

If one star fills or slightly overfills its Roche lobe there will be matter at the L_1 point that will flow into the lobe of the other star (Warner, 1995, ch.2; Postnov &

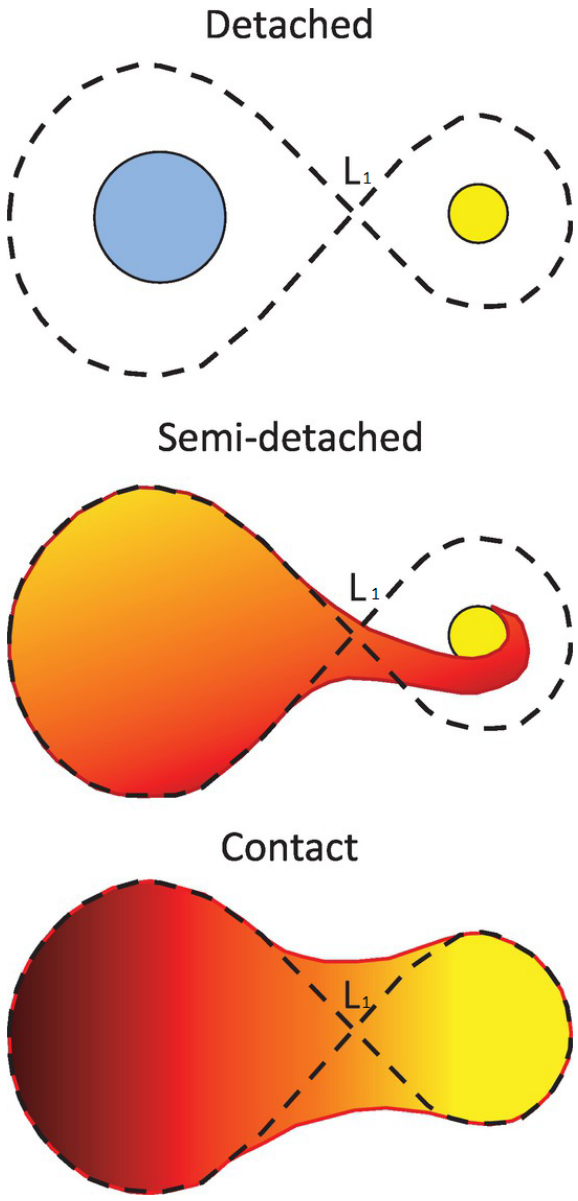

Figure 5: Binary stars may be detached, if their only interaction is gravitational and they do not share material (Smith, 2007, ch.3); semi-detached, if one star fills its Roche lobe and matter is accreted onto the other star (Postnov & Yungelson, 2006; Smith, 2007, ch.3); or contact, if both stars fill their Roche lobes and mutually share material (Smith, 2007, ch.3). The Roche lobes of the stars are denoted by the dotted line. Credit: Walker (2017)

.

Yungelson, 2006; Hellier, 2007, ch.2; Smith, 2007, ch.3). In this case the star that fills its Roche lobe is known as the secondary, and the mass-capturing star is known as the primary. Accretion by this process is known as Roche lobe overflow, and this type of system is known as a semi-detached binary (Warner, 1995, ch.2; Pretorius, 2004; Smith, 2007, ch.3).

A cataclysmic variable is a semi-detached binary star in which a white dwarf accretes matter from a late-type red dwarf donor star via Roche lobe overflow (Pretorius, 2004; Knigge, 2011). CVs are characterised by their outbursts and accretion physics that are only present in semi-detached systems (Warner, 1995, ch.2).

2.3 White Dwarfs

The primary of a cataclysmic variable is a white dwarf star.

White dwarfs are the extremely dense cores of dead stars (Hellier, 2007, ch.2). All stars with initial masses of up to about $8 - 12$ $M_\odot$ eventually become white dwarfs (Pols, 2008, ch.4). Single white dwarfs are usually between $0.5 - 0.6$ $M_\odot$, while those in CVs average about 0.8 $M_\odot$ (Hellier, 2007, ch.2; Prialnik, 2009, ch.7). They have an upper limit (Chandrasekhar limit) of 1.44 $M_\odot$ (see Section 2.3.1) (Hellier, 2007, ch.2; Prialnik, 2009, ch.7). The WDs in CVs are generally quite hot, between 10 000 K and 40 000 K (Smith, 2007, ch.5). The average white dwarf has a radius of about 7 000 km (Hellier, 2007, ch.2; Prialnik, 2009, ch.7; Hewitt, 2020).

In any massive body matter is pulled inwards due to self-gravitation (Mehlin, 1959, ch.2; Prialnik, 2009, ch.7). In normal stars this causes the material in the core to be dense and hot enough for hydrogen fusion to occur (Mehlin, 1959, ch.2; Prialnik, 2009, ch.7). Fusion releases extreme amounts of energy that push outwards and stabilise the star against gravitational collapse (Hellier, 2007, ch.2). Gravity confines the star against pressure expansion. When these forces exactly balance the star is in a state of hydrostatic equilibrium (Pols, 2008, ch.4; Prialnik, 2009, ch.7). In this condition, the star neither expands nor contracts (Pols, 2008, ch.4). Because energy is radiated away from the star in the form electromagnetic radiation, the star is only stable if nuclear reactions in the core generate enough energy to compensate for that which is radiated (Hellier, 2007, ch.2). When the hydrogen fuel in the core runs out hydrogen fusion ceases and there is no longer the outward pressure from the energy of the thermonuclear reaction (Mehlin, 1959, ch.2). The core contracts, increasing the density and squeezing the remaining hydrogen together, causing it to fuse rapidly. Large amounts of energy and pressure are released from the core, causing the outer layers, which make up about half the mass of the star, to expand outwards into space, forming a planetary nebula and leaving behind the hot, dense

core of the star (Hellier, 2007, ch.2; Smith, 2007, ch.7). It burns rapidly through the remaining fuel and becomes inactive (Hellier, 2007, ch.2). With no remaining source of thermonuclear pressure, the star contracts further. When a star no longer has outward pressure it collapses under its own gravity until a new form of outward pressure is encountered. In the case of low mass stars the core contracts to the limit of the Pauli exclusion principle, halting further contraction (Postnov & Yungelson, 2006; Hellier, 2007, ch.2; Smith, 2007, ch.7).

The volume of the white dwarf is limited by the Pauli exclusion principle, which states that no two fermions (a category of particles that includes protons, electrons and neutrons) can occupy the same quantum state at the same time (Serway & Renner et al., 1985, ch.42). This means that no two electrons with the same magnetic, angular momentum and spin quantum numbers can occupy the same atomic orbital at the same time (Serway & Renner et al., 1985, ch.42). This effectively sets a minimum volume for the white dwarf (see Section 2.3.1).

Though the core is no longer fusing, and is no longer thermally supported, there is still much thermal energy trapped inside it (Pols, 2008, ch.4). It will continue to slowly radiate this energy into space for trillions of years (Pols, 2008, ch.4). This is a white dwarf.

2.3.1 The Chandrasekhar Limit

Due to the strong gravitational forces inside a white dwarf, the radius decreases as mass increases, thus the density increases rapidly with mass (Pols, 2008, ch.4). The white dwarf mass-radius relation is given as (Nauenberg, 1972; Hellier, 2007, ch.2):

$$R_1 = 0.779(M^{-\frac{2}{3}} - M^{\frac{2}{3}})^{\frac{1}{2}} \times 10^7 \text{ m} \tag{4}$$

where M is the mass of the white dwarf as a fraction of the Chandrasekhar mass = 1.44 $M_\odot$ (Nauenberg, 1972; Hellier, 2007, ch.2; Prialnik, 2009, ch.7). This is the maximum possible mass of a white dwarf (Hellier, 2007, ch.2; Prialnik, 2009, ch.7). Above this limit the pressure of gravity will overcome Pauli exclusion and force the electrons into the nuclei, where they combine with protons to form neutrons, thus forming a neutron star (Hellier, 2007, ch.2).

2.4 Red Dwarfs

The secondary of a cataclysmic variable is a red dwarf star.

Red dwarfs are cool ($\approx$ 2900 K), low-mass, main-sequence stars (Hellier, 2007, ch.2). Unlike larger stars that have a radiative zone around the core that traps much of the hydrogen outside of the actively fusing core, red dwarfs are small enough that the entire star is convective. This means that all of the hydrogen in the star is available for fusion, and also that the helium and hydrogen constantly mix, so the concentration of hydrogen is never high (Adams et al., 2004). This, along with the fact that they are low-mass and hence less dense due to the lower gravitation, means that they have more fuel and use up their fuel very slowly (Hellier, 2007, ch.2). They burn so slowly that their average lifespan is between 1 and 12 trillion years, significantly longer than the Hubble time[7] (Adams et al., 2004; Pretorius, 2004).

2.5 Accretion

Any perturbations in the stellar matter at the L_1 point will push it into the lobe of the primary, where it will accelerate towards it (Frank et al., 2002, ch.4; Hellier, 2007, ch.2). Due to the orbital motion of the red dwarf, this stream of material will have high angular momentum, and will therefore orbit the white dwarf instead of falling directly onto it (Frank et al., 2002, ch.4; Smith, 2007, ch.3).

Hence, if the red dwarf fills its Roche lobe, a thin stream of accreting material emerges from the L_1 point and falls into orbit around the white dwarf (Hellier, 2007, ch.2; Smith, 2007, ch.3). This stream is pushed from behind by the pressure of the stellar atmosphere of the red dwarf (Hellier, 2007, ch.2). It is this pressure that continuously provides the accretion stream with new material. From the frame of reference of the white dwarf, the L_1 point is orbiting around it, hence any matter that emerges from that point will continue to orbit with the same angular momentum (Hellier, 2007, ch.2). The Coriolis force deflects the accretion stream, causing it to orbit the white dwarf on the plane of the equator of its rotational axis (Pretorius, 2004; Hellier, 2007, ch.2).

2.5.1 Accretion Disc

The accreting material falls into orbit around the white dwarf. Dissipative processes, such as collisions, shocks, and viscous dissipation, will convert some of the kinetic energy of the material into internal energy, or be radiated as electromagnetic radiation (Frank et al., 2002, ch.4). Hence the material will spread out into an accretion disc, as shown in figure 6 (Hellier, 2007, ch.2). The disc is replenished by the mass-transfer accreting stream from the secondary, which provides fresh material

[7]The Hubble time is the time required for the Universe to expand to its current size, assuming deceleration is negligible. The Hubble time is the reciprocal of the Hubble constant, $1/H_0$, about 15 billion years (Tryon, 2003).

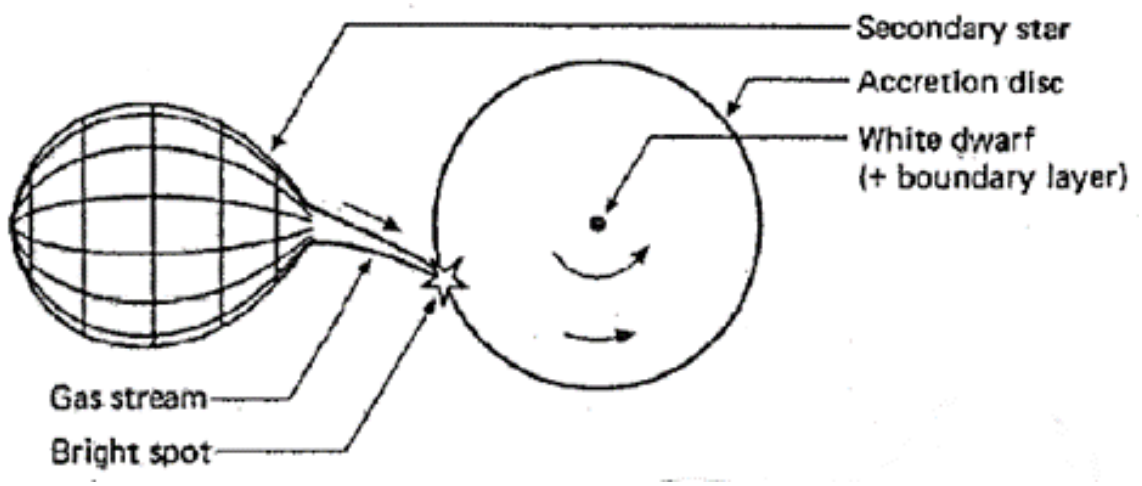

Figure 6: Material from the secondary is accreted onto the white dwarf, and falls into orbit around it, forming an accretion disc (Hellier, 2007, ch.2). Where the accretion stream meets the accretion disc there is a bright spot (Hellier, 2007, ch.2). Credit: Smith (2007, ch.1).

and angular momentum to the disc.

An accretion disc is a Keplerian disc, which is a disc of material orbiting a large mass, whose own mass is comparatively negligible. It is a disc of particles in Keplerian orbits around the central mass, with each particle following Kepler's laws of orbital mechanics (Smith, 2007, ch.5).

2.5.2 Keplerian Discs

Kepler's first and second laws state that orbiting bodies follow elliptical orbits and that their velocity is such that they always trace out a constant area in a given period of time (Serway & Renner et al., 1985, ch.14; Reese, 1999, ch.10). Given the circularisation of orbits in accretion discs (discussed in Section 2.5.6), this means that, barring interactions with other material in the disc, a particle of matter in the accretion disc will follow a circular orbit at a constant velocity.

From Kepler's third law, the Keplerian velocity is given as (Pretorius, 2004):

$$v = \sqrt{\frac{GM}{r}} \tag{5}$$

where:
G is the gravitational constant, $G = 6.674 \times 10^{-11}$ m^3 kg^{-1} s^{-2}

M is the mass of the central body, the white dwarf
r is the radius of the orbit
v is the Keplerian velocity, the velocity of an orbiting body at radius r (Hellier, 2007)

This implies that $v \propto r^{-\frac{1}{2}}$, which means that material closer to the centre will move faster than material further away (Hellier, 2007, ch.2). Each annulus of the disc rotates with its own Keplerian velocity, thus, for adjacent annuli, material further in moves faster and must slide past material further out (Hellier, 2007, ch.2). Any viscosity in the material will increase the friction between the annuli, opposing this sliding motion (Smith, 2007, ch.5). Viscosity will tend to cause the annuli to corotate, causing the outer annulus to speed up, thus increasing its angular momentum, and the inner annulus to slow down, thus decreasing its angular momentum (Hellier, 2007, ch.2; Smith, 2007, ch.5). Hence viscosity in the material causes angular momentum to flow outwards through the disc (Hellier, 2007, ch.2; Smith, 2007, ch.5). Viscosity in the disc will also cause collision and hence energy dissipation. In order to conserve angular momentum, this loss in kinetic energy will cause particles in the disc to spiral inwards (Frank et al., 2002, ch.4; Pretorius, 2004). Thus, in accretion discs, matter flows inwards and angular momentum flows outwards (Frank et al., 2002, ch.4).

2.5.3 Alpha Disc Model

Normal, molecular viscosity alone is insufficient to explain the dissipation and flow of angular momentum outwards in the disc (Frank et al., 2002, ch.4; Pretorius, 2004; Smith, 2007, ch.6). It is thought that discs are turbulent, and this turbulence is responsible for angular momentum redistribution (Smith, 2007, ch.6). Turbulence effectively increases the viscosity due to turbulent eddies in the disc (Smith, 2007, ch.6). The α-disc model introduces the adjustable α parameter that accounts for this effect (Smith, 2007, ch.6).

Turbulence can be simulated by the introduction of turbulent viscosity, which is proportional to turbulent velocity and the scale of turbulent eddies (Canuto et al., 1984; Armijo, 2012):

$$\eta \propto v_{turb} l_{turb}$$

where:
η is the turbulent viscosity
v_{turb} is the velocity of turbulent cells relative to the mean gas motion
l_{turb} is the size of the largest turbulent cells

The size of the largest turbulent eddies must be less than the scale height of the disc

(Canuto et al., 1984; Smith, 2007; Armijo, 2012):

$$l_{turb} \leq H$$

and the turbulent velocity must be less than the speed of sound in the medium, since there is no evidence of turbulent shocks (Canuto et al., 1984; Smith, 2007, ch.6; Armijo, 2012):

$$v_{turb} \leq c_s$$

thus the turbulent viscosity is given as (Canuto et al., 1984; Armijo, 2012):

$$\eta \leq c_s H$$

by introducing the coefficient α between 1 (denoting high viscosity) and 0 (denoting low viscosity) (Warner, 1995, ch.2; Canuto et al., 1984; Frank et al., 2002, ch.4; Smith, 2007, ch.6; Armijo, 2012):

$$\eta = \alpha c_s H \tag{6}$$

where:
η is the turbulent viscosity
H is the vertical height of the disc
c_s is the speed of sound in the gas
α is a coefficient less than 1 that denotes the size of the viscosity as a fraction of the limiting case

This is known as the alpha-disc model of Shakura & Sunyaev (1973). This viscosity estimate is known as alpha viscosity, and such discs are commonly called alpha discs (Smith, 2007, ch.6).

2.5.4 Boundary Layer

The material in the inner region of the disc is moving at Keplerian velocity, and the white dwarf surface is moving at its rotational velocity. In order for the accreting material to settle onto the white dwarf it must decelerate to have the same angular momentum as the surface of the white dwarf, and must first dissipate its kinetic energy (Warner, 1995, ch.2; Frank et al., 2002, ch.6; Pretorius, 2004; Balman, 2012). This creates a transition region between the accretion disc and the white dwarf, known as the boundary layer, where matter is rapidly dissipating energy (Warner, 1995, ch.2; Frank et al., 2002, ch.6; Pretorius, 2004; Balman, 2012).

2.5.5 Bright Spot

The stream of accreting material, incoming rapidly from L_1, collides with the disc material, moving in orbit (Warner, 1995, ch.2; Frank et al., 2002, ch.5; Hellier, 2007, ch.2; Smith, 2007, ch.4). This interaction is highly turbulent (Hellier, 2007, ch.2). It shocks the gas to high temperatures, and dissipates large amounts of kinetic energy, mainly in the form of electromagnetic radiation (Warner, 1995, ch.2). Hence there is a bright spot where the accretion stream meets the accretion disc, as shown in figure 6 (Frank et al., 2002, ch.5; Hellier, 2007, ch.2; Smith, 2007, ch.4).

2.5.6 Disc Circularisation

A significant amount of energy is constantly radiated away by the turbulent interaction at the bright spot, hence, the material will settle into the lowest energy orbital geometry: circular (Warner, 1995, ch.2; Pretorius, 2004; Hellier, 2007, ch.2).

The stream cannot easily change its angular momentum, and it therefore orbits at a radius that ensures that it has the same angular momentum as at L_1 (Pretorius, 2004; Hellier, 2007, ch.2). This is known as the circularisation radius (Frank et al., 2002, ch.4; Hellier, 2007, ch.2). This limits the outward spread of the accretion disc, and effectively sets an upper limit for the disc radius.

2.5.7 Tidal Effects

In close binary systems, there are significant tidal forces between the stars which causes an increase in rotation speed of the red dwarf, known as 'spinning-up', so that it synchronises with the orbital period, and the red dwarf becomes tidally locked (Smith, 2007, ch.3). Tidal forces also tend to circularize the orbits of the stars (Frank et al., 2002, ch.4; Hellier, 2007, ch.2).

At the outer edge of the disc tidal interactions with the secondary transfer disc angular momentum to it, thus limiting the outward spread of the disc and allowing matter to spiral continuously inwards (Hellier, 2007, ch.2). The smallest discs fill about half the white dwarf Roche lobe, and the largest discs fill up to 90% (Smith, 2007, ch.3).

2.6 Mass Transfer

In the case where mass is transferred from a lower-mass secondary onto a higher-mass primary, as is the case with red dwarf / white dwarf binary pairs, the lower mass star is further from the centre of mass, so the transferred material is moving closer to the centre of mass, thus losing angular momentum (Pretorius, 2004; Hellier, 2007,

ch.4). In order for momentum to be conserved the binary separation must increase, which would cause the Roche lobes to increase in size such that the secondary no longer fills its Roche lobe, thereby halting further mass transfer (Pretorius, 2004; Hellier, 2007, ch.4).

In order for mass transfer to be sustained, the secondary must remain in contact with its Roche lobe (Knigge, 2011). This may be satisfied by the secondary growing in size to fill its Roche lobe, as in the case of a red dwarf evolving into a red giant (Pretorius, 2004; Hellier, 2007, ch.4). This cannot, however, be the case for the majority of CVs, as the lifetimes of low-mas main-sequence stars exceed the Hubble time (Frank et al., 2002, ch.4; Pretorius, 2004; Hellier, 2007, ch.4).

Mass transfer may be maintained by mass loss from the system, however, rates of mass loss via stellar winds are insufficient to account for the mass transfer rates observed in CVs (Warner, 1995, ch.9; Pretorius, 2004).

Alternatively, mass transfer may be sustained by a gradual loss of angular momentum from the binary, which would maintain a small binary separation and small Roche lobes, thus allowing a smaller secondary to fill its Roche lobe and transfer material in excess of it (Frank et al., 2002, ch.4; Hellier, 2007, ch.4; Knigge, 2011).

The period distribution of CVs is bimodal, with a period gap between 2.15 and 3.18 hours that contains few systems, as shown in figure 7 (Warner, 1995, ch.2; Knigge, 2011). Mass transfer below the gap is driven primarily by gravitational radiation, and mass transfer above the gap is driven primarily by magnetic braking (Knigge, 2011).

2.6.1 Gravitational Radiation

The repetitive orbiting of massive bodies in space causes ripples in spacetime that radiate outwards, taking angular momentum from the system with them (Hellier, 2007, ch.4). The system thus loses angular momentum and the binary components spiral inwards (Hellier, 2007, ch.4). This effect is negligible for low-mass, slow moving bodies, and as such is not relevant for most binary systems (Hellier, 2007, ch.4). But as binary separation decreases, speeds increase, resulting in significant gravitational radiation (Hellier, 2007, ch.4). Thus gravitational radiation is significant in the shortest-period systems, such as cataclysmic variables (Hellier, 2007, ch.4).

2.6.2 Magnetic Braking

The short orbital periods of CVs imply high orbital velocities. Tidal forces ensure that secondaries are tidally locked to their primaries, which means that secondaries must have high rotational speeds, on the order of hours (Hellier, 2007, ch.4). Since

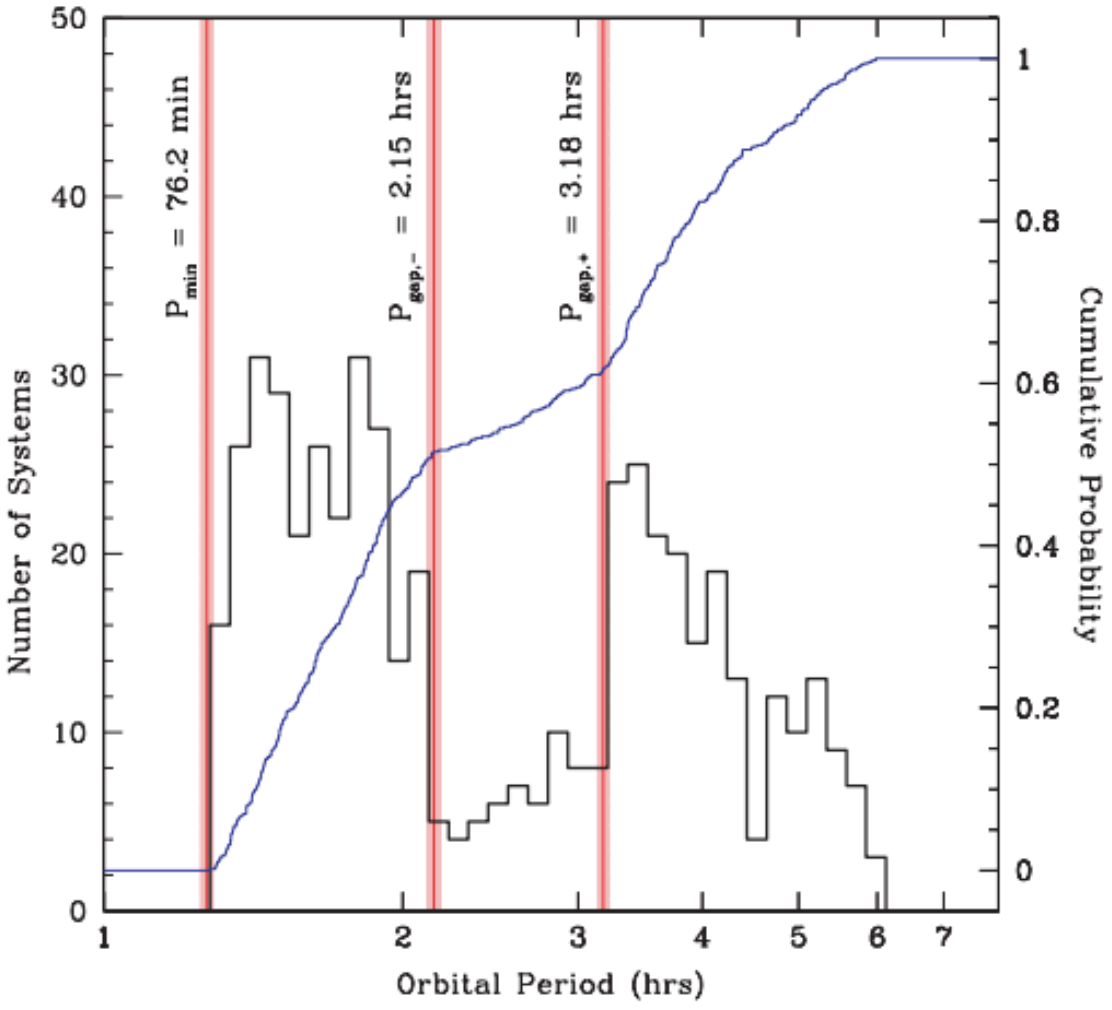

Figure 7: The differential (black) and cumulative (blue) orbital period distribution of CVs. The minimum and maximum of the period gap is denoted by red vertical lines, and the errors in these values by the red shaded regions. This plot is based on data from Ritter & Kolb (2003). Credit: Knigge (2011).

rapid stellar rotation generates strong magnetic fields, we expect red dwarfs in cataclysmic variables to be highly magnetic (Hellier, 2007, ch.4).

A stellar wind is a stream of ionised sub-atomic particles that are ejected from a star (Nussbaumer, 1982; Hellier, 2007, ch.4). Due to their strong magnetic fields and hot convective regions, we expect such winds from secondaries in CVs (Hellier, 2007, ch.4; Johnstone et al., 2015; Suzuki, 2013). Since charged particles cannot easily cross magnetic field lines, and instead spiral around them, the ionised particles will corotate with the red dwarf's magnetic field (Pretorius, 2004; Postnov & Yungelson, 2006). See Section 3.5 for an explanation of this phenomenon. These particles are accelerated to high speeds and eventually flung out into space, taking substantial angular momentum with them without significantly reducing the mass of the system (Postnov & Yungelson, 2006; Hellier, 2007, ch.4). This is known as a magnetic stellar wind (Postnov & Yungelson, 2006).

As such, the angular momentum of the secondary is reduced, as is its rotation speed (Hellier, 2007, ch.4). Since it is tidally locked in the binary orbit, the orbital velocity is reduced, and the angular momentum is ultimately lost by the whole system (Hellier, 2007, ch.4). Thus the system shrinks and the Roche lobes get smaller, allowing the red dwarf to fill its lobe (Hellier, 2007, ch.4). This process is illustrated in figure 8.

2.7 Types of CVs

The magnetic field strength of the primary, which is generally on the order of $B \approx 10^6$ G, has a significant effect on the accretion geometry (Hewitt, 2020). Low magnetic field strength ($B \lesssim 10^5$ G) results in non-magnetic CVs in which the accretion geometry is not significantly affected by the magnetic field of the white dwarf. High magnetic field strength ($B \gtrsim 10^5$ G) (magnetic CVs) results in significant distortion of the accretion geometry, partially or completely preventing the formation of an accretion disc (Smith, 2007, ch.4). Accretion geometry is one way we attempt to classify CVs, however, their classification is ultimately phenomenological. In the case of nova-likes and dwarf novae it is based on long-term photometric behaviour (Coppejans et al., 2015). Magnetic CVs are distinguished by the presence of circular polarisation, which is particularly strong in polar CVs (Smith, 2007, ch.4; Hewitt, 2020).

2.7.1 Non-Magnetic CVs

If the white dwarf is non-magnetic ($B \lesssim 10^5$ G) the accretion geometry will not be substantially disrupted by any magnetic fields (Hewitt, 2020). The accreting material will form a simple accretion disc, with matter slowly spiralling inwards as it loses

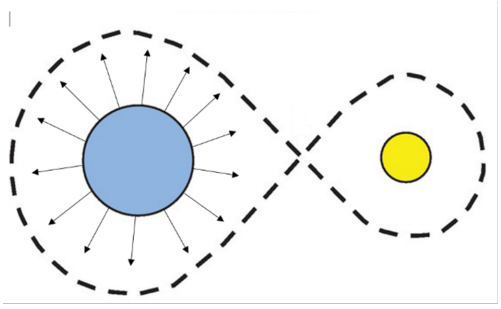

The stellar wind of the red dwarf causes it to lose angular momentum.

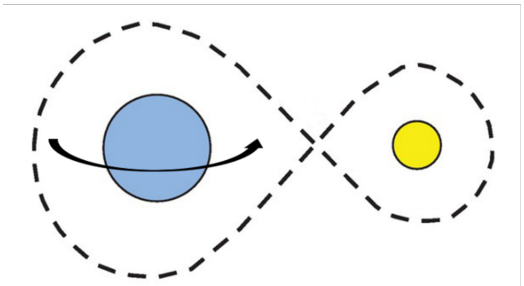

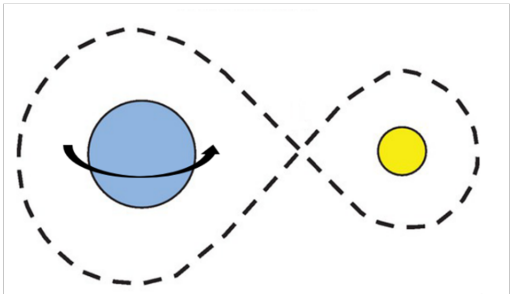

Angular momentum loss causes a reduction in the rotation speed of the red dwarf.

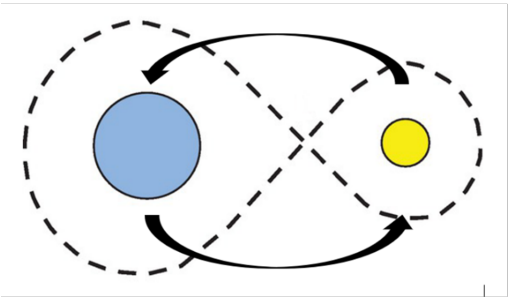

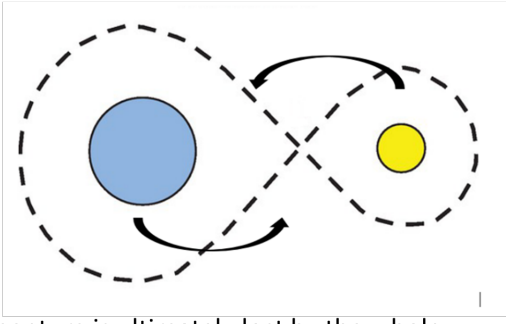

Because the stars are tidally locked, the angular momentum is ultimately lost by the whole system, causing the system to shrink.

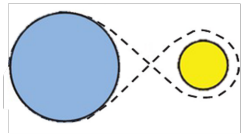

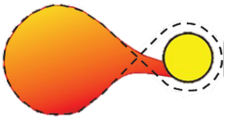

The reduced orbital separation causes the Roche lobes to shrink. The red dwarf now fills its Roche lobe, allowing accretion to continue.

Figure 8: The stellar wind of the red dwarf causes it to lose angular momentum. Angular momentum loss causes a reduction in the rotation speed of the red dwarf. Because the stars are tidally locked, the angular momentum is ultimately lost by the whole system, causing the system to shrink. The reduced orbital separation causes the Roche lobes to shrink. The red dwarf now fills its Roche lobe, allowing accretion to continue. Credit: Walker (2017).

momentum and falling preferentially on the white dwarf's equatorial zone (Hellier, 2007, ch.2; Smith, 2007, ch.4; Hewitt, 2020). A non-magnetic CV is shown in figure 6. Non-magnetic CVs are subdivided into nova-likes and dwarf novae, depending on the presence or absence of outbursts (Hellier, 2007, ch.5; Hewitt, 2020).

Nova-Likes

Nova-likes (NLs) are non-eruptive (Warner, 1995, ch.2; Hellier, 2007, ch.5; Smith, 2007, ch.4; Hewitt, 2020). They have many of the same characteristics as classical novae, and have nova-like spectra, but they have never been observed to outburst (Warner, 1995, ch.2; Hellier, 2007, ch.5; Smith, 2007, ch.4; Hewitt, 2020). Nova-like variables have a perpetually high accretion rate that continually drains the disc and stabilises it against dwarf-nova outbursts (Hellier, 2007, ch.5).

Dwarf Novae

In dwarf novae (DNe) material is transferred from the secondary faster than it can be transported through the disc, thus accreting material builds up in the accretion disc (Osaki, 1974; Warner, 1995, ch.2 Hellier, 2007, ch.5; Smith, 2007, ch.4). This increases the viscosity, which in turn increases the rate of angular momentum flow through the disc, causing it to spread inwards and outwards (Osaki, 1974; Hellier, 2007, ch.5; Smith, 2007, ch.4). Thus the rate of accretion onto the white dwarf increases, causing an increase in the luminosity of the system that is seen as a dwarf nova outburst (Osaki, 1974; Hellier, 2007, ch.5; Smith, 2007, ch.4). This process drains the disc, returning the system to quiescence (Osaki, 1974; Hellier, 2007, ch.5; Smith, 2007, ch.4). These outbursts reach their peak within about a day, occur semi-regularly on timescales from days to decades with amplitudes between 2-8 magnitudes, and last for days or weeks (Hewitt, 2020).

SU UMa systems, a subclass of dwarf novae, are found below the period gap, and produce superoutbursts that are thought to result from tidal thermal instability (Thorstensen et al., 1986; Smith, 2007, ch.4). These are longer, higher-amplitude eruptions that occur in addition to typical dwarf nova eruptions, and are accompanied by superhumps, which are similar to ordinary dwarf novae outbursts but drift in orbital phase (Warner, 1995, ch.2). They are thought to be the result of an elliptical disc (Thorstensen et al., 1986; Smith, 2007, ch.4).

Dwarf novae of the subclass Z Cam exhibit typical dwarf novae outbursts, but the decline of the outburst sometimes plateaus at about 1 mag below maximum (Warner, 1995, ch.2; Oppenheimer et al., 1998; Hartley et al., 2005; Smith, 2007, ch.4). These brightness plateaux may last from a few days to a few years (Warner, 1995, ch.2;

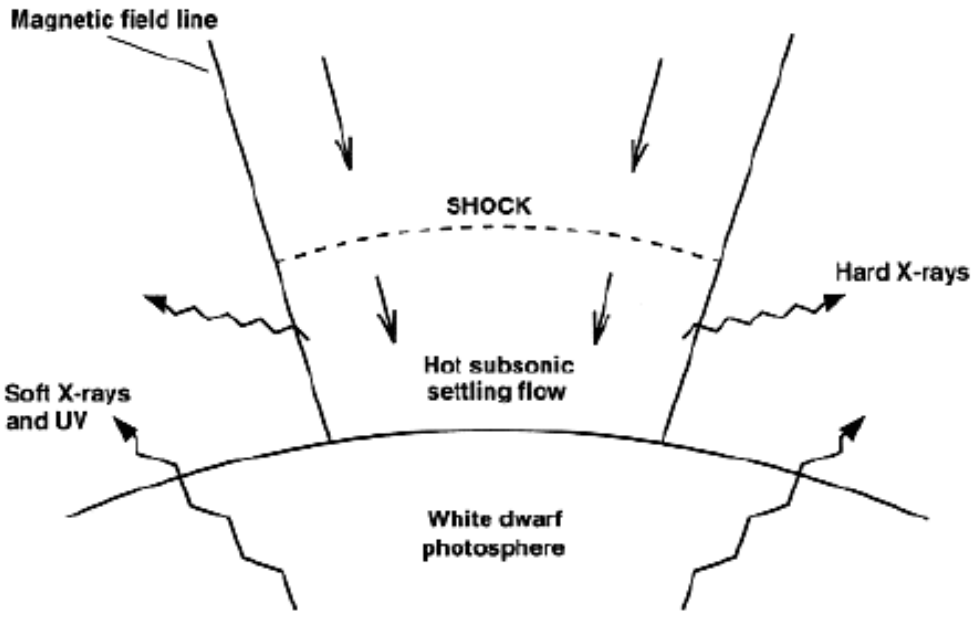

Figure 9: The accretion column of an accreting white dwarf. The accreting material falls around the pole of the white dwarf, and emits X-rays. Credit: Potter (1999)

Oppenheimer et al., 1998; Hartley et al., 2005; Smith, 2007, ch.4).

2.7.2 Magnetic CVs

Magnetic CVs (mCVs) have magnetic white dwarfs whose magnetic fields are sufficiently strong ($B \gtrsim 10^5$ G) that they play a role in controlling the accretion flow (Frank et al., 2002, ch.6; Smith, 2007, ch.4). Because the accreting matter is ionised, it will interact with the magnetic field, and hence magnetic CVs do not form simple accretion discs (Frank et al., 2002, ch.6; Smith, 2007, ch.4). The magnetic white dwarf will be surrounded by a magnetosphere. When the ionized accretion stream encounters the magnetosphere the flow of material is directed along the magnetic field lines and forms an accretion column that falls around the magnetic poles of the star (Frank et al., 2002, ch.6; Smith, 2007, ch.4). An accretion column is shown in figure 9. The magnetic field strengths of astronomical objects can be estimated by observing the relative presence of circular polarisation emitted by cyclotron and synchrotron radiation, as discussed in Sections 3.5 and 3.6.

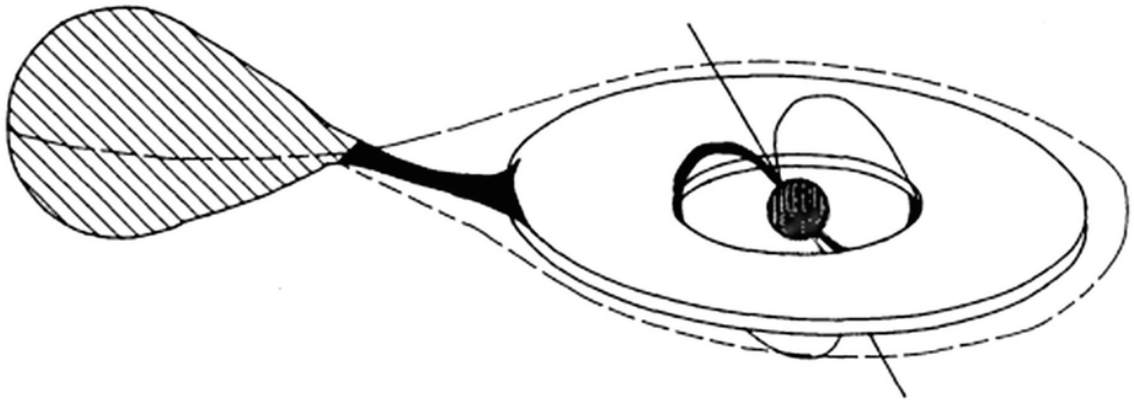

Figure 10: An intermediate polar CV. The accreting matter forms an accretion disc whose inner edge meets the magnetosphere of the white dwarf (Smith, 2007, ch.4). It then follows the magnetic field lines of the white dwarf and falls around its poles (Smith, 2007, ch.4). Credit: Shahbaz (2019)

Intermediate Polars

If the white dwarf has a weak magnetic field ($10^5\,\mathrm{G} \lesssim B \lesssim 10^7\,\mathrm{G}$) and a small magnetosphere an accretion disc may form around the magnetosphere ((Warner, 1995, ch.2); Hellier, 2007, ch.9; Smith, 2007, ch.4). The inside of the ring meets the magnetosphere and flows onto the poles of the white dwarf along the magnetic field lines (Hellier, 2007, ch.9; Smith, 2007, ch.4). Because the accretion disc meets the magnetosphere at all points on its inner edge, the accreting material forms an accretion curtain as it flows onto the poles (Smith, 2007, ch.4). An intermediate polar (IP) is shown in figure 10. Because the accretion disc forms around the rotational equator of the white dwarf, and the ionised material falls around the magnetic poles, if the rotational and magnetic poles do not align, one side of the accretion disc falls around the North pole, while the other side falls around the South Pole (Hellier, 2007, ch.9). This is shown in figure 11.

Polars

If the white dwarf is strongly magnetic ($\mathrm{B} \gtrsim 10^6\,\mathrm{G}$) such that the radius of the magnetosphere is on the order of the orbital separation, an accretion disc cannot form, and the accreting material flows directly from the L_1 point along the field lines to the magnetic poles, as shown in figure 12 (Warner, 1995, ch.2; Frank et al., 2002, ch.6; Smith, 2007, ch.4). The magnetic field of the white dwarf is so strong that an accretion disc cannot form (Smith, 2007, ch.4).

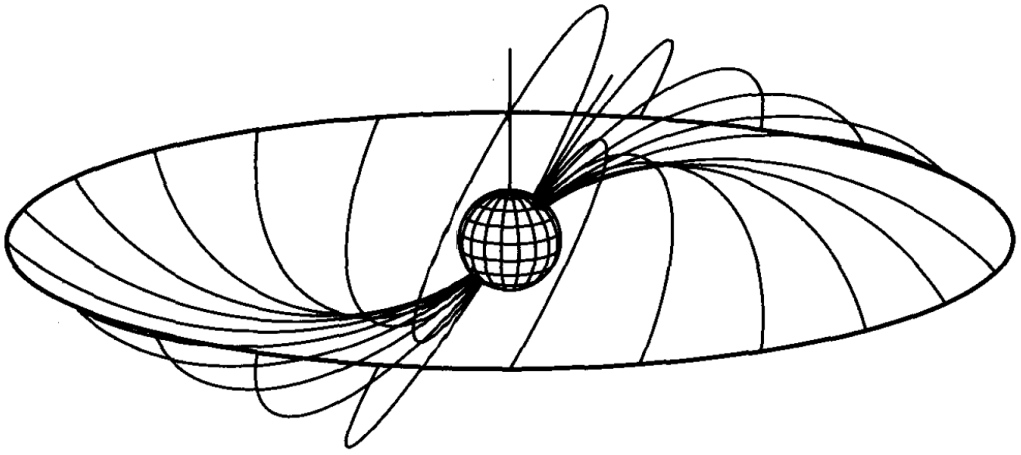

Figure 11: The accretion curtain of an intermediate polar CV. The inner edge of the accretion disc, where it meets the magnetosphere, is depicted by the outer ring, and the rotational axis by the vertical line. The rotational and magnetic poles may not align, in which case one side of the accretion disc falls around the North magnetic pole, while the other side falls around the South magnetic pole. Credit: (Hellier, 2007, ch.9).

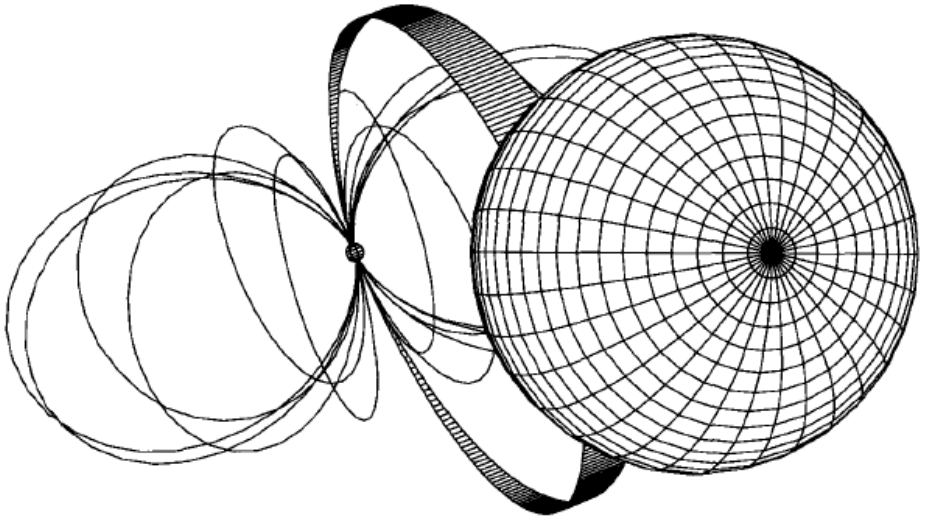

Figure 12: A polar CV. The white dwarf is magnetic and, because the accreting material is ionised, it follows the magnetic field lines of the white dwarf and falls around its poles, without forming an accretion disc (Smith, 2007, ch.4). Credit: Hellier (2007, ch.9)

2.8 Origin of CVs

A cataclysmic variable system begins as two main sequence stars of different masses that orbit fairly close, at a few hundred solar radii (Hellier, 2007, ch.4). The more massive star evolves more rapidly and swells to becomes a red giant (Hellier, 2007, ch.4; Smith, 2007, ch.7). Because the binary separation is small the Roche lobes are small and it overfills its Roche lobe, transferring material onto its lower-mass companion (Hellier, 2007, ch.4; Smith, 2007, ch.7). The system is now a semi-detached binary transferring material from high-mass to low-mass.

This situation is unstable (Hellier, 2007, ch.4). Because the heavier star is closer to the centre of mass of the system, mass is being transferred away from the centre of mass (Hellier, 2007, ch.4; Smith, 2007, ch.7). To conserve angular momentum, the stars move closer to the centre of mass, decreasing the binary separation (Hellier, 2007, ch.4; Smith, 2007, ch.7). This causes the Roche lobes to decrease in volume, and the red giant overfills its Roche lobe more, despite the fact that it is losing material (Hellier, 2007, ch.4; Smith, 2007, ch.7). This sets up is a positive feedback loop that results in the entire envelope of the red giant being accreted rapidly onto its companion (Hellier, 2007, ch.4; Smith, 2007, ch.7).

The companion, a low mass red dwarf with a small Roche lobe, cannot assimilate all of the material transferred onto it (Hellier, 2007, ch.4; Smith, 2007, ch.7). The result is that both stars overfill their Roche lobes, forming a contact binary, consisting of a red dwarf and the white dwarf core of the red giant (Smith, 2007, ch.7). This is effectively a cataclysmic variable orbiting inside a red giant (Hellier, 2007, ch.4). The binary is surrounded by a cloud of stellar matter known as a common envelope (Postnov & Yungelson, 2006; Hellier, 2007, ch.4; Smith, 2007, ch.7).

The orbiting stars drag on this material, and they transfer their kinetic energy to it and spiral inwards from about 100 solar radii to about 1 solar radii in about 1000 years (Postnov & Yungelson, 2006; Hellier, 2007, ch.4; Smith, 2007, ch.7). The energy and angular momentum transferred to the envelope cause it to expand outwards into interstellar space, forming a planetary nebula (Hellier, 2007, ch.4; Smith, 2007, ch.7). What remains is a white dwarf / red dwarf binary that is either detached, if the separation is still too large for transfer, or semi-detached, in which case it is a novel cataclysmic variable (Hellier, 2007, ch.4).

A schematic depicting the evolution of a cataclysmic variable is shown in figure 13.

2.9 The Spectral Energy Distributions of CVs

A Spectral Energy Distribution (SED) is a plot of light energy versus wavelength or frequency. The SED of a CV is the sum of contributions from several components

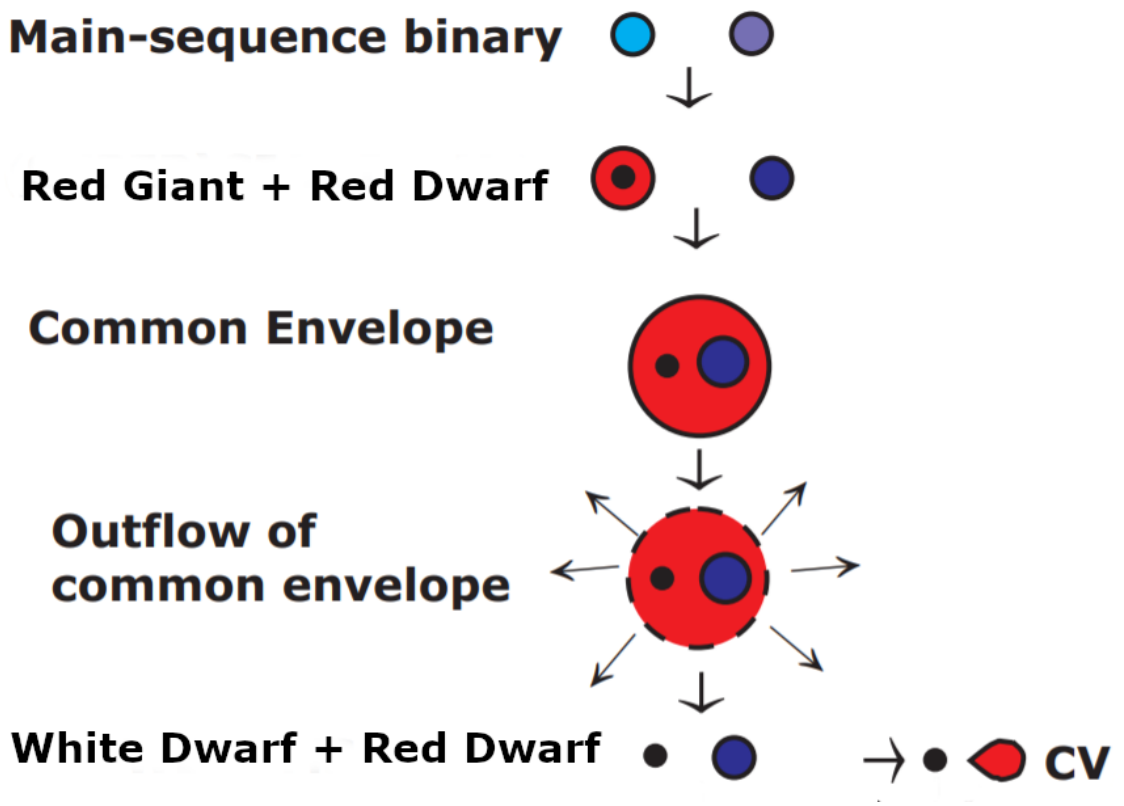

Figure 13: A cataclysmic variable begins as a pair of main-sequence stars (Hellier, 2007, ch.4). One evolves into a red giant star that eventually surrounds the entire system in a common envelope (Postnov & Yungelson, 2006; Hellier, 2007, ch.4; Smith, 2007, ch.7). The envelope is expelled into space, leaving behind a white dwarf / red dwarf binary that, if close enough, will accrete, becoming a cataclysmic variable (Hellier, 2007, ch.4; Smith, 2007, ch.7). Credit: Postnov & Yungelson (2006).

of the binary, as discussed below.

2.9.1 White Dwarf

A white dwarf very closely approximates a blackbody (see equation 8) (Hellier, 2007, ch.3). They depart from a blackbody due to a thin layer of hydrogen, and sometimes helium, on their surface (Hellier, 2007, ch.3).

2.9.2 Red Dwarf

Because the red dwarf is cool, its spectrum is red, with most of its light emitted at infrared and red optical wavelengths (Hellier, 2007, ch.3). Since blackbody emission increases in proportion to surface area, the emission of the red dwarf is not swamped by that of the white dwarf, and its emission can be seen in the red and infrared regions of the CV spectrum (Hellier, 2007, ch.3).

2.9.3 Stellar Spectra

The solid angle of a circle is given by (Tryka, 1997):

$$\Omega_{circle} = 2\pi(1 - \frac{d}{\sqrt{R^2 + d^2}}) \tag{7}$$

where:
d is the distance between the observer and the circle
R is the radius of the circle

This is illustrated in figure 14. Thus, observed stellar flux density of the red and white dwarfs are given as:

$$F_\nu = 2\pi(1 - \frac{d}{\sqrt{R^2 + d^2}})B_\nu(T) \tag{8}$$

where B_ν is the blackbody flux density at a given frequency and T is the temperature of the blackbody.

2.9.4 Accretion Disc

Modelling the SED of an accretion disc is extremely challenging, especially in the case of low-accretion rate, optically thin discs and systems that undergo DN outburst cycles. However, optically thick, steady-state discs, such as one expects to find in

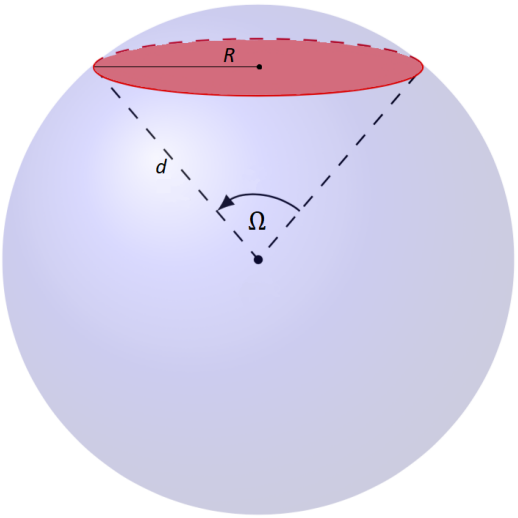

Figure 14: The solid angle, Ω, subtended by a circle of radius R at a distance d. Credit: https://tex.stackexchange.com/questions/483789/add-an-angle-to-a-sphere

NLs and DNe in outburst, can be modelled with some success as a multi-temperature blackbody.

The accretion disc has a radius dependent temperature gradient. They are cool at their outer edge, approximately 5 000 K, but heat up to about 30 000 K in their inner regions due the release of gravitational energy (Hellier, 2007, ch.3). Each annulus of the disc radiates roughly as a blackbody (Frank et al., 2002, ch.5).

The temperature at a given radius of the disc is dependent on the viscous dissipation rate of an optically thick Keplerian disc of that radius (Frank et al., 2002, ch.5; Hewitt, 2020). This relation is given by equation 9.

$$D = \sigma T^4 \tag{9}$$

where:
D is the viscous dissipation rate
T is temperature
σ is the Stefan-Boltzmann constant $= 5.670374 \times 10^{-8}\ W\ m^{-2}\ K^{-4}$

The viscous dissipation rate is related to the radius by equation 10 (Frank et al., 2002, ch.5; Hewitt, 2020).

$$D(R) = \frac{3GM_1\dot{M}}{8\pi R^3}\left(1 - \left(\frac{R_{in}}{R}\right)^{\frac{1}{2}}\right) \tag{10}$$

where:
D is the viscous dissipation rate
G is the gravitational constant $= 6.67430 \times 10^{-11}$ m^3 kg^{-1} s^{-2}
M_1 is the mass of the white dwarf
$\dot{M}$ is the accretion rate
R is the radius at which dissipation rate is being calculated
R_{in} is the inner radius of the disc

For an observer at distance d whose line of sight makes an angle i to the normal of the plane of the disc, the solid angle of an inclined disc is given by:

$$\Omega_{disc} = \frac{2\pi\cos(i)}{d^2}\ R\ \delta R \tag{11}$$

where:
d is the distance between the observer and the disc
i is the angle between the line of sight to the disc, and the normal of the plane of the disc
δR is the disc radius

This is illustrated in figure 15.

Hence the flux density of the accretion disc is given as:

$$F_\nu = \frac{2\pi\cos i}{d^2}\ \int_{R_{in}}^{R_{out}} R\ B_\nu(T)\ \delta R \tag{12}$$

where B_ν is the blackbody frequency flux.

This is the sum of an infinite series of blackbody spectra, and so the integrated spectrum F_ν is a stretched-out blackbody spectrum. F_ν is similar in shape to a blackbody, but is flatter at its peak. Such a spectrum is shown in figure 16.

Hence, due to the radius-dependent temperature gradient accretion discs only approximate blackbodies. The overall spectrum of CV accretion discs is flatter in the optical than a true blackbody.

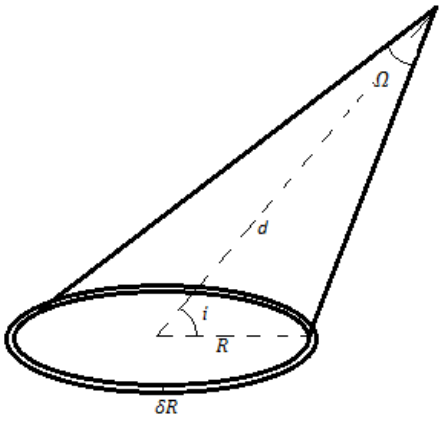

Figure 15: The solid angle, Ω, of a circular disc of inner radius R and width δR at a distance d and inclination i. Credit: https://socratic.org/questions/what-is-formula-for-solid-angle-labeled-in-the-given-figure-as-omega

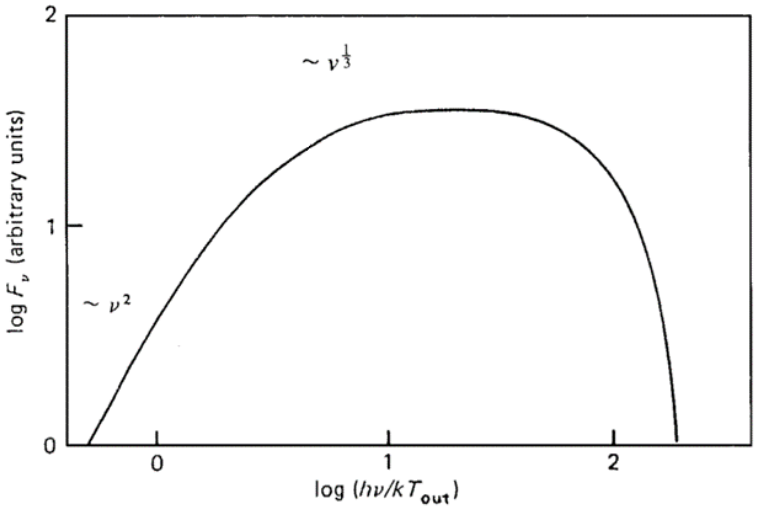

Figure 16: The frequency flux density spectrum of a geometrically thin, optically thick accretion disc radiating locally as a blackbody. Credit: Frank et al. (2002, ch.5)

2.9.5 Inclination

The inclination of a binary system is the angle between the normal of the plane of oscillation of the disc and the line of sight. High-inclination systems ($i \gtrsim 57°$) may result in eclipses and self-occultation of the disc, which will effect the lightcurves and SED of the systems. A high inclination angle also exposes the rim of the disc, which may not be a blackbody (Knigge et al., 2000). Semi-detached systems with an inclination greater than $33.69° < i < 34.45°$ are likely eclipsing systems (Morris, 1999).

2.9.6 Boundary Layer

Only about half the gravitational potential energy dissipated by the accreting material is emitted as disc luminosity, while the other half is emitted by the boundary layer (Frank et al., 2002, ch.6; Pretorius, 2004). When the system is accreting rapidly the boundary layer is optically thick. It dissipates thermal energy efficiently, and is therefore relatively cool and is optically bright in the soft X-ray. When accretion is slow and the boundary layer is optically thin and does not dissipate energy efficiently, it is hotter, and bright in the hard X-ray (Pretorius, 2004; Balman, 2012). We therefore expect significant X-ray luminosity in the spectral energy distributions of cataclysmic variables (Balman, 2012).

2.9.7 Bright Spot

The contribution of the bright spot will depend on its brightness and temperature, as well as the orientation of the system, and will vary as the system orbits. In some CVs the bright spot emits up to 30% of the light from the system, and may dominate at their brightest wavelengths, generally in the optical (Warner, 1995, ch.2; Froning, 1999; Frank et al., 2002, ch.6; Unda-Sanzana, 2005; Hellier, 2007, ch.2). There is as yet no theoretical treatment of the bright spot.

2.9.8 Jets

Cataclysmic variables belong to a broad class of objects that exhibit accretion behaviour and produce accretion discs (Coppejans & Knigge, 2020). CVs have, until recently, been thought to be one of the few examples of such objects that do not launch jets (Coppejans & Knigge, 2020). However, recent observations of CVs have shown radio flaring consistent with jets (Coppejans & Knigge, 2020). While these observations have not confirmed the existence of radio jets on CVs, significant radio emission in the spectra of CVs may be the result of jets (Coppejans & Knigge, 2020). Some polar CV were detected in the radio several decades ago, whereas non-magnetic CVs were only more recently found to be radio emitters, with the help of much more

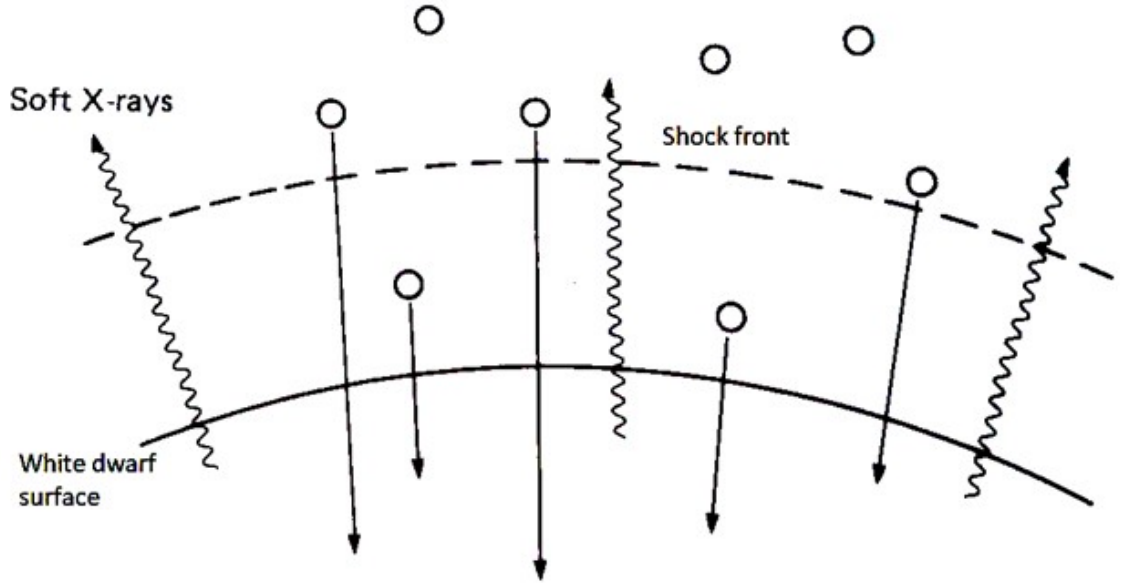

Figure 17: Soft X-rays are emitted by the accretion column due to blobs of dense accretion material penetrating the shock front and impacting the white dwarf
Credit: Frank et al. (2002, ch.6)

sensitive radio observations (Coppejans & Knigge, 2020). DNe are detected in the radio only in outburst (Coppejans et al., 2016a; Coppejans & Knigge, 2020).

2.9.9 Accretion Column

As the material in the accretion column (see Section 2.7.2) approaches the white dwarf its trajectory is almost radial as it follows the magnetic field lines of the white dwarf, and its velocity is highly supersonic, resulting in the formation of a supersonic shock front above the surface of the white dwarf pole (see figure 9) (Frank et al., 2002, ch.6; Pretorius, 2004). This results in hard X-ray emission. This phenomenon is accompanied by denser blobs of accreting material that have sufficient momentum to penetrate the shock front and impact the white dwarf, where their kinetic energy is absorbed by the white dwarf, resulting in soft X-ray and EUV emission (see figure 17) (Patterson, 1994; Frank et al., 2002, ch.6; Pretorius, 2004). The accretion column that forms in magnetic CVs is therefore luminous in the X-ray and EUV (Frank et al., 2002, ch.6).

2.9.10 Combined Spectrum

The broad spectral energy distributions of cataclysmic variables will include contributions from all components of the system. The white dwarf contribution will be primarily in the ultraviolet range, the red dwarf contribution primarily in the infrared range, and, despite its low temperature, significant in comparison to the white dwarf due to its size. The accretion disc contribution will be primarily in the optical, and broad in comparison to a blackbody. The contributions of the boundary layer and jets will be in the extreme UV / X-ray and radio respectively. The contribution of the bright spot will depend on brightness and temperature and the orientation of the system.

The combined spectrum of these components in the infrared to ultraviolet range is likely that of a blackbody flattened in the optical due to the contribution of the disc. However, if the stellar components are particularly bright, they may be sufficient to distort the combined spectrum, causing it to have two local maxima in the regions of the spectrum dominated by the stars, and the spectrum will thus be bimodal. In systems with bright stellar components this phenomenon will be quite pronounced, whereas systems with dim stellar components will have combined spectra that more closely resemble a flattened blackbody.

3 Emission Mechanisms

In this section I describe the dominant emission mechanisms that are relevant to accreting binary stars, and in which physical structures of the binary the different emission mechanisms take place.

3.1 Thermal Radiation

Thermal radiation is emitted by a material when the emitting particles are in local thermodynamic equilibrium; they have a Maxwellian velocity distribution (Longair, 2011, ch.1).

Heat energy causes charged particle motion within a material. These accelerating electric charges then emit electromagnetic radiation, thus thermal energy is converted into electromagnetic energy (Robertson, 1941, ch.18; Jenkins & White, 1957, ch.21). Because higher heat energy implies more charged particle motion, which will result in higher-energy electromagnetic radiation, the frequency of the emitted light is temperature dependent (Hecht, 1987, ch.3).

A blackbody is a perfect emitter and absorber, it does not reflect or transmit electromagnetic radiation, thus the light emanating from it is only that of its own thermal radiation (Hecht, 1987, ch.3). Hence the thermal radiation spectrum is that of a blackbody. Blackbodies emit a characteristic continuous spectrum that depends only on temperature (Robertson, 1941, ch.18; Hecht, 1987, ch.3). The spectral radiance of a blackbody emitter is given by Planck's radiation law (Serway & Renner et al., 1985, ch.40; Hecht, 1987, ch.3):

$$B_\nu(\lambda, T) = \frac{2\pi hc^2}{\lambda^5(e^{hc/\lambda kT} - 1)} \tag{13}$$

Where:
h is Planck's constant $= 6.626 \times 10^{-34}$ J.s (Serway & Renner et al., 1985, ch.40)
k is the Boltzmann constant $= 1.38 \times 10^{-23}$ J.K^{-1} (Serway & Renner et al., 1985, ch.19)

For a given temperature of the source, there is a certain frequency at which the intensity of the emitted radiation peaks (Robertson, 1941, ch.18). With increasing temperature the peak shifts to higher frequencies and increases in intensity, hence the total energy emitted at all wavelengths increases rapidly with absolute temperature (Hecht, 1987, ch.3). The wavelength at which the radiation peaks is given by Wein's displacement law (Jenkins & White, 1957, ch.21; Serway & Renner et al., 1985, ch.40; Hecht, 1987, ch.3):

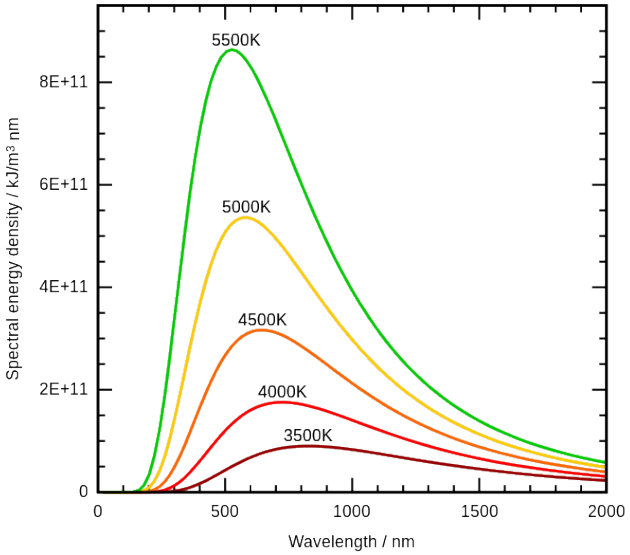

Figure 18: The blackbody or thermal radiation spectrum for several temperatures. The peak of radiation shifts to shorter wavelengths for higher temperatures, and the total energy emitted increases.
Credit: https://en.wikipedia.org/wiki/Thermal_radiation

$$\lambda_{max} T = 0.28978 \times 10^{-2} \text{ m.K} \tag{14}$$

At room temperature radiation peaks in the infrared. CV accretion discs tend to peak in the visible region of the electromagnetic spectrum (Scaringi, 2015). A diagram of several blackbody curves for different temperatures is shown in figure 18.

The thermal radiation emitted by CVs is produced primarily by the hot inner portion of the accretion disc (Williams, 1980).

3.2 Compton Scattering

A high-energy incident photon collides with an electron. Some of the photon energy is absorbed by the electron and the rest is reradiated as a lower-energy photon, as shown in figure 19 (Robertson, 1941, ch.20; Serway & Renner et al., 1985, ch.40; Reese, 1999, ch.26). This change in wavelength is known as Compton shift (Serway & Renner et al., 1985, ch.40). It depends on the angle at which the scattered radiation is observed relative to the direction of the incident radiation, θ, as in equation 15 (Serway & Renner et al., 1985, ch.40; Reese, 1999, ch.26). The incident radiation has wavelength λ. At an angle θ the scattered photons have intensity peaks at two

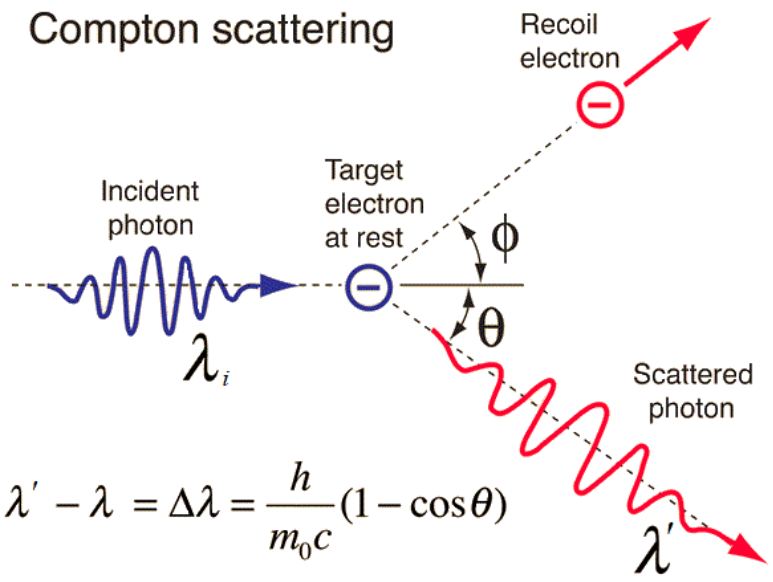

Figure 19: Compton scattering of a photon by an electron. The photon imparts some of its energy onto the electron, and scatters away as a lower energy photon. Credit: http://hyperphysics.phy-astr.gsu.edu/hbase/quantum/compton.html#c1

distinct wavelengths, λ and λ'. If the scattered photons are observed at $\theta = 0°$, there is no Compton shift in wavelength (Serway & Renner et al., 1985, ch.40; Reese, 1999, ch.26). The maximum Compton shift is (Serway & Renner et al., 1985, ch.40; Reese, 1999, ch.26). Compton shift, and its dependence on wavelength, is shown in figure 20.

$$\Delta\lambda = \lambda' - \lambda = \frac{h}{m_0 c}(1 - \cos\theta) \tag{15}$$

Because CVs emit mainly in the infrared to ultraviolet, Compton scattering is not significant. It is however observed in the stellar corona of X-ray binaries (Code, 1949; White & Holt, 1981; Shi, 2021).

3.3 Inverse Compton Scattering

A photon collides with a high-energy electron. Some of the energy of the electron is imparted onto the photon, so that the scattered photon is higher frequency than the incident photon (Pfleiderer & Grewing, 1966). This interaction is shown in figure 21.

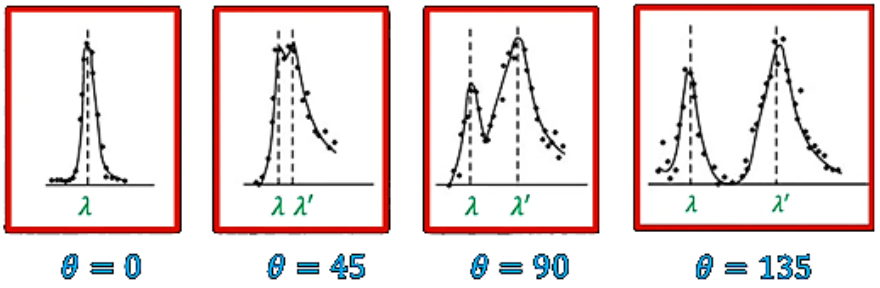

Figure 20: Compton Shift. For monochromatic incident light, of wavelength λ, the spectrum of Compton scattering has two distinct peaks, at λ and λ'. The Compton shift in wavelength, $\Delta\lambda = \lambda' - \lambda$, varies with the angle θ at which the scattered photons are observed. Credit: https://www.youtube.com/watch?v=rGy7nsC8O_Y&t=813sab_channel=PhysicsExplained

While inverse Compton scattering has a significant effect on the spectra of black holes and AGN accretion discs, it has not been observed in CVs (Zhang & Cheng, 1997; Vuillaume et al., 2012; Kinch et al., 2020).

3.4 Bremsstrahlung Radiation

Bremsstrahlung "braking" radiation is emitted by a charged particle when it is deflected by the presence of another charged particle (Longair, 2011, ch.6). Typically, this is an electron that is deflected by the presence of an atomic nucleus (Serway & Renner et al., 1985, ch.45).

A negative electron with a certain velocity v_i and kinetic energy E_i, is deflected by the electric field of a positive atomic nucleus, and exits the interaction with velocity v_s and kinetic energy E_s. Due to its large mass, the recoil of the nucleus is negligible (Eberhard & Werner, 2004). Radiation is emitted that accounts for the change in the electron's kinetic energy, $E_\gamma = E_i - \mathrm{E_s}$ (Eberhard & Werner, 2004). Diagrams of this interaction for different impact parameters are shown in figure 22.

The electron is deflected from its original trajectory in the direction of the nucleus by an angle θ, which depends on its velocity and the distance of the encounter, given by the impact parameter, b (Eberhard & Werner, 2004). The angle of deflection θ is greater when the electron is moving more slowly, and when the impact parameter is small (Eberhard & Werner, 2004). The Coulombic force of attraction between the electron and the atomic nucleus is greater if the charge on the nucleus is stronger, so the angle of defection will be greater for heavier elements (Eberhard & Werner, 2004).

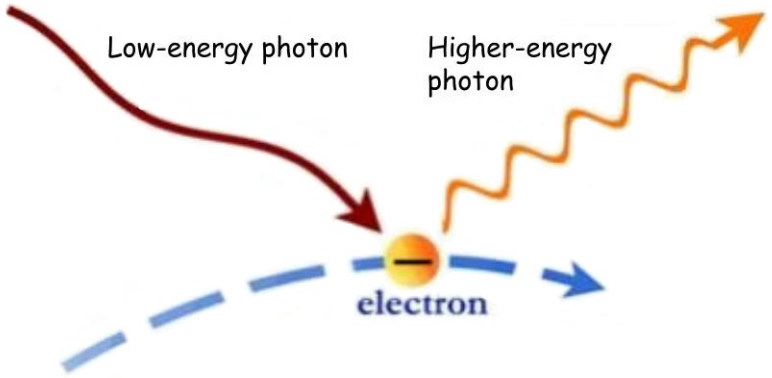

Figure 21: Inverse Compton scattering. A photon collides with a high-energy electron, causing the electron to lose energy and the photon to be scattered away as a higher-energy photon. Credit: http://www.outerspacecentral.com/x_ray_page.html

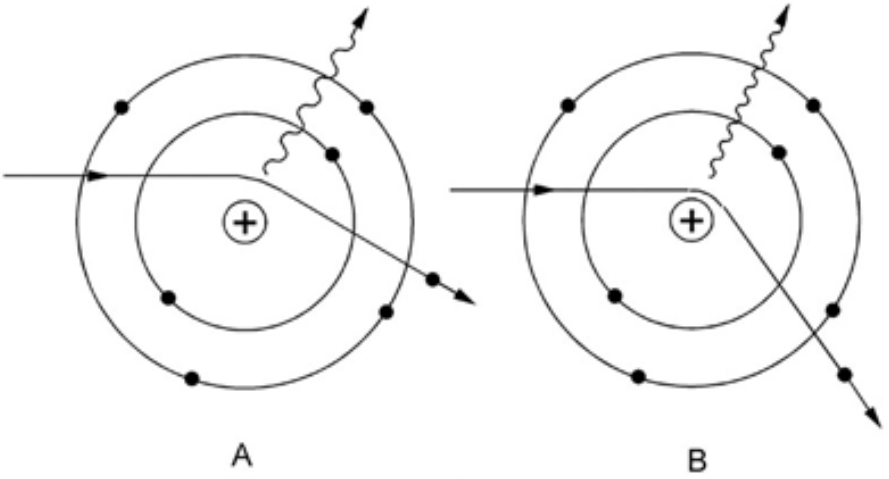

Figure 22: Bremsstrahlung Radiation. An electron is deflected by the presence of an atomic nucleus. It accelerates in the direction of the positive charge, and emits electromagnetic radiation. Credit: Andrades (2017)

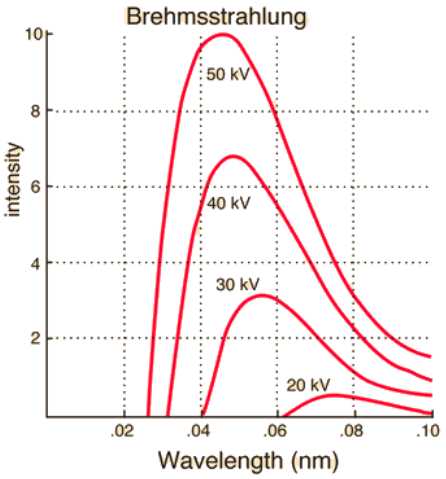

Figure 23: Bremsstrahlung Radiation Spectrum. For higher-energy incoming electrons the total intensity of the radiation is greater, and the peak of the emission is shorter-wavelength.
Credit: http://hyperphysics.phy-astr.gsu.edu/hbase/quantum/xrayc.html

Because the variables of electron velocity, impact parameter and atomic number can vary throughout the material, bremsstrahlung radiation is broadband in nature (Hecht, 1987, ch.3; Eberhard & Werner, 2004). The photon energy can be no greater than the kinetic energy of the incoming electrons (Eberhard & Werner, 2004):

$$E_{\gamma max} = h\nu_{max} = E_i \tag{16}$$

Very few of the photons are emitted with the very highest energies, near to the kinetic energy of the electron (Eberhard & Werner, 2004).

The spectrum of Bremsstrahlung radiation is shown in figure 23.

Evidence of bremsstrahlung radiation from the atmospheres of white dwarfs and the boundary layer of the accretion disc has been observed (O'Connell, 1973; Hoffman, 1974; Wood et al., 1995).

3.5 Cyclotron Radiation

A charged particle moving in a uniform magnetic field will experience a Lorentz force perpendicular to the velocity of the charge and the magnetic field, causing the charge to follow a circular path (Serway & Renner et al., 1985, ch.40; Reese, 1999, ch.20; Longair, 2011, ch.6). An electron in a magnetic field is diagrammed as a 3-d

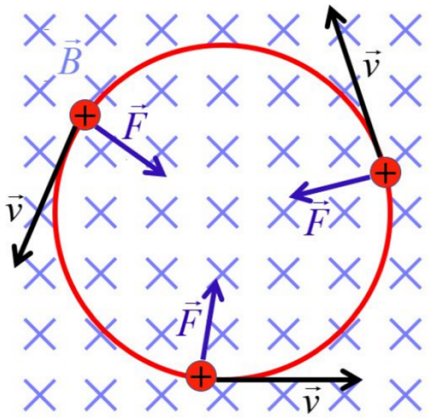

Figure 24: The orientation of the force, velocity, and field components of an electron in an magnetic field. An electron oscillates clockwise in a magnetic field $\overrightarrow{B}$ (light blue crosses) that points into the page. The velocity of the electron $\overrightarrow{v}$ (black arrows) is tangential to the motion of the charge, and the Lorentz force $\overrightarrow{F}$ (dark blue or arrows) points inwards. The path of the electron is shown in red. Credit: Kathryn Hadley, University of Oregon PHY213, http://www.khadley.com/Courses/Physics/ph_213/topics/Bfield/page4.html

surface in figure 24. The magnetic force is the source of centripetal acceleration, and so the charge will radiate (Ding, 2020).

The angular frequency of the charge determines the frequency of the radiation (Hecht, 1987, ch.3). The angular frequency depends on the charge and mass of the particle and the strength of the magnetic field in the following way (Ding, 2020):

$$\omega = \frac{qB}{m}$$

So for a collection of like charges, such as electrons, the frequency of emission depends only on the strength of the magnetic field:

$$\omega = \frac{e}{m_e}B$$

Hence, the frequency of the radiation is:

$$\nu = \frac{1}{2\pi}\frac{e}{m_e}B \tag{17}$$

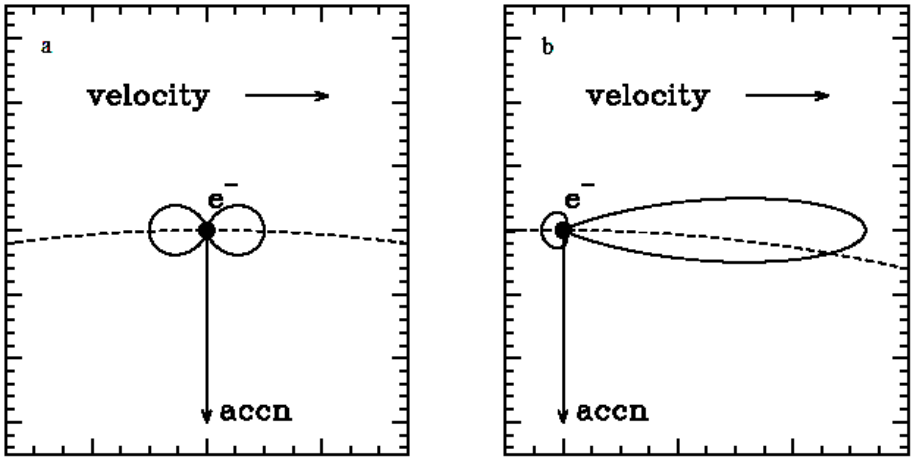

Figure 25: a) Cyclotron emission radiates in lobes forward and backward along the direction of the electron's velocity. b) Relativistic beaming, the combination of relativistic length contraction and Doppler shift, causes synchrotron radiation to radiate primarily in the forward direction.
Credit: http://www.astro.utu.fi/∼cflynn/astroII/l4.html

Therefore, in a uniform magnetic field, cyclotron radiation is monochromatic, though harmonics may be seen (Hecht, 1987, ch.3; Longair, 2011, ch.8).

Photons are emitted in lobes forwards and backwards in the direction of motion of the charged particle, as shown in figure 25a (Hecht, 1987, ch.3). In general, the radiation is elliptically polarized (Nava et al., 2016). The emission varies between linear and circular polarisation depending on the angle at which it is observed (Nava et al., 2016).

Cyclotron radiation is emitted by the accretion column of magnetic accreting white dwarfs, including IPs and polars, as electrons spiral around the magnetic field lines (Masters et al., 1977; West et al., 1987; Warner, 1995, ch.6; Kalomeni et al., 2005). The motion of a charged particle as it spirals around a magnetic field line is shown in figure 26.

3.6 Synchrotron Radiation

Synchrotron radiation is the relativistic limit of cyclotron radiation (Longair, 2011, ch.8). A charged particle moving at relativistic velocity encounters a magnetic field, causing it to move in a tight circle or spiral (Hecht, 1987, ch.3; Longair, 2011, ch.8). The acceleration of the electric charge causes high-frequency photons to be radiated (Longair, 2011, ch.8).

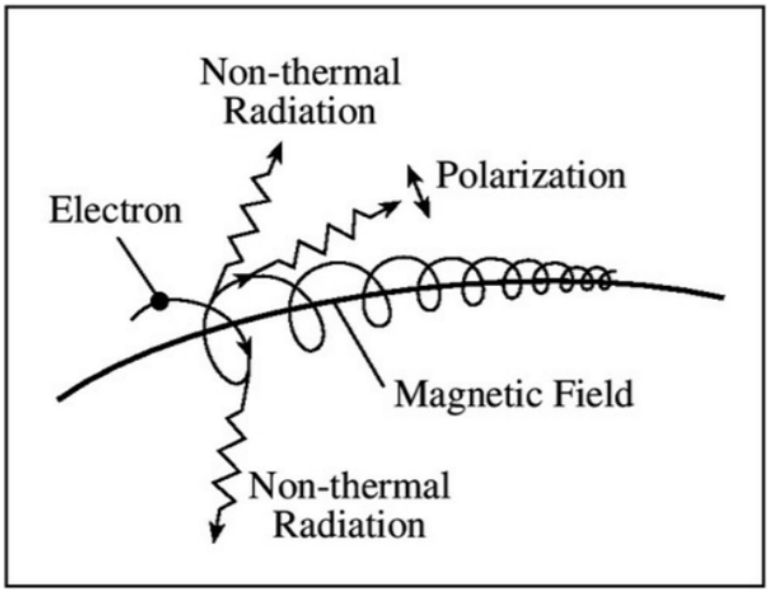

Figure 26: An electron emits electromagnetic radiation as it spirals around a magnetic field line. Credit: Professor Kenneth R. Lang, Tufts University, NASA's Cosmos, 2010

Because of relativistic length contraction, the forward lobe of emission is longer and narrower, and the backward emission lobe is shorter and broader (Hecht, 1987, ch.3; Longair, 2011, ch.8). A diagram of this is shown in figure 25b.

Because the motion of the electron is relativistic, the emission is Doppler shifted (Longair, 2011, ch.8). The forward emission is blue shifted and the backward emission is red shifted, hence the emission frequency is not the same as the angular frequency (Longair, 2011, ch.8).

The combination of these two effects, length contraction and Doppler shifting, is known as relativistic beaming, the result of which is that most of the energy is emitted in the direction of motion of the charge (Longair, 2011, ch.8). Because the beam is narrowed, the electromagnetic oscillation of the emission is no longer sinusoidal, the Fourier transform does not correspond to a single frequency, and the emission will not be monochromatic (Longair, 2011, ch.8). When the electrons become significantly relativistic, the energy radiated at higher harmonics increases, and the emission line at a given harmonic broadens, especially for higher harmonics, to the point that high harmonics are no longer discrete, and the emission spectrum becomes continuous (Longair, 2011, ch.8). As shown in figure 27, relativistic beaming causes distortion in the electromagnetic radiation away from a sinusoid, and this results

in emission at multiple frequencies. In figure 28 one can see how the broadening of high harmonics results in a continuous emission spectrum. Linear and logarithmic plots of the synchrotron radiation spectrum are shown in figures 29 and 30.

Synchrotron radiation is emitted by the jets of neutron stars and black holes in X-ray binaries (Bornak et al., 2008). In CVs, it is likely emitted by the jets of magnetic white dwarfs, as electrons spiral around the magnetic field lines (Rupen et al., 2008).

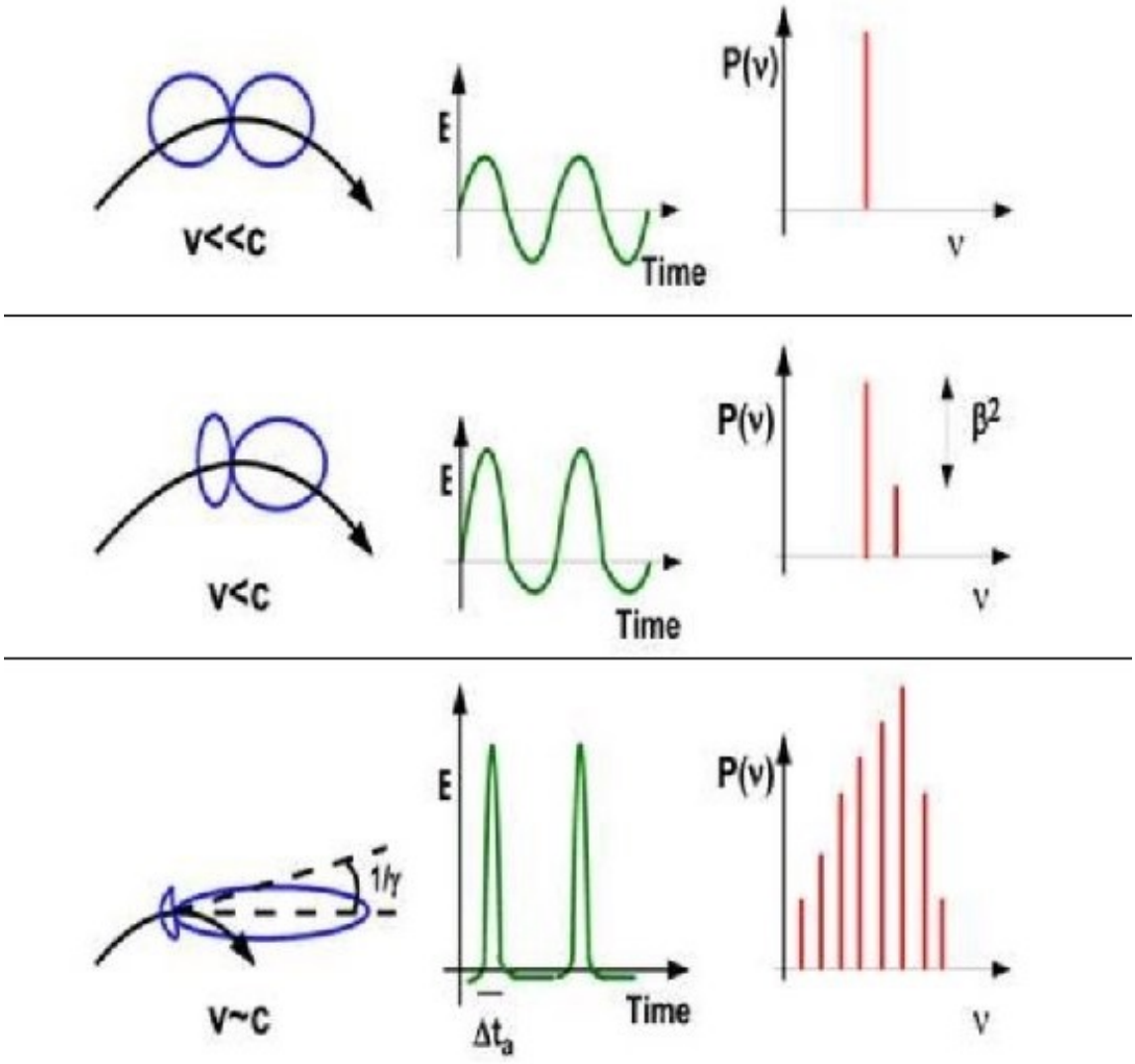

Figure 27: Cyclotron and Synchrotron Radiation Spectrum. Relativistic beaming causes the radiation seen by an observer to diverge from a sinusoid, the spectrum of emitted radiation diverges from a simple Dirac delta function, and the radiation is no longer monochromatic. Credit: https://slidetodoc.com/cyclotron-synchrotron-radiation-synchrotron-radiation-is-radiation-emerging/

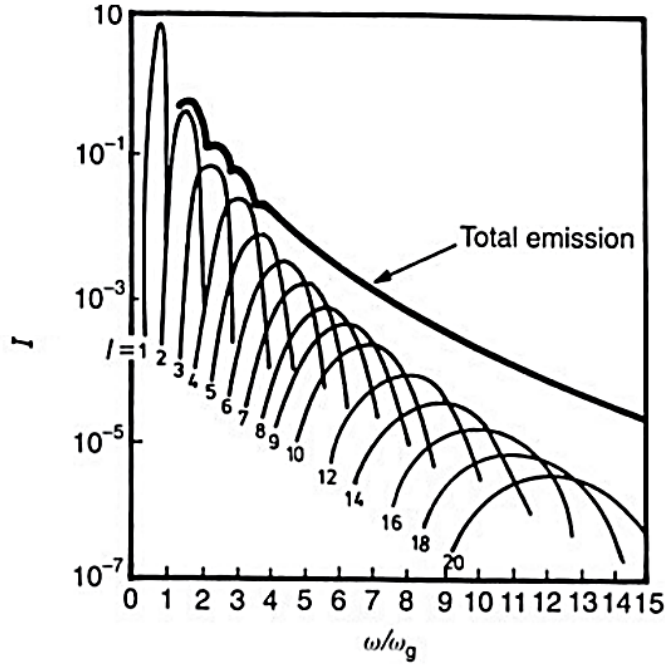

Figure 28: Relativistic beaming broadens the harmonics of synchrotron radiation to the point that higher harmonics are no longer distinct, resulting in a continuous emission spectrum. Credit: Longair (2011, ch.8)

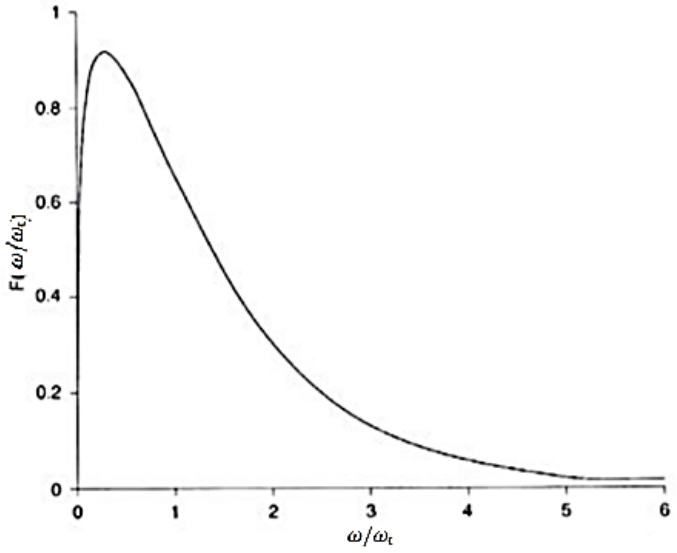

Figure 29: Linear plot of the synchrotron radiation spectrum. Credit: Longair (2011, ch.8)

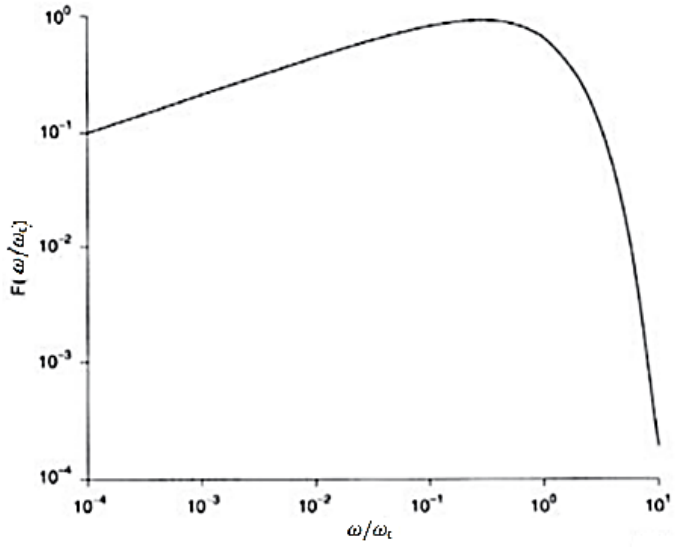

Figure 30: ogarithmic plot of the synchrotron radiation spectrum. Credit: Longair (2011, ch.8)

4 Methods

In this section I identify my data sources and describe my methods and code.

4.1 Data Archives

4.1.1 Barbara A. Mikulski Archive for Space Telescopes

mast

The NASA funded Barbara A. Mikulski Archive for Space Telescopes[8] (MAST) is an astronomical data archive focused on the optical, ultraviolet, and near-infrared wavelengths. It is located at the Space Telescope Science Institute (STScI) in Baltimore, Maryland, USA, and is one of the largest astronomical databases in the world, hosting data from over a dozen missions.

I used MAST to find spectral data from the *Extreme Ultraviolet Explorer*, *Far Ultraviolet Spectroscopic Explorer*, *International Ultraviolet Explorer*, *Neil Gehrels Swift Observatory*, *Berkeley Extreme and Far-ultraviolet Spectrometer*, *Wisconsin Ultraviolet Photo-Polarimeter Experiment*, *Johns Hopkins Ultraviolet Telescope*, *Tübingen Echelle Spectrograph* missions.

[8]https://mast.stsci.edu/portal/Mashup/Clients/Mast/Portal.html

4.1.2 NASA/IPAC InfraRed Science Archive

The NASA/IPAC InfraRed Science Archive (IRSA)[9] is a project at the NASA Infrared Processing and Analysis Center (IPAC), at the California Institute of Technology (Caltech) in Pasadena, California, USA. It is a portal to the science products of NASA's infrared and submillimeter missions.

IRSA was used to access data from the Two Micron All-Sky Survey, *Global Astrometric Interferometer for Astrophysics*, *Wide-field Infrared Survey Explorer*, *Spitzer Space Telescope*, Skymapper Southern Sky Survey, Panoramic Survey Telescope and Rapid Response System, *Hipparcos*, Sloan Digital Sky Survey, INT/WFC Photometric H-Alpha Survey of the Northern Galactic Plane, UKIRT Infrared Deep Sky Survey, Visible and Infrared Survey Telescope for Astronomy, *Galaxy Evolution Explorer*, Palomar Observatory Sky Survey II catalogues.

4.1.3 High Energy Astrophysics Science Archive Research Center

The High Energy Astrophysics Science Archive Research Center (HEASARC)[10] is a member of the NASA Astronomical Virtual Observatories (NAVO) and is the primary archive for the missions of several space agencies including NASA. The HEASARC archive contains data in the extreme-ultraviolet, X-ray, and gamma-ray bands, as well as cosmic microwave background (CMB) radiation data in the submillimeter, millimeter and centimeter wavelength bands. I used the HEASARC archive to access *Röntgensatellit* and *X-ray Multi-Mirror Mission* point data (denoted by large purple dots in Section 6.1.2).

4.1.4 XMM-Newton Science Archive

I used ESA's XMM-Newton Science Archive (XSA)[11] to access XMM-Newton spectral data (denoted by an orange spectrum in Section 6.1.2). XSA provides access to data from the XMM-Newton mission, and was developed for the XMM-Newton project by the ESAC Science Data Centre (ESDC).

XMM data in this study was provided both by XSA, which provided a flux density spectrum over a range of frequencies, and HEASARC, which provided point-form data at a single frequency. Data for some systems was not available from either High Energy Astrophysics Science Archive Research Center and/or XMM-Newton Science Archive, and as such both data sources have been used.

[9] https://irsa.ipac.caltech.edu/frontpage/
[10] https://heasarc.gsfc.nasa.gov/
[11] http://nxsa.esac.esa.int/nxsa-web/search

4.2 Data Sources

Table 1 gives some properties of the data sources used to collect data for the systems in this study. Table 2 shows which systems in this study include data from which data sources.

[12]Bowyer (1996)
[13]Moos et al. (2004)
[14]Moos & Sonneborn (2006)
[15]Showstack (2007)
[16]Riegler (1998)
[17]Krimm et al. (2004)
[18]Gehrels et al. (2004); Savaglio & Grothkopf (2013)
[19]Bowyer & Hurwitz (1990)
[20]Grewling (2002)
[21]Skrutskie et al. (2006)
[22]Wright et al. (2010)
[23]Lindegren & Söderhjelm (1982); Rouan (2011)
[24]ESA (1997)
[25]Bianchi et al. (1997)
[26]Burgarella et al. (2003)
[27]Werner et al. (2004)
[28]Keller et al. (2007)
[29]Hodapp et al. (2004a,b)
[30]Gunn & Weinberg (1995)
[31]Drew et al. (2005a)
[32]Lawrence (2013)
[33]Lawrence et al. (2007)
[34]Iye & Yamashita (2000)
[35]Arnaboldi (2010)
[36]Reid et al. (1991)
[37]Reid & Djorgovski (1993)
[38]Ridpath (2012)
[39]Christy et al. (2022)
[40]Prieto et al. (2011)
[41]Trümper (1982)
[42]Georgantopoulos et al. (1991)
[43]Trümper (1999)
[44]de Blok et al. (2009)
[45]Woudt (2021)
[46]Thompson et al. (1980)

Table 1: Properties of the data sources. Properties that are not referenced in Section 4.2 are referenced in the footnotes.

Name	Waveband	Spectral Range	Operation Period
EUVE	EUV	100, 200, 400, 600 Å[12]	Jul 1992 [12] - Jan 1993 [12]
FUSE	FUV	905 – 1187 Å[13]	1 Dec 1999[14] - 18 Oct 2007[15]
IUE	UV	1150 - 3200 Å	Jan 1978 - late 1996[16]
Swift	Visible to γ-ray	7 eV - 150 keV[17]	late 2004[18] - present
BEFS	EUV and FUV	390 - 1200 Å[19]	12 - 26 Sep 1993 & 19 Nov - 7 Dec 1996
WUPPE	UV	1400 - 3400 Å	9 days in Dec 1990
HUT	UV	450 - 1800 Å	9 days in Dec 1990
TUES	UV	900 - 1400 Å	19 Nov - 7 Dec 1996[20]
2MASS	NIR	1.25 μm, 1.65 μm, and 2.16 μm	Jun 1997[21] - Feb 2001[21]
WISE	IR	3.4 μm, 4.6 μm, 12 μm and 22 μm	14 Jan 2010[22]- Nov 2010[22]
Hipparcos	Visible	B: 440 ± 98 nm, V: 550 ± 89 nm[23]	Nov 1989[24] - Mar 1993
GAIA	Visible	300 – 1000 nm	Dec 2013 - present
GALEX	FUV to NUV	1300 - 3000 Å[25]	May 2003[26] - Jun 2013
Spitzer	IR	3.6 - 160 μm[27]	Aug 2003 - Jan 2020
SkyMapper	UV	u, v_s, g, r, i, z: 0.32 - 0.95 μm[28]	late 2007[28] - present
PanSTARRS	Visible	g: 402 – 552 nm r: 552 – 691 nm i: 691 – 818 nm z: 818 – 922 nm y_1: 948 – 1060 nm y_2: 970 – 1028 nm w_1: 402 – 818 nm w_2: 522 – 818 nm[29]	2007[28] - present
SDSS	Visible	u_0: 3540 Å g_0: 4760 Å r_0: 6280 Å i_0: 7690 Å z_0: 9250 Å[30]	May 2000 - present
IPHAS	IR to Visible	r′: 6240 Å, Hα: 6568 Å, i′: 7743 Å[31]	Aug 2003[31] - present
UKIDSS	IR	Z: 0.8817 ± 0.093 nm Y: 1.0305 ± 0.102 nm J: 1.2483 ± 0.159 nm H: 1.6313 ± 0.292 nm K: 2.2010 ± 0.351 nm[33]	May 2005[33] - 2012[32]
Subaru	NUV to mid-IR	0.3 to 30 μm	Oct 2000[34] - present
VISTA	NIR	Z, Y, J, H, K_s: 0.88 - 2.15 μm[35]	1 Apr 2010[35] - present
POSS-II	Visible	3900 - 9000 Å[36]	mid 1985[37] - 2000[38]
ASAS-SN	Visible	g: 481 nm, V: 551 nm[39]	2011[40] - present
ROSAT	X-ray to XUV	0.1 - 2 keV[41]	1990[42] - 12 Feb 1999[43]
XMM	X-ray	0.1 and 10 keV	Dec 1999 - present
ThunderKAT	Radio	0.58 - 2.0 GHz, 8.5 - 15 GHz[44]	2018[45] - 2022[45]
VLA	Radio	1.34 - 1.73, 4.5 - 5.0, 14.4 - 15.4, 22 - 24 GHz[46]	late 1980[46] - present

Table 2: The binary systems in this study and their data sources. 'x' indicates which systems in this study include data from which data sources.

	V603 Aql	V3885 Sgr	IX Vel	UX UMa	SU UMa	U Gem	Z Cam	SS Cyg	DQ Her	DO Dra	AE Aqr	EX Hya	AM Her	AR UMa	BL Hyi	VV Pup
EUVE			x					x					x	x	x	x
FUSE	x	x	x	x	x	x	x	x	x	x	x		x	x	x	x
IUE	x	x	x	x	x		x	x	x	x		x	x	x	x	x
Swift																
BEFS		x	x				x				x		x			
WUPPE			x				x	x					x			
HUT			x	x		x	x	x					x			
TUES			x				x						x			
2MASS	x	x	x	x	x	x	x	x	x	x	x	x	x	x	x	x
WISE	x	x	x	x	x	x	x	x	x	x	x	x	x	x	x	x
Hipparcos	x	x	x	x			x	x		x	x				x	
GAIA	x	x	x	x	x	x	x	x	x	x	x	x	x	x	x	x
GALEX				x	x	x	x		x	x	x		x	x	x	
Spitzer	x		x													
SkyMapper		x									x	x			x	x
PanSTARRS	x		x	x	x	x	x	x	x	x	x	x	x	x		x
SDSS	x	x	x	x	x	x	x	x	x	x	x		x	x		
IPHAS	x		x													
UKIDSS	x		x			x					x					
Subaru	x	x	x								x					
VISTA		x									x	x				x
POSS-II					x	x			x	x	x	x	x	x	x	x
ASAS-SN	x	x	x	x	x	x	x	x	x	x	x	x	x	x	x	x
ROSAT	x	x	x	x	x	x	x		x	x		x			x	x
XMM	x	x	x	x	x	x	x			x	x	x	x	x	x	x
ThunderKAT	x	x	x													
VLA	x	x			x	x	x	x	x		x	x	x	x		x

4.2.1 *Extreme Ultraviolet Explorer*

The *Extreme Ultraviolet Explorer* (*EUVE*) was a NASA mission to search for and observe extreme ultraviolet (EUV) radiation sources (Bowyer, 1982; Malina et al., 1982). The mission consisted of three telescopes which were each sensitive to different EUV frequencies, as well as a fourth telescope that performed a high-sensitivity search of limited region of the sky (Bowyer, 1982; Malina et al., 1982). For six months the *EUVE* performed an all-sky EUV survey, during which it detected hundreds of objects, and then it performed pointed observations of specific astronomical sources (Bowyer, 1982; Malina et al., 1982).

4.2.2 *Far Ultraviolet Spectroscopic Explorer*

The *Far Ultraviolet Spectroscopic Explorer* (*FUSE*) was a NASA astrophysics satellite that performed high-resolution far-ultraviolet observations (Conrad et al., 2000). The telescope launched in June 1999 and has obtained spectra of bright quasars, Seyfert galaxies, and nearby hot stars, as well as galactic halos, planetary atmospheres, cool stellar atmospheres and the interstellar medium (Weiler and Stencel, 1982; Conrad et al., 2000). *FUSE* crucially extended spectroscopic abilities to 100 Å, into a spectral region that contains atomic transitions that can be used as probes for many astronomical phenomena, some of which can only be interrogated by spectroscopy at wavelengths below 1216 Å (Weiler and Stencel, 1982; Cash, 1984; Conrad et al., 2000).

4.2.3 *International Ultraviolet Explorer*

The *International Ultraviolet Explorer* (*IUE*) was astronomical observatory satellite with a 45 cm spectrographic telescope that covered a wavelength range 1150 Å - 3200 Å (Macchetto, 1976; IUE, 1978). It was a joint undertaking by NASA, ESA and The UK Science Research Council, and was launched to an elliptical geosynchronous orbit above the Atlantic Ocean in January 1978 (Macchetto, 1976; Dial & Cooley, 1977; IUE, 1978). The goals of the *IUE* included the study of gas streams in and around some binary systems, and observing faint stars, galaxies and quasars and the spectra of planets and comets, as well as objects known to have variable spectra (Macchetto, 1976). Its primary goal was to observe the ultraviolet spectra of stars, galaxies, and the brighter gaseous and planetary nebulae (Dial & Cooley, 1977).

4.2.4 *Neil Gehrels Swift Observatory*

The *Neil Gehrels Swift Observatory* (*Swift*) is a multiwavelength transient observatory that is part of NASA's medium explorer (MIDEX) program (Gehrels, 1999;

Marshall, 2003). The Swift mission observes gamma-ray bursts (GRBs) and their afterglows in an effort to investigate their origin and probe the early Universe (Gehrels, 1999). It consists of the *Burst Alert Telescope* (*BAT*), which images and detects GRBs, the *X-ray Telescope* (*XRT*), a multiwavelength X-ray telescope, and the *Ultra-Violet/Optical Telescope* (*UVOT*), which detects the early UV and optical photons of GRB afterglows (Marshall, 2003). *BAT* is able to detect hundreds of GRBs every year, and then *XRT* and *UVOT* observe them and their afterglows (Marshall, 2003).

4.2.5 *Berkeley Extreme and Far-ultraviolet Spectrometer*

The *Berkeley Extreme and Far-ultraviolet Spectrometer* (*BEFS*) flew on the *Orbiting and Retrievable Far and Extreme Ultraviolet Spectrograph (ORFEUS)-SPAS I* and *II* space shuttle missions, in 1993 and 1996 (Bowyer & Hurwitz, 1990; Dixon, 2002). It returned high-resolution spectra of point sources in the 390 Å - 1200 Å wavelength range (Bowyer & Hurwitz, 1990).

4.2.6 *Wisconsin Ultraviolet Photo-Polarimeter Experiment*

The *Wisconsin Ultraviolet Photo-Polarimeter Experiment* (*WUPPE*) was one of three ultraviolet telescopes aboard the *ASTRO-1* shuttle Spacelab mission in December 1990 (Code, 1991; Nordsieck et al., 1991a,b). During the nine day mission it made observations of Be stars, rapid rotators, interstellar extinction probes, polarized supergiants, a magnetic white dwarf, a reflection nebula, and a Seyfert galaxy, and obtained data on ultraviolet interstellar polarisation (Code, 1991; Nordsieck et al., 1991a). *WUPPE* observed in the 1400 Å - 3400 Å wavelength range, and was more sensitive than pre-launch expectations (Code, 1991; Nordsieck et al., 1991a,b).

4.2.7 *Johns Hopkins Ultraviolet Telescope*

The *Johns Hopkins Ultraviolet Telescope* (*HUT*) was a 0.9 meter (Davidsen et al., 1981) telescope with a prime focus far-ultraviolet spectrophotometry telescope of the Johns Hopkins University (Davidsen et al., 1981). It obtained moderate resolution spectra in the 450 Å - 1800 Å wavelength range, emphasizing the 900 Å - 1200 Å spectral region (Davidsen et al., 1981; Davidsen & Fountain, 1985). It was launched on the *ASTRO-1* mission in 1990, and was primarily devoted to the study of quasars and active galactic nuclei (AGNs), as well as observations of Halley's Comet, the planets, distant galaxies and quasars (Davidsen et al., 1981; Davidsen, 1990).

4.2.8 *Tübingen Echelle Spectrograph*

The *Tübingen Echelle Spectrograph* (*TUES*) was designed and managed at the University of Tübingen, Germany (Grewling, 2002). It flew on the Orbiting and *Retrievable Far and Extreme Ultraviolet Spectrograph (ORFEUS)-SPAS II* space shuttle mission in 1996 (Grewling, 2002). *TUES* observed in the 900 Å - 1400 Å wavelength range, returning 239 spectra of 62 targets (Grewling, 2002).

4.2.9 Two Micron All-Sky Survey

The Two Micron All-Sky Survey (2MASS) is a near-infrared survey of the entire sky at 1.25 μm, 1.65 μm, and 2.16 μm (Cutri et al., 2003; Skrutskie et al., 2006). It took place between 1997 and 2001 at the U.S. Fred Lawrence Whipple Observatory on Mount Hopkins, Arizona, USA, and at the Cerro Tololo Inter-American Observatory in Chile, in order to survey both hemispheres (Cutri et al., 2003; Skrutskie et al., 2006). 2MASS consists of two 1.3 meter telescopes and is conducted by the University of Massachusetts and IPAC (Cutri et al., 2003; Skrutskie et al., 2006).

4.2.10 *Wide-field Infrared Survey Explorer*

IPAC's *Wide-field Infrared Survey Explorer* (*WISE*), launched in December 2009, is a 40 cm infrared telescope that provides an all-sky survey at 3.4 μm, 4.6 μm, 12 μm and 22 μm wavelengths (Duval et al., 2004; Wright et al., 2010). *WISE* extended *2MASS* into the thermal infrared, with the goal of detecting luminous galaxies, nearby stars, and main belt asteroids larger than 3 km in diameter (Duval et al., 2004).

4.2.11 *Hipparcos*

Hipparcos was a scientific satellite of the European Space Agency (ESA), that was dedicated to astrometry and photometry (ESA, 1997). *Hipparcos* was the predecessor of the *GAIA* mission. It launched in August 1989 and operated until March 1993 (ESA, 1997).

4.2.12 *Global Astrometric Interferometer for Astrophysics*

The ESA's *Global Astrometric Interferometer for Astrophysics*[47] (*GAIA*) is designed for global astrometry, and is the successor to the *Hipparcos* mission (Perryman et al., 2001; Brown, 2013). Its objective is to produce a three-dimensional census of the Milky Way by surveying more than a billion objects and precisely characterizing their position, distance and proper motion (Perryman et al., 2001). This will allow

[47] https://gea.esac.esa.int/archive/

scientists to study the origin, evolutionary history and subsequent evolution of the Milky Way (Perryman et al., 2001). *GAIA* targets objects brighter than magnitude 20, mainly stars, but also minor Solar System bodies, extra-Solar planetary systems, nearby galaxies, and quasars (Perryman et al., 2001; Brown, 2013). These objects represent about 1% of the Galactic population (Perryman et al., 2001). *GAIA* observes in a broad photometric band that covers most of the visual range (Brown, 2013). It was launched in December 2013 from Kourou in French Guiana and is expected to operate until 2022 (Brown, 2013). The spacecraft orbits around the Sun–Earth L2 Lagrangian point (Perryman et al., 2001; Brown, 2013).

4.2.13 *Galaxy Evolution Explorer*

The *Galaxy Evolution Explorer* (*GALEX*) was an NASA space telescope that observed in the ultraviolet (Bianchi et al., 1997; Burgarella et al., 2003). Its mission was to produce an all-sky Ultraviolet map, and study galactic evolution and the history of star formation at distances up to $z = 2$ (Bianchi et al., 1997; Millard et al., 2001). It provided measurements of redshift, extinction, luminosity, and star formation rate of thousands of galaxies (Bianchi et al., 1997). *GALEX* launched in April 2003 and was decommissioned in June 2013 (Burgarella et al., 2003; Shiao et al., 2014).

4.2.14 *Spitzer Space Telescope*

The *Spitzer Space Telescope* is a NASA infrared observatory operated by the Spitzer Science Center (SSC) at Caltech (Werner et al., 2004). It carried an Infrared Array Camera (IRAC), an Infrared Spectrograph (IRS), and the Multiband Infrared Photometer for Spitzer (MIPS) (Werner et al., 2004). Spitzer was launched in August 2003 from Florida's Cape Canaveral Air Force Base to an Earth-trailing orbit, and retired in January 2020 (Werner et al., 2004; Miller et al., 2020).

4.2.15 Skymapper Southern Sky Survey

Skymapper Southern Sky Survey is a 1.3 m wide-field telescope at Siding Spring Observatory, Coonabarabran, New South Wales, Australia (Schmidt et al., 2005; Keller et al., 2007). The project is led by the Research School of Astronomy and Astrophysics at the Australian National University (Keller et al., 2007).

SkyMapper records the brightness and position of Southern stars and galaxies between 8 and 22 mag (Keller et al., 2007). The goal of the project is to produce a deep, multi-colour digital record of the entire Southern Sky (Keller et al., 2007).

4.2.16 Panoramic Survey Telescope and Rapid Response System

The Panoramic Survey Telescope and Rapid Response System (PanSTARRS) is a project of the University of Hawai'i Institute for Astronomy, and is located at Haleakala Observatory, Haleakala, Maui, Hawai'i (Chambers, 2004; Kaiser, 2005). It consists of an array of four 1.8 m telescopes that survey in the optical and infrared (Kaiser, 2005).

PanSTARRS' primary mission is to detect Near Earth Objects and Potentially Hazardous Asteroids (Kaiser, 2005). It also surveys the entire sky and catalogues objects brighter than magnitude 24 (Kaiser, 2005).

Data from PanSTARRS aids scientists in the study of the Solar System and the Milky Way, and will have a substantial impact on the study of the outer Solar System and the Kuiper belt (Jewitt, 2003; Kaiser, 2005).

4.2.17 Sloan Digital Sky Survey

The Sloan Digital Sky Survey (SDSS) is a photometric and spectroscopic redshift survey of π sr of the Northern Galactic cap, and a 200 sq.deg strip of the southern Galactic cap (Gunn & Weinberg, 1995; Loveday, 1999; Margon, 1999; York et al., 2000). Since it began regular survey operations in May 2000, it has obtained spectra of about 1 million galaxies and over 100,000 quasars, with the aim of constructing a map of the local universe, as well as observing some very high redshift objects (Loveday, 1999; Margon, 1999; York et al., 2000).

4.2.18 INT/WFC Photometric H-Alpha Survey of the Northern Galactic Plane

The INT/WFC Photometric H-Alpha Survey of the Northern Galactic Plane (IPHAS) is a survey of the Northern Milky Way (Walton et al., 2004; Drew et al., 2005a). It surveys at red and longer wavelengths and uses two broad-band filters and a narrow H-alpha filter to image and identify objects in our galaxy that are characterized by strong emission in H-alpha (Drew et al., 2005a).

H-alpha emission traces diffuse ionized nebulae and is a strong signature of active stars, interacting binaries, supergiants, and supernova remnants and progenitors (Walton et al., 2004; Drew et al., 2005a). Such objects generally represent short but important stellar evolutionary phases (Walton et al., 2004; Drew et al., 2005a). This H-alpha survey to identify and study these objects will help scientists understand these crucial evolutionary stages (Walton et al., 2004).

IPHAS is conducted on the 2.5 meter Isaac Newton Telescope's Wide Field Camera in the Canary Islands, Spain (Walton et al., 2004; Drew et al., 2005a).

4.2.19 UKIRT Infrared Deep Sky Survey

The UKIRT Infrared Deep Sky Survey (UKIDSS) is a near-infrared survey conducted using the Wide Field Camera (WFCAM) on the UK Infrared Telescope (UKIRT) on Mauna Kea, Hilo, Big Island, Hawai'i (Warren, 2002). UKIDSS is the successor to *2MASS* (Warren, 2002). It consists of five surveys: the Large Area Survey (LAS), Galactic Plane Survey (GPS), Galactic Clusters Survey (GCS), Deep Extragalactic Survey (DXS), and Ultra Deep Survey (UDS) (Warren, 2002). These surveys will collectively cover 7500 sq.deg of the Northern sky to a depth three magnitudes deeper than 2MASS, produce a panoramic atlas of the Milky Way disk, image nearby stellar clusters and study galaxies at high redshifts (Warren, 2002).

The goals of UKIDSS include the discovery of young stellar objects, brown dwarfs, and high redshift quasars further than $z = 7$, as well as determining the stellar-mass function, measuring the abundance of galaxy clusters at $1 < z < 1.5$, and mapping the Milky Way to several kiloparsecs (Warren, 2002).

4.2.20 Subaru Telescope

The Subaru Telescope (Japan National Large Telescope, JNLT) is an 8.2 m optical and infrared telescope of the National Astronomical Observatory of Japan (NAOJ), located on Mauna Kea, Hilo, Big Island, Hawai'i (Hayashi et al., 1992; Sekiguchi, 1999). It covers a spectral range of 0.3 μm to 30 μm, from near-ultraviolet to mid-infrared wavelengths (Hayashi et al., 1992).

The Subaru project studies individual components in the Local Group, in particular it can resolve the light of galaxies in the Local Group into individual stars and determine their physical properties (Sekiguchi, 1999). It also provides spectroscopic data for faint objects (Sekiguchi, 1999).

4.2.21 Visible and Infrared Survey Telescope for Astronomy

The Visible and Infrared Survey Telescope for Astronomy (VISTA) is a 4 m wide-field near-infrared Southern Hemisphere telescope operated by the European Southern Observatory (ESO) and located at the Paranal Observatory in Chile (Arnaboldi, 2010).

VISTA has several galactic and extra-galactic scientific goals, including the study of galactic evolution, high redshift AGNs, high-proper motion stars, the early Universe at redshifts $6 < z < 10$, and the evolution of stellar populations in the Magellanic Clouds, as well as the study of baryonic acoustic oscillations (BAOs) in order to geometrically constrain our models Dark Energy, and the creation of a complete census

of the Southern Sky and a 3-dimensional map of the Galactic bulge (Arnaboldi, 2010).

4.2.22 Palomar Observatory Sky Survey II

The National Geographic Society-Palomar Observatory Sky Survey (POSS-I) began observations in 1949 on the 1.2 m Oschin telescope, located on Palomar Mountain, San Diego, California, USA (Reid et al., 1991). This was the first of the photographic sky surveys produced by large Schmidt telescopes (Reid et al., 1991). Given the scientific success of this project, a new survey of the Northern Sky operated from the Palomar Observatory was undertaken: POSS-II (Reid et al., 1991).

POSS-II has provided a proper motion catalogue of the Northern Sky and has helped astronomers to discover and study many different kinds of objects including planetary nebulae, star clusters and thousands of galaxies (Picard, 1991; Reid et al., 1991).

4.2.23 All Sky Automated Survey for SuperNovae

The All Sky Automated Survey for SuperNovae[48] (ASAS-SN) consists of several facilities distributed around the globe, each of which comprises four individual telescopes (Bersier, 2016). It is based on the successful All-Sky Automated Survey (ASAS), a project to monitor the entire sky, but the focus of ASAS-SN is nearby supernovae (Bersier, 2016). Discoveries also include tidal distribution events, dwarf stars, cataclysmic variables and active galactic nuclei (Bersier, 2016).

4.2.24 *Röntgensatellit*

The *Röntgensatellit* (*ROSAT*) began observations in 1990 and was the first all-sky X-ray survey (Aschenbach et al., 1981; Trümper, 1982; Prieto et al., 2011). It discovered more than 100 000 X-ray sources, including objects ranging from nearby stars to distant quasars (Aschenbach et al., 1981; Trümper, 1982). In addition to its all-sky survey, *ROSAT* performed pointed observations of selected targets (Aschenbach et al., 1981; Trümper, 1982). *ROSAT* consists of a main telescope with a 83 cm aperture, as well as a Wide Field Camera that can observe into the extreme ultraviolet (Aschenbach et al., 1981; Trümper, 1982).

4.2.25 *X-ray Multi-Mirror Mission*

The ESA's *X-ray Multi-Mirror Mission* (*XMM*) is an X-ray space observatory tasked with performing high-resolution spectroscopic observations of X-ray sources between

[48] https://asas-sn.osu.edu/

0.1 and 10 keV, allowing for the study of many classes of objects (Koch-Miramond, 1985; Aschenbach et al., 1989). It consists of two arrays of grazing incidence Wolter type 1 telescopes and has a ground station located in Perth, Australia. It was launched in December 1999 to a highly elliptical orbit (Koch-Miramond, 1985; Schuerenberg, 1989; Jansen, 1999).

4.2.26 HUNt for Dynamic and Explosive Radio transients with meerKAT

MeerKAT is a precursor radio telescope to the Square Kilometer Array (SKA) at the Karoo radio astronomy reserve (Schröder et al., 2009). It is the most sensitive gigaHertz frequency telescope in the Southern Hemisphere (Booth et al., 2009).

The HUNt for Dynamic and Explosive Radio transients with meerKAT (ThunderKAT) is a MeerKAT programme that searches for transients in the image plane (Fender et al., 2016). Almost all explosive phenomena and high-energy astrophysical processes in the universe emit transient radio waves (Fender et al., 2016). ThunderKAT observes radio emissions with the goal of finding, identifying and understanding such phenomena (Fender et al., 2016; Woudt, 2021). Observed phenomena include X-ray binaries, tidal disruption events, ultraluminous X-ray sources, cataclysmic variables, supernovae, and gamma-ray bursts, among many others (Fender et al., 2016).

Hewitt (2020) made observations of several cataclysmic variables using the MeerKAT radio interferometer as part of ThunderKAT. The observations were centred at 1284 MHz.

4.2.27 Karl G. Jansky Very Large Array

The Karl G. Jansky Very Large Array (VLA) is a centimeter-wavelength radio astronomy observatory designed by the National Radio Astronomy Observatory (NRAO) and located in central New Mexico, USA (Heeschen, 1967; Burton, 1974; Heeschen, 1975). It consists of 27 radio antennas, each of which is 25 meters in diameter and is movable along the 21 km arms of a Y-configuration (Heeschen, 1967; Burton, 1974). The data from the antennas is combined by Earth-rotation aperture synthesis to synthesize an aperture of up to 40 km in diameter (Heeschen, 1967; Burton, 1974; Heeschen, 1975).

Coppejans et al. (2015) conducted a VLA survey of four close and optically-bright nova-like CVs at 6 GHz. Three of the selected CVs were successfully detected. Deanne L. Coppejans[3] also kindly provided additional radio data, with contributions from Barrett et al. (2017).

Barrett et al. (2020) used the VLA to observe 122 magnetic cataclysmic variables (mCVs), of which 33 were reported in 3 frequency bands, $4-6$, $8-10$, and $20-22$ GHz. Bastian (1987) utilised the VLA to observe eighteen MCV systems, including three of the systems analysed in this study.

4.3 Data Processing

In figures 36 - 51 (Section 6.1.2) flux density, F_ν, in units of Jy = 10^{-23} s^{-1} cm^{-2} Hz^{-1}, is plotted against frequency, ν, in units of Hz. Both of these axes are logarithmic.

The data provided by MAST was in the form of wavelength flux density, F_λ, (energy per unit surface area per unit wavelength), and had to be converted to frequency flux density, F_ν, (energy per unit surface area per unit frequency) using equation 18.

$$F_\nu[\text{Jy}] = \frac{\text{F}_\lambda[\text{erg s}^{-1}\ \text{cm}^{-2}\ \text{Å}^{-1}] \times \lambda[\text{Å}]^2 \times 10^{23}}{\text{c}[\text{Å s}^{-1}]} \tag{18}$$

Data provided by IRSA had to be filtered into the different catalogues. Frequency was given in GHz, and had to be converted to Hz.

Radio luminosity data provided by Deanne L. Coppejans was given in units of $erg.s^{-1}.Hz^{-1}$, and converted to flux density using equation 19, where d is the distance between the CV and the observer.

$$F = \frac{L}{4\pi d^2}$$

$$F_\nu[\text{Jy}] = \frac{L[\text{erg s}^{-1}\ \text{Hz}^{-1}]}{4\pi d[\text{cm}]^2 \times 10^{23}} \tag{19}$$

To retrieve *ROSAT* and *XMM* data, HEASARC's *X-ray, Gamma-Ray, and EUV Source Finder*[49] tool was used to find the count rate, the *nH Column Density*[50] tool was used to calculate the Galactic nH, and the *WebPIMMS*[51] tool was then used to calculate flux from count rate, which was given in units of $ergs.cm^{-2}.s^{-1}$, with a thermal bremsstrahlung estimated at 10kev. The value of this parameter had no significant effect on results. To get flux density, the result was integrated over the frequency domain. For a sufficiently narrow frequency domain, the flux density can be calculated by equation 20.

[49] https://heasarc.gsfc.nasa.gov/cgi-bin/Tools/high_energy_source/high_energy_source.pl
[50] https://heasarc.gsfc.nasa.gov/cgi-bin/Tools/w3nh/w3nh.pl
[51] https://heasarc.gsfc.nasa.gov/cgi-bin/Tools/w3pimms/w3pimms.pl

$$F_\nu = \frac{F}{\Delta\nu} \tag{20}$$

XMM data was provided by XSA in the form of fixed counts (γ) in units of photons.cm^{-2}s^{-1}Å^{-1} over wavelength (λ) in Angstroms:

$$\gamma \ [\mathrm{cm^{-2}s^{-1}\AA^{-1}}]$$

I multiply by the wavelength:

$$\gamma \ [\mathrm{cm^{-2}s^{-1}\AA^{-1}}] \times \lambda \ [\mathrm{\AA}] = \gamma\lambda \ [\mathrm{cm^{-2}s^{-1}}]$$

and I divide by frequency:

$$\gamma\lambda \ [\mathrm{cm^{-2}s^{-1}}] \div \nu \ [\mathrm{Hz}] = \gamma\lambda\nu^{-1} \ [\mathrm{cm^{-2}s^{-1}Hz^{-1}}]$$

I multiply by $h\nu$ to get the energy of the photons:

$$\gamma\lambda\nu^{-1} \ [\mathrm{cm^{-2}s^{-1}Hz^{-1}}] \times h\nu \ [\mathrm{J}] = \gamma\lambda\nu^{-1}h\nu \ [\mathrm{J.cm^{-2}s^{-1}Hz^{-1}}] = \gamma\lambda h \ [\mathrm{J.cm^{-2}s^{-1}Hz^{-1}}]$$

and convert energy to units of ergs:

$$\gamma\lambda h \ [\mathrm{J.cm^{-2}s^{-1}Hz^{-1}}] \times 10^7 = \gamma\lambda h \ [\mathrm{erg.cm^{-2}s^{-1}Hz^{-1}}]$$

I then multiply by 10^{23} to get flux density in Jansky:

$$\gamma\lambda h \ [\mathrm{erg.cm^{-2}s^{-1}Hz^{-1}}] \times 10^{23} = \gamma\lambda h \ [10^{-23} \times \mathrm{erg.cm^{-2}s^{-1}Hz^{-1}}] = F_\nu \ [\mathrm{Jy}]$$

The overall calculation performed was:

$$F_\nu[\mathrm{Jy}] = 10^{23} \times \gamma\lambda h \times 10^7 \ [10^{-23} \ \times \mathrm{erg.cm^{-2}s^{-1}Hz^{-1}}] \tag{21}$$

ASAS-SN data was provided in units of milliJansky, and converted into Jansky, and ThanderKAT data from Hewitt (2020) was in units of microJansky and was converted to Jansky.

4.4 Algorithms

4.4.1 Primary Spectra

I plotted the spectra of the primaries as blackbodies of given temperature. These temperatures are shown in table 3. I used the *astropy.modeling.blackbody.blackbody_nu()* function to calculate the spectrum. This function takes a range of frequencies in Hertz and the blackbody temperature in Kelvin as input parameters, and outputs the flux in units of erg Å^{-1} cm^{-2} s^{-1} sr^{-1}. I multiplied by solid angle, as given in equation 7, and by 10^{23} to convert this to Jansky.

The radius of the white dwarf was calculated using the white dwarf mass-radius relation, equation 4. This spectrum was subtracted from the spectral data of the system.

4.4.2 Secondary Spectra

The spectra of the secondaries were plotted in the same way as in Section 4.4.1. Using the orbital periods of the systems, the temperatures and stellar radii of the secondaries were obtained from table 2 of Knigge et al. (2011), and are given in table 3. This spectrum is also subtracted from the spectral data of the system.

The temperatures and stellar radii of the secondaries of Z Cam and SS Cyg could not be obtained from Knigge et al. (2011) as their orbital periods are too long. For these systems, the secondary temperature was inferred from the spectral type using the Harvard Spectral Classification Scheme created by Annie Jump Cannon. The radii were calculated from the masses using the mass-radius relation for CV donor stars determined by Knigge (2006):

$$R_2 = 0.2361 \; P_{orb}^{\frac{2}{3}} \; M_2^{\frac{1}{3}} \tag{22}$$

where R_2 and M_2 are in solar units and P_{orb} is in units of hours.

4.4.3 Accretion Disc Spectra

I subtract the spectra of the primary and secondary from the spectral data of the systems. For each data point, I subtract the flux density of the stars (calculated in Sections 4.4.1 and 4.4.2) at the same frequency as the data point from the flux density of the data point. What remains (in the infrared - ultraviolet region) is spectral data for the accretion disc.

The inner radius of the disc is set as the approximate radius of an average white dwarf, 7000 km (Hewitt, 2020). The outer radius of the disc is defined as $0.7R_{L1}$,

where R_{L1} is the Roche lobe radius of the primary, which is calculated by equation 23 (Silber, 1992).

$$\frac{R_{L1}}{a} = (1.0015 + q^{0.4056})^{-1} \tag{23}$$

where:
R_{L1} is the Roche lobe radius of the primary
a is the orbital separation
$q = \frac{M_2}{M_1}$

By Kepler's third law, the orbital separation of the binary is related to the orbital period by (Reese, 1999, ch.10):

$$GM = \omega^2 a^3$$

where:
G is the gravitational constant
M is the total mass of the system $= M_1 + M_2$
ω is the orbital frequency $= 2\pi/P_{orb}$
P_{orb} is the orbital period

Therefore R_{out} is given by equation 24.

$$R_{out} = \frac{0.7(\frac{G(M_1+M_2)}{\omega^2})^{\frac{1}{3}}}{1.0015 + (\frac{M_2}{M_1})^{0.4056}} \tag{24}$$

The function *blackbody(freq_ array,accretion_ mass, primary_ mass, inclination, distance)* takes in an array of ν-values for the data, as well as the input parameters (see Section 4.4.4). It calculates the blackbody spectrum for a range of ten thousand temperatures, calculated using equations 9 and 10, the corresponding radii for which are evenly spread between R_{in} and R_{out}, and performs a Riemann sum over the radii of the rings to determine the spectrum for an accretion disc with the given parameters over the given frequency domain, using equation 12. The *blackbody()* function returns an array of the corresponding flux densities for each frequency in the given input array.

4.4.4 Parameter Inputs

The *blackbody()* function takes, as inputs, an estimate for the accretion rate in solar masses per year, the mass of the primary in solar masses, the inclination of the

system in degrees and the distance to the binary in parsecs. These parameters for each CV are given in table 3. When the accretion rate for a given system is not known, a default value of $1 \times 10^{-9} M_{\odot}.yr^{-1}$ is used, as the CVs in this study tend have accretion rates on the order of nanosolar masses per year. Distances are retrieved from *GAIA*'s *external.gaiadr2_ geometric_ distance* table (Bailer-Jones et al., 2018).

A curve-fitting algorithm (see Section 4.4.5) is run on the *blackbody()* function that finds the best fit for the data. The values for primary mass, inclination and distance are constants in the fitting algorithm, and the mass accretion rate is given as a starting point. The fitting algorithm adjusts this parameter to find the best fit for the data.

In figure 31 I show how adjusting each of the input parameters effects the shape of the outputted accretion disc spectrum. In particular, figure 31a is a visual representation of how the adjustments made to the mass accretion rate by the curve fitting algorithm in the next section effect the spectrum.

From equations 10 and 9; a high primary mass implies a high viscous dissipation rate, which implies high disc temperature and therefore a brighter disc. This is reflected in the plots in figure 31b.

In figure 31c one can see how inclination affects the spectrum. In low-inclination systems, in which the normal of the plane of the disc is close to parallel to the line of sight, the plane of the disc faces the observer and the system therefore appears bright. A 90° inclination angle, in which the normal of the plane of the disc is orthogonal to the line of sight, results in a very dim disc.

Systems far away from the observer will have a smaller solid angle in the sky, and so will have lower apparent brightness, as can be seen in figure 31d.

4.4.5 Curve Fitting

Python's *scipy.optimize.curve_fit()* algorithm is used to calculate the best fitting accretion disc spectrum for the data. It takes in the *blackbody()* function, the y- and x-values for the data, and the input parameters that the *blackbody()* function takes. It performs a curve fit by adjusting the mass accretion rate to determine the best fitting curve. It returns the best-fit estimate for the accretion rate. This fitted parameter is then used, with the *blackbody()* function, to plot the best-fit accretion disc spectrum curve for the data. The errors of the individual data points are used, in Section 4.4.7, to determine the goodness of fit of the best-fit curve.

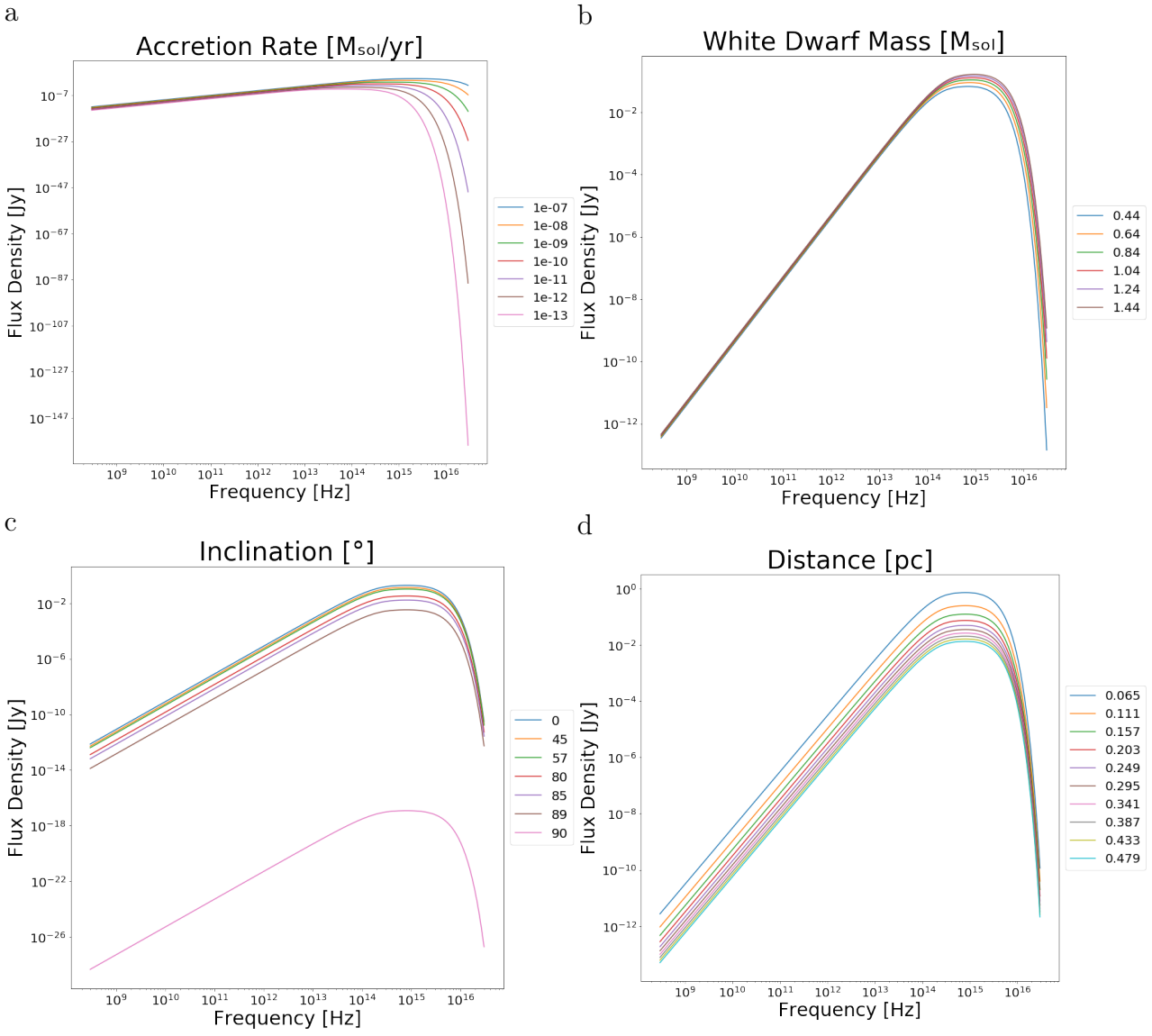

Figure 31: How each of the input parameters to the *blackbody()* function affect the output. In each case, the other input values were held at a set value, and the input in question was varied over a range of values representative of the range of system parameters in the observed systems.

4.4.6 Uncertainties

In addition to the fitted parameters for the system, the *scipy.optimize.curve_fit()* algorithm outputs a covariance matrix, the diagonal of which contains the variances of the fitted parameters. Because the *blackbody()* function is only being fitted on one input variable, it is a 1×1 matrix, and this value is the variance of the accretion rate. The standard deviation is the square root of the variance, and so the square root of this value is taken as the error in the accretion rate.

4.4.7 Goodness of Fit

In order to determine the goodness of fit of the fitted accretion disc spectra, as well as the meaningfulness of my estimated accretion rates and uncertainties, I calculated the reduced χ^2 values of the fits. In order to do this, I calculate (Bevington & Robinson, 2003; Andrae et al., 2010):

$$\chi^2 = \sum_{n=1}^{N} \left(\frac{y_n - f(x_n, p)}{\sigma_n} \right)^2 \tag{25}$$

where:
N is the number of data points
y_n are the y-values of the data points
x_n are the x-values of the data points
$f(x_n, p)$ are the y-values for the fitting function for each value of x_n
p are the input parameters of the function
σ_n are the errors of the data points

I then calculate the reduced χ^2 value (Bevington & Robinson, 2003; Andrae et al., 2010):

$$\chi^2_{red} = \frac{\chi^2}{K} \tag{26}$$

where K is the number of degrees of freedom, in this case K = 1, as there is only one adjustable input parameter, accretion rate.

If $\chi^2_{red} \approx 1$ it is a good fit. If $\chi^2_{red} \gg 1$ it is considered an underfit, whereas $\chi^2_{red} \ll 1$ is considered an overfit (Andrae et al., 2010).

4.4.8 Flux Density Ratios

In order to compare the flux densities in different wavebands, one dataset of those plotted in Section 6.1.2 is selected from each waveband.

For each waveband, the selected dataset is present in most of the systems in my sample, generally does not contain significant outliers, is relatively consistent across the systems, and tends to fall on the accretion disc spectrum (for the IR - UV wavebands).

The selected data sets are the radio data provided by Deanne L. Coppejans[3], 2MASS data in the K-band (infrared), *GAIA* data in the G-band (visible), *IUE* data for the ultraviolet waveband and spectral *XMM* data for the X-ray. Due to the gap in available data in the microwave, this waveband was not included in this analysis. Where a particular dataset was not available for a given system, that system is excluded from the relevant flux density ratio plots.

For each waveband, an average of the flux density is calculated, and these averages are then used to calculate and plot the flux density ratios between each of the wavebands, which are then plotted against orbital period for each system. These plots are shown in Section 6.1.4 in figures 56 - 59.

5 A Sample of Well-Studied CVs

In this section I introduce the observed systems and tabulate their relevant properties. I present a brief overview of each system, together with references for the listed parameters.

I selected nearby, well-studied CVs of the types nova-like, dwarf nova, intermediate polar and polar. My goal was to select a small sample of well-studied cataclysmic binary systems that span the different classes of CVs, in order to perform detailed analysis and establish the feasibility of my curve-fitting and accretion rate estimating method. As such four CVs of each type were selected. These 16 systems have some of the most complete multi-wavelength datasets, have been observed by many telescopes, and have well-estimated properties, in particular, well-constrained orbital periods. They would therefore provide the most robust results. Because large, broad-spectrum datasets were needed for each system, compiled from multiple data sources, these data may be biased towards nearer objects, where the fluxes would be higher, or towards well-known sources that are well-studied. These systems, and their relevant properties, are listed in Table 3. For reference, absolute magnitudes in the g-band for each system are also reported in Table 3. Apparent magnitudes retrieved from ASAS-SN were used to calculate absolute g-magnitudes using equation 27.

$$M_g = -5 \times log_{10}(d[\mathrm{pc}]) + 5 + m_g \tag{27}$$

5.1 Nova-Likes

5.1.1 V603 Aql

V603 Aquilae is a nova-like cataclysmic binary system in the constellation Aquila (Mukai et al., 2002). It was one of the brightest stars observed in the 20^{th} century, rising to 1 mag at its peak (Arenas et al., 2000). The system is 311 parsecs[47] away, with an orbital period that was found by to be $P_{orb} = 0.1385 \pm 0.0002$ days (Arenas et al., 2000; Bailer-Jones et al., 2018). Arenas et al. (2000) also deduced stellar masses of $M_1 = 1.2 \pm 0.2$ $\mathrm{M}_\odot$ and $M_2 = 0.29 \pm 0.04$ $\mathrm{M}_\odot$, and an orbital inclination of $i = 13^\circ \pm 2^\circ$.

V603 Aql was first observed in June 1918, and was the brightest nova discovered since the invention of the telescope (Drechel et al., 1981; Haefner & Metz, 1984). Due to an apparent overabundance of Ne, V603 Aql is consistent with a young stellar system, and from infrared interferometry measurements the spectral type of the secondary is believed by Feast & Glass (1974) to be a middle K dwarf (Mukai &

Table 3: The CVs selected for detailed study, and their relevant properties from the literature and absolute g-magnitudes from ASAS-SN.

Type	Name	P_{orb} [hrs]	d [pc]	i [°]	M_1 [$M_\odot$]	M_2 [$M_\odot$]	T_1 [K]	T_2 [K]	R_2 [$R_\odot$]	M_g
NL	V603 Aql	3.324	311	13	1.2	0.29	102 500	3326	0.327	4.40
NL	V3885 Sgr	4.972	132	65	0.7	0.473	57 000	3660	0.534	4.69
NL	IX Vel	4.654	90.3	57	0.8	0.52	60 000	3576	0.486	4.73
NL	UX UMa	4.700	295	71	0.78	0.47	20 000	3587	0.492	5.54
DN	SU UMa	1.832	219	44	0.7	0.15	28 000	3091	0.167	7.74
DN	U Gem	4.246	93.1	72	1.1	0.6	29 500	3487	0.426	9.56
DN	Z Cam	6.955	224	57	0.99	0.729	57 000			5.09
DN	SS Cyg	6.603	114	36	0.81	0.55	50 000			5.68
IP	DQ Her	4.647	494	86.5	0.6	0.4	80 000	3574	0.484	6.23
IP	DO Dra	3.969	197	45	0.83	0.375	215 00	3434	0.389	8.95
IP	AE Aqr	9.880	91.0	0.63	0.37					6.97
IP	EX Hya	1.637	56.9	76.8	0.79	0.108	25 000	2912	0.149	9.63
Polar	AM Her	3.094	87.5	50	0.78		19 800	3300	0.289	9.38
Polar	AR UMa	1.932	101	65			15 000	3177	0.190	11.25
Polar	BL Hyi	1.894	130	47.5	0.45			3147	0.184	10.73
Polar	VV Pup	1.673	136	75	0.73	0.1	11 900	2950	0.154	9.72

Orio, 2005). Hence, for the purpose of this study, the spectral type of the secondary is assumed to be K5V.

Pottasch (1959) determined the temperature of the white dwarf to vary between $T_1 = 60\ 000\ K$ and $T_1 = 145\ 000\ K$. In this paper I estimate a white dwarf temperature of $T_1 = 102\ 500\ K$. From Knigge (2006), the donor temperature is $T_2 = 3326$ K and the donor radius is $R_2 = 0.327\ R_\odot$.

5.1.2 V3885 Sgr

Discovered in 1968, V3885 Sagittarii is non-eclipsing ($i = 65 \pm 2°$) nova-like variable with an orbital period of $P_{orb} = 0.2071607$ days, and is one of the brightest CVs (Cowley et al., 1977; Bond, 1978; Riberto & Diaz, 2007; Linnell et al., 2009).

V3885 Sgr is 132 parsecs[47] away (Bailer-Jones et al., 2018). Linnell et al. (2009) reports the system's accretion rate, $\dot{M} = 5.0 \pm 2.0 \times 10^{-9}\ M\ yr^{-1}$, the masses of the white dwarf, $M_1 = 0.70 \pm 0.1\ M_\odot$, and the secondary, $M_2 = 0.475\ M_\odot$, and the temperature of the white dwarf, $T_1 = 57\ 000\ \pm\ 5\ 000$ K. Given an orbital period of 4.972 hr, and using Knigge et al. (2011), I estimate that V3885 Sgr has spectral type of M2.4V. From Knigge (2006), the donor temperature is $T_2 = 3660$ K and the

donor radius is $R_2 = 0.534$ R$_\odot$.

5.1.3 IX Vel

IX Velorum was discovered and identified as a nova-like cataclysmic variable by Garrison et al. (1982, 1984), and is the brightest such object in the sky (Kubiak et al., 1999; Linnell et al., 2007). However, Kato (2021) recently postulated that it is in fact a Z Cam-type dwarf nova. IX Vel flickers on the order of ~ 25 s at an amplitude of 0.0010 mag (Warner et al., 1985).

The distance to IX Vel is $d = 90.3$ pc[47] (Bailer-Jones et al., 2018). Linnell et al. (2007) derived the parameters primary mass, $M_1 = 0.80 \pm 0.2$ M$_\odot$, secondary mass, $M_2 = 0.52 \pm 0.10$ M$_\odot$, mass accretion rate $\dot{M} = 5.0 \pm 1.0 \times 10^{-9}$ M$_\odot$ yr^{-1}, orbital period, $P_{orb} = 0.1939292$ days, orbital inclination, $i = 57 \pm 2°$, and white dwarf temperature, $T_1 = 60\,000 \pm 10\,000$ K. Beuermann (2000) reports the spectral type of the secondary as M2. From Knigge (2006), the donor temperature is $T_2 = 3576$ K and the donor radius is $R_2 = 0.486$ R$_\odot$.

5.1.4 UX UMa

UX Ursa Majoris is one of the earliest-recognized and most well-studied CVs (de Miguel et al., 2016). It is an eclipsing binary with ~ 30 second oscillations in brightness and is 295 parsecs away[47] (de Miguel et al., 2016; Bailer-Jones et al., 2018). Baptista et al. (1995) calculated system parameters for the inclination, $i = 71.0° \pm 0.6°$, and mass accretion rate, $\dot{M} = 10^{-8.0\pm0.2}$ M$_\odot$ yr^{-1}. Vande Putte et al. (2003) estimated the mass of the primary, $M_1 = 0.78 \pm 0.13$ $M_\odot$, the mass of the secondary, $M_2 = 0.47 \pm 0.07$ $M_\odot$, and the orbital period, $P_{orb} = 4.7$ h. The temperature of the primary is $T_1 = 20\,000$ K (Linnell et al., 2008), and, from Knigge (2006), the donor temperature is $T_2 = 3587$ K and the donor radius is $R_2 = 0.492$ R$_\odot$.

5.2 Dwarf Novae

5.2.1 SU UMa

SU Ursa Majoris is the prototype of the SU UMa subclass of dwarf novae (see Section 2.7.1. Thorstensen et al. (1986) found the orbital period of SU UMa to be $P_{orb} = 0.076351 \pm 4.3 \times 10^{-5}$ days (110 minutes), as well as the masses of the primary, $M_1 = 0.7$ M$_\odot$, secondary, $M_2 \approx 0.15$ M$_\odot$, and the inclination, $i = 44° \pm 8°$. The distance to SU UMa is $d = 219$ pc[47] (Bailer-Jones et al., 2018), and Zead et al. (2017) found a mass accretion rate of $\dot{M} = 9.8 \times 10^{-13}$ M$_\odot$ yr^{-1} during outburst. Urban & Sion (2006) estimates a white dwarf temperature of $T_1 = 28\,000$ K. I again use Knigge et al. (2011) to estimate the spectral type of the secondary, M5.1V.

From Knigge (2006), the donor temperature is $T_2 = 3091$ K and the donor radius is $R_2 = 0.167$ R$_\odot$.

5.2.2 U Gem

First observed by English astronomer John Hind in December of 1855, U Geminorum is the prototype of the dwarf nova subclass of cataclysmic variables (Smith, 2007, ch.4; Toone, 2012). The distance to U Gem is $d = 93.1$ pc[47] (Bailer-Jones et al., 2018), with an inclination of $i \approx 72°$ (Unda-Sanzana et al., 2006), and an orbital period of $P_{orb} = 0.176906$ day (Bailey, 1981). Smak (1976) found the mass of the components to be $M_1 = 1.1 \pm 0.4$ M$_\odot$ and $M_2 = 0.6 \pm 0.4$ M$_\odot$, and Dai & Qian (2009a) estimated a mass accretion rate of $\dot{M} = 3.5(5) \times 10^{-9}$ to $1.30(6) \times 10^{-8}$ M$_\odot$ yr^{-1}. Long et al. (2006) estimates a white dwarf temperature of $T_1 = 28\,000 - 31\,000$ K, and Knigge (2006) reports the spectral type of the secondary as M4.25 ± 0.5. From Knigge (2006), the donor temperature is $T_2 = 3487$ K and the donor radius is $R_2 = 0.426$ R$_\odot$.

5.2.3 Z Cam

Z Cam is the prototype of the Z Cam subclass of Dwarf novae. It experiences outbursts about once a month (Knigge et al., 1997; Mattei et al., 1996). It has the brightest outbursts in its class, and is the most well-studied (Hartley et al., 2005).

Z Cam is 224 parsecs[47] away and has an orbital period of $P_{orb} = 0.2898406(2)$ days, which places it above the period gap (Shafter, 1983; Thorstensen, 2003; Hartley et al., 2005; Bailer-Jones et al., 2018). It has a metal rich primary of temperature $T_1 = 57\,000$ K and mass of $M_1 = 0.99 \pm 0.15$M$_\odot$ (Shafter, 1983; Hartley et al., 2005). Hartley et al. (2005) also reports an inclination of $i = 57° \pm 11°$ (Shafter, 1983), mass accretion rate of $\dot{M} \sim 10^{18}$ g s^{-1} $= 1.59 \times 10^{-8}$ M$_\odot$ yr^{-1}, and a mass ratio of 0.71 ± 0.10 (Shafter, 1983), placing the mass of the secondary at about $M_2 = 0.729$ M$_\odot$ (Knigge et al., 1997; Hartley et al., 2005). Knigge (2006) reports the spectral type of the secondary as K7 ± 2.

5.2.4 SS Cyg

Discovered in 1869, the prototypical dwarf nova, SS Cygni was the first CV to be identified as a binary, by Joy (1956) (Stover et al., 1980; Miller-Jones et al., 2013). It is the brightest of the dwarf novae, and as such is one of the most well-studied CVs (Stover et al., 1980; Hessman, 1984; Smith, 2007, ch.4). It is non-eclipsing, with an inclination of $i = 36°$, and it undergoes outbursts approximately every 49 ± 15 days (Hessman, 1984; Miller-Jones et al., 2013)

Stover et al. (1980) reports an orbital period of $P_{orb} = 0.275129$ days, and it is 114 parsecs[47] away (Bailer-Jones et al., 2018). Bitner et al. (2007) derived primary and secondary masses of $M_1 = 0.81 \pm 0.19$ $M_\odot$ and $M_2 = 0.55 \pm 0.13$ $M_\odot$ respectively. Sion et al. (2010) reports that the white dwarf has a temperature of $T_1 \approx 45\,000 - 55\,000$ K, and Knigge (2006) reports the spectral type of the secondary as K4.5 $\pm$ 0.5. Lesniak & Sion (2003) estimates an accretion rate of $\dot{M} = 5 \times 10^{-11} M_\odot$ yr^{-1}.

5.3 Intermediate Polars

5.3.1 DQ Her

The remnant of the nova Herculis 1934, DQ Herculis is an eclipsing binary system (Horne et al., 1993; Dai & Qian, 2009b), and is the prototype of the intermediate polar subclass of cataclysmic variables (Vaytet et al., 2007; Dai & Qian, 2009b). It was first observed at a magnitude of 3.3 on 12 December 1934 (Campbell, 1935; Vaytet et al., 2007; Dai & Qian, 2009b).

Horne et al. (1993) estimates the stellar masses of the white dwarf, $M_1 = 0.60 \pm 0.07$ $M_\odot$, and the companion, $M_2 = 0.40 \pm 0.05$ $M_\odot$. They also report an orbital period of $P_{orb} = 0.1936209$ days, and an inclination of $i = 86.5° \pm 1.6°$. *GAIA*[47] provides a distance to the system of $d = 494$ pc (Bailer-Jones et al., 2018), and Saito et al. (2010) estimates a mass accretion rate of $\dot{M} = (2.7 \pm 1.0) \times 10^{-9}$ $M_\odot$ yr^{-1}. Kraft (1959) estimated that the temperature of the white dwarf is $T_1 = 80\,000$ K, and Knigge (2006) reports the spectral type of the secondary as M3 $\pm$ 0.5. From Knigge (2006), the donor temperature is $T_2 = 3574$ K and the donor radius is $R_2 = 0.484$ $R_\odot$.

5.3.2 DO Dra

Also known in the literature as "YY Dra", DO Draconis is a cataclysmic variable of the subclass intermediate polar (Green et al., 1982; Patterson et al., 1982; Patterson, 1994; Andronov et al., 2008).

Haswell et al. (1997) determined an orbital period of $P_{orb} = 0.16537398[17]$ days, as well as the mass of the primary, $M_1 = 0.83 \pm 0.10$ $M_\odot$, the mass of the secondary, $M_2 = 0.375 \pm 0.014$ $M_\odot$, and the inclination, $i = 45° \pm 4°$. *GAIA*[47] provides a distance to the system of $d = 197$ pc (Bailer-Jones et al., 2018).

Hoard et al. (2005) determined a white dwarf temperature of $T_1 = 21\,500$ K, and Knigge (2006) reports the spectral type of the secondary as M4.25 $\pm$ 0.7. From Knigge (2006), the donor temperature is $T_2 = 3434$ K and the donor radius is $R_2 = 0.389$ $R_\odot$.

5.3.3 AE Aqr

AE Aquarii is a noneclipsing cataclysmic variable in the constellation Aquarius (Welsh et al., 1998). It is observed at an apparent magnitude of about 11 to 12, making it one of the brightest CVs, and was discovered in the visible range by Zinner (1938) (Bruch, 1991; Echevarría et al., 2008). It was classified as a binary by Joy (1954) and as an intermediate polar by Patterson (1979). It has a long orbital period of $P_{orb} = 9.88$ hr (Walker, 1965), making it one of the largest cataclysmic variables (Welsh et al., 1998).

Echevarría et al. (2008) calculates the masses of the primary and secondary to be $M_1 = 0.63 \pm 0.05$ $M_\odot$ and $M_2 = 0.37 \pm 0.04$ $M_\odot$ respectively, and Watson et al. (2006) determined the inclination, $i = 66°$, with an upper limit of 70°. *GAIA*[47] provides a distance to the CV of $d = 91.0$ pc (Bailer-Jones et al., 2018), and reports Knigge (2006) a secondary spectral type of K4 ± 1.

AE Aqr is known to be an unusual CV specimen. In addition to being large and bright and having a long orbital period, it exhibits random flaring, and rapid oscillations that indicate an extremely fast spinning white dwarf (Welsh et al., 1998). The white dwarf spins so fast that its magnetosphere is modelled as a propeller, and until last year had the fastest-known white dwarf spin of $P_{spin1} = 33.08$ s (Kitaguchi et al., 2014; Mereghetti et al., 2021).

5.3.4 EX Hya

EX Hydrae is an eclipsing binary with a short orbital period of $P_{orb} = 98.26$ min, and is the prototype of the short-period intermediate polars (Kruszewski et al., 1982; Beuermann & Reinsch, 2008). Its orbital period is decreasing at a rate of $\dot{P}_{orb} = 5.2 \times 10^{-12}$, likely as a result of angular momentum exchange due to mass transfer (Vogt et al., 1980).

Beuermann & Reinsch (2008) determined a white-dwarf mass of $M_1 = 0.790 \pm 0.026$ $M_\odot$, and a secondary mass of $M_2 = 0.108 \pm 0.008$ $M_\odot$, and Beuermann et al. (2003) found an inclination of $i = 76.0° - 77.6°$ and a quiescent mass accretion rate of $\dot{M} = (6.2 \pm 1.5) \times 10^{-11}$ $M_\odot$ yr^{-1}. Eisenbart et al. (2002) estimated the spectral type of the secondary, M4 ± 1 and the temperature of the white dwarf, $T_1 = 25\ 000 \pm 3\ 000$. *GAIA*[47] provides a distance to the system of $d = 56.9$ pc (Bailer-Jones et al., 2018), making it one of the closest known CVs. From Knigge (2006), the donor temperature is $T_2 = 2912$ K and the donor radius is $R_2 = 0.149$ $R_\odot$.

5.4 Polars

5.4.1 AM Her

Discovered by Wolf (1924), AM Herculis is the prototype polar CV (Tapia, 1977a). It has an orbital period of $P_{orb} = 3.094$ hr, an orbital inclination of $i = 50°$, and is 87.5 parsecs[47] away (Campbell et al., 2008; Bailer-Jones et al., 2018; Pala et al., 2020). Gänsicke et al. (2006) found a white dwarf mass of $M_1 = 0.78 \pm^{0.12}_{0.17}$ $M_\odot$ and temperature of $T_1 = 19\ 800 \pm 700$ K, and Campbell et al. (2008) estimated its magnetic field to be $B_1 = 13.6 \pm^{1.0}_{0.8}$ MG. Knigge (2006) reports that the spectral type of the secondary is M4.25 ± 0.5. From Knigge (2006), the donor temperature is $T_2 = 3300$ K and the donor radius is $R_2 = 0.289$ $R_\odot$.

5.4.2 AR UMa

AR Ursae Majoris is a nearby ($d = 101$ pc[47]) cataclysmic variable with an extremely high magnetic field of $B \approx 230$ MG that places it in the polar subclass (Remillard et al., 1994; Schmidt et al., 1996; Gänsicke et al., 2001; Bailer-Jones et al., 2018; Pala et al., 2020). It has a short orbital period of $P_{orb} = 1.932$ hr that situates it at the lower edge of the period gap (Remillard et al., 1994; Gänsicke et al., 2001).

Heise & Verbunt (1988) derived an upper limit to the white dwarf temperature of $T_1 \approx 20\ 000$ K, and Knigge (2006) reports that the spectral type of the secondary is M5.5 ± 0.5. Harrison & Campbell (2015) estimates its inclination as $i = 65°$, and Gänsicke et al. (2001) places the accretion rate of the binary at $M_\odot \approx 1.7 \times 10^{-13}$ $M_\odot$ yr^{-1}. For the purposes of this study, the white dwarf is modelled as a 20 000 K blackbody. From Knigge (2006), the donor temperature is $T_2 = 3177$ K and the donor radius is $R_2 = 0.190$ $R_\odot$.

5.4.3 BL Hyi

BL Hydri was first observed by Agrawal et al. (1981), and was identified as a polar CV by Visvanathan & Pickles (1982) and Agrawal et al. (1983). Its orbital period was established as $P_{orb} = 113.65$ min by Agrawal et al. (1983), and Wolff et al. (1999) calculated the mass of the white dwarf to be $M_1 = 0.3 - 0.7 M_\odot$. The companion star has a spectral type of M5 (Kafka et al., 2010). From Knigge (2006), the donor temperature is $T_2 = 3147$ K and the donor radius is $R_2 = 0.184$ $R_\odot$.

GAIA[47] provides a distance to the system of 130 pc (Bailer-Jones et al., 2018). Estimates of the inclination range from $i = 25° \pm 15°$ to $i \approx 65°$ - 75° (Beuermann et al., 1985; Schwope & Beuermann, 1985; Piirola et al., 1987).

5.4.4 VV Pup

VV Puppis is a well-studied system that was identified as a polar CV by Tapia (1977b) due to its strong circular polarisation (Schneider & Young, 1980). It has an orbital period of $P_{orb} = 0.069747$ days (Bailey, 1981), a mass accretion rate of $\dot{M} = 9.4 \times 10^{-13}$ $M_\odot$ yr^{-1} (Pandel & Córdova, 2005; Howell et al., 2006), and is 137 parsecs[47] away (Bailer-Jones et al., 2018). Howell et al. (2006) produced estimates for several properties: $M_1 = 0.73 \pm 0.05$ $M_\odot$, $M_2 = 0.10 \pm 0.02$ $M_\odot$, and $i = 75° \pm 6°$. Mason et al. (2008) estimated a white dwarf temperature of $T_1 = 11\ 900\ K$, and Knigge (2006) reports that the spectral type of the secondary is M5.5 ± 0.5. From Knigge (2006), the donor temperature is $T_2 = 2950$ K and the donor radius is $R_2 = 0.154$ $R_\odot$.

6 Results and Discussion

In this section I present and discuss the results of my study of the systems in my sample, as well as systems from the Pala et al. (2020) volume-limited sample, for comparison.

6.1 The Sample for Detailed Study

6.1.1 Lightcurves

For reference, I show the lightcurves of the systems in my sample for the past three years, in figures 32 – 35. These data are obtained from ASAS-SN. EX Hya, V3885 Sgr, and UX UMa contained additional bright outliers, several magnitudes brighter than the known brightness ranges of these systems, that were removed. In these cases ASAS-SN was likely confused by a nearby object.

Most of the lightcurves contain regular seasonal gaps, the result of the system being occulted by or close to the Sun. The dwarf-novae outbursts in SU UMa and U Gem are clearly visible, as are low points in the lightcurves of UX UMa and DQ Her that are likely eclipses. AE Aqr is famous for its flaring behaviour, which is clearly displayed in its lightcurve. SS Cyg is well known for its frequent DN outbursts, and the very short outburst recurrence cycle is clear in this light curve. The lightcurve of Z Cam is very constant until quite recently. This is typical of Z Cam, and is the behaviour that characterises the Z Cam subclass of DNe. The system has been in a standstill, and has recently transitioned to a series of DN outbursts. The lightcurves of AM Her and VV Pup include significant low and high states, known as VY Scl behaviour, low and high states that look like inverted DN lightcurves. Some NLs and most polars display this behaviour. V603 Aql has been experiencing an increase in brightness over the past three years.

These light curves display the typical range of variability of the systems in this sample (excluding nova eruptions). The data making up the SEDs that are shown in these samples are from different epochs, and the resulting SEDs therefore are necessarily noisy, in particular in the case of the DNe.

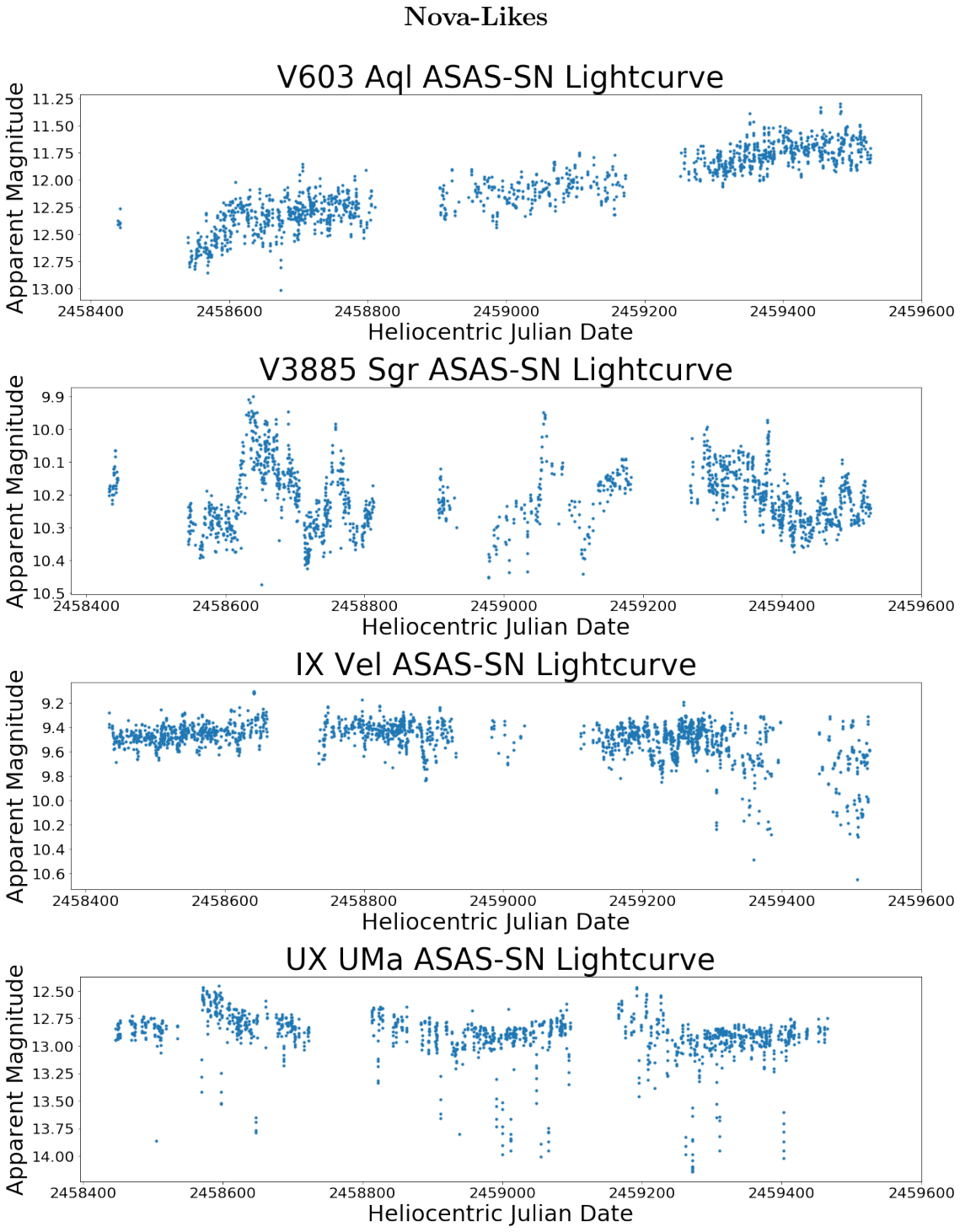

Figure 32: The lightcurves in the g-band of the nova-likes in my sample for the past 3 years, retrieved from ASAS-SN.

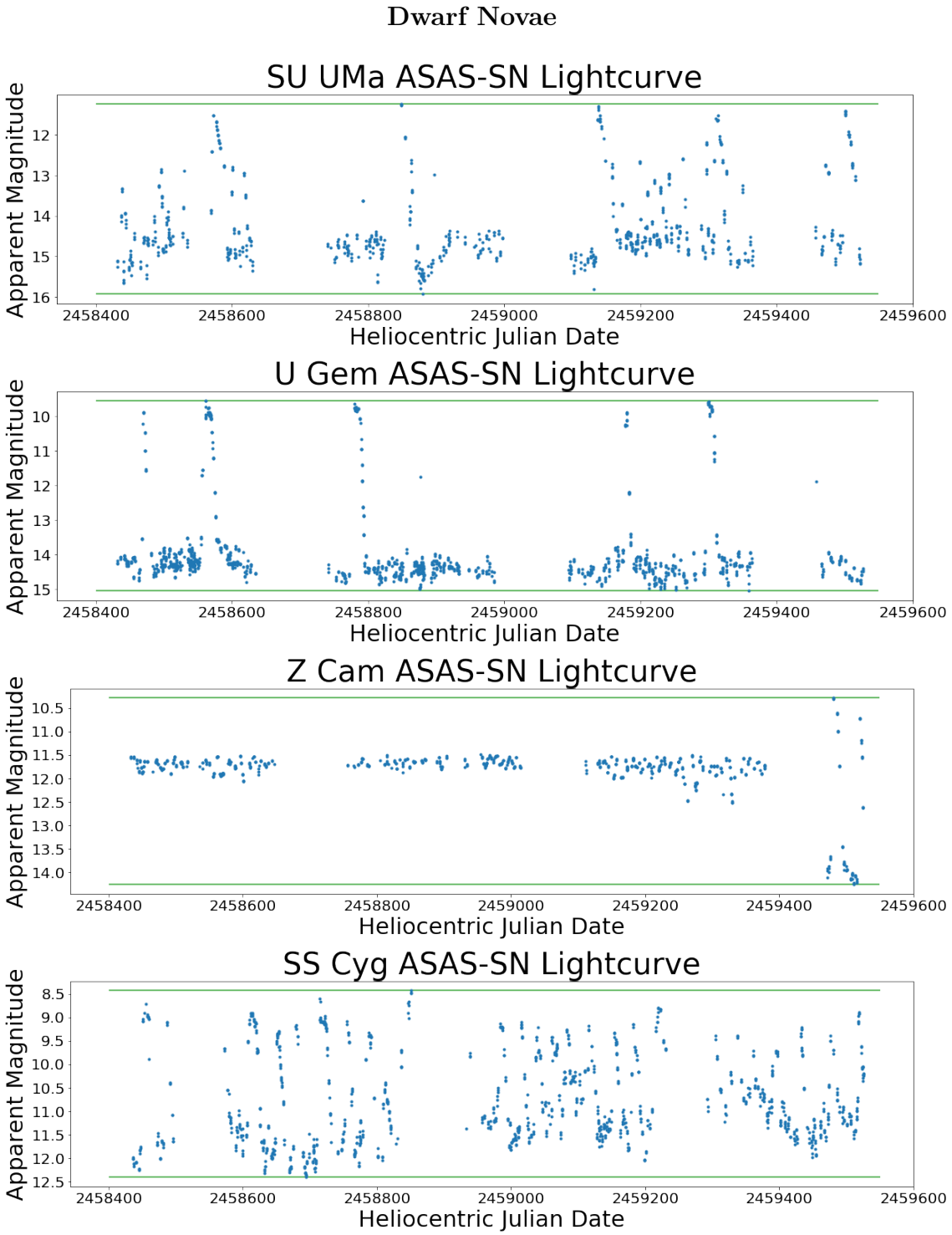

Figure 33: The lightcurves in the g-band of the dwarf novae in my sample for the past 3 years, retrieved from ASAS-SN. The green lines represent the maximum and minimum g-band magnitudes for the past three years. These are the same limits as in figure 54.

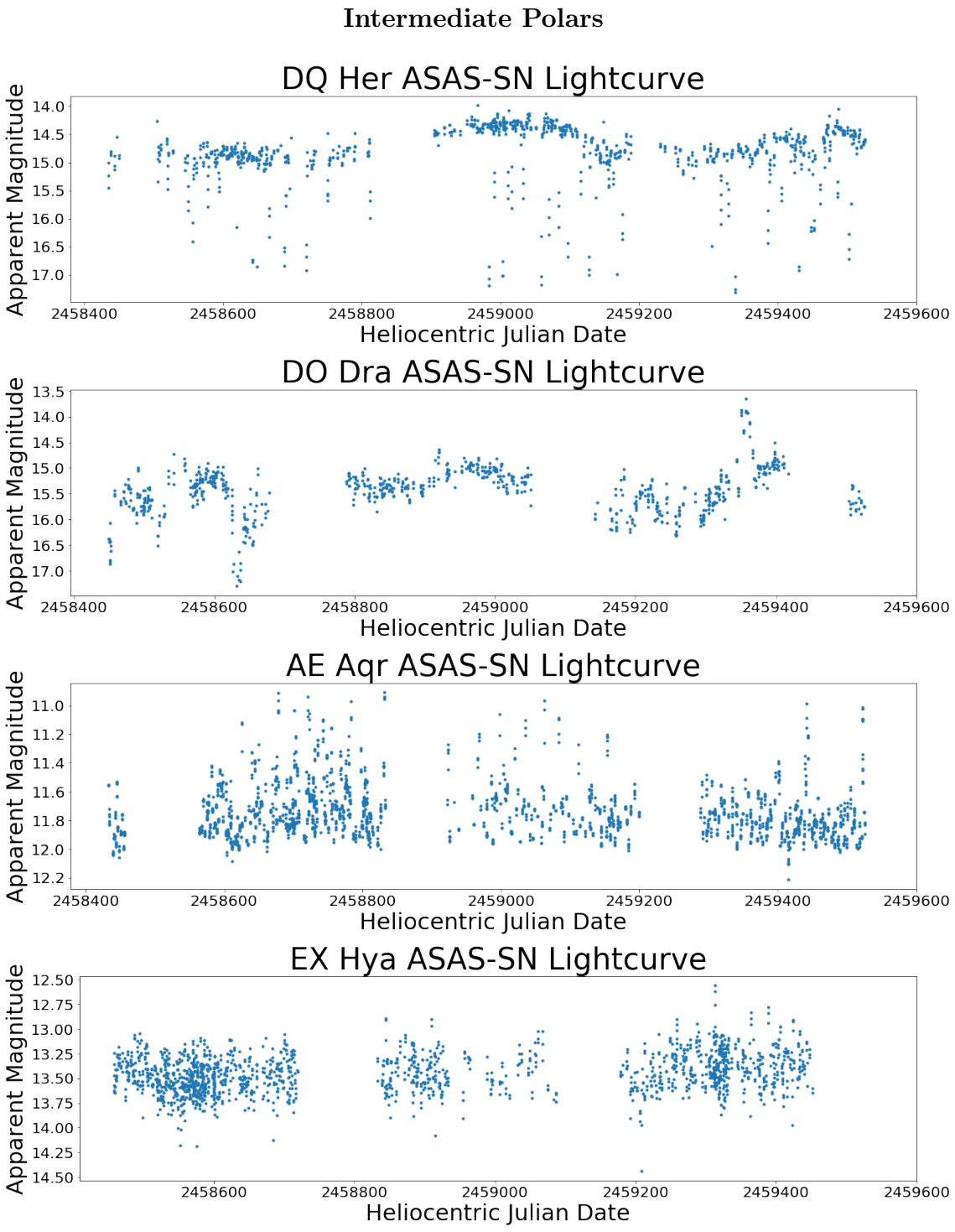

Figure 34: The lightcurves in the g-band of the intermediate polars in my sample for the past 3 years, retrieved from ASAS-SN.

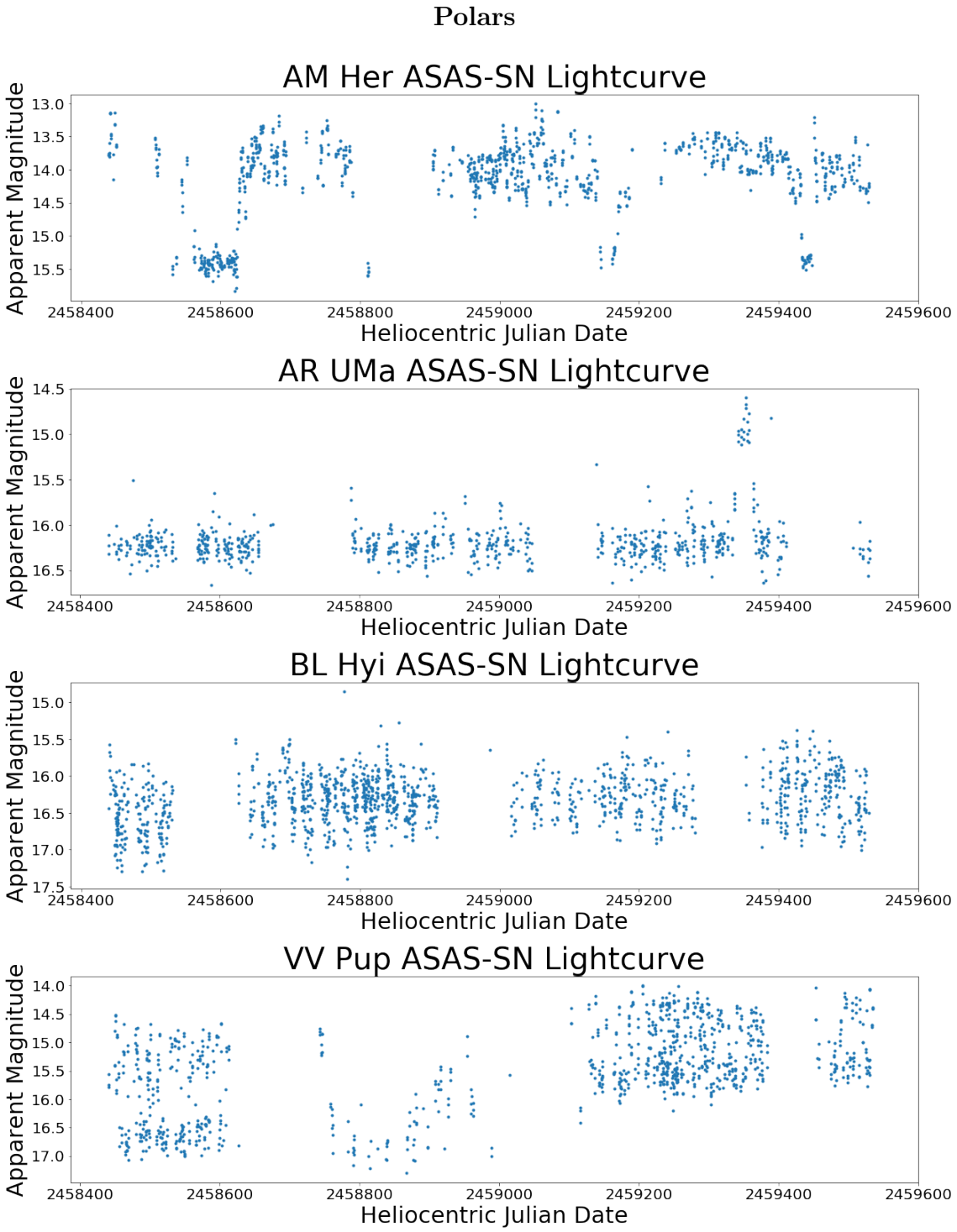

Figure 35: The lightcurves in the g-band of the polars in my sample for the past 3 years, retrieved from ASAS-SN.

6.1.2 Broad SEDs

On the following pages I have plotted the collected spectral energy data of these systems (figures 36 – 51). Overplotted, for the nova-likes and dwarf novae, are the spectra of the white dwarfs, the companions, the accretion discs, and the combined spectra of all components, the sum of the white dwarf, red dwarf and accretion disc contributions. For the mCVs, the spectra of the stellar components have been plotted, for those systems where the necessary properties were available, but no contribution from the accreting material has been plotted, as these systems do not have complete accretion discs.

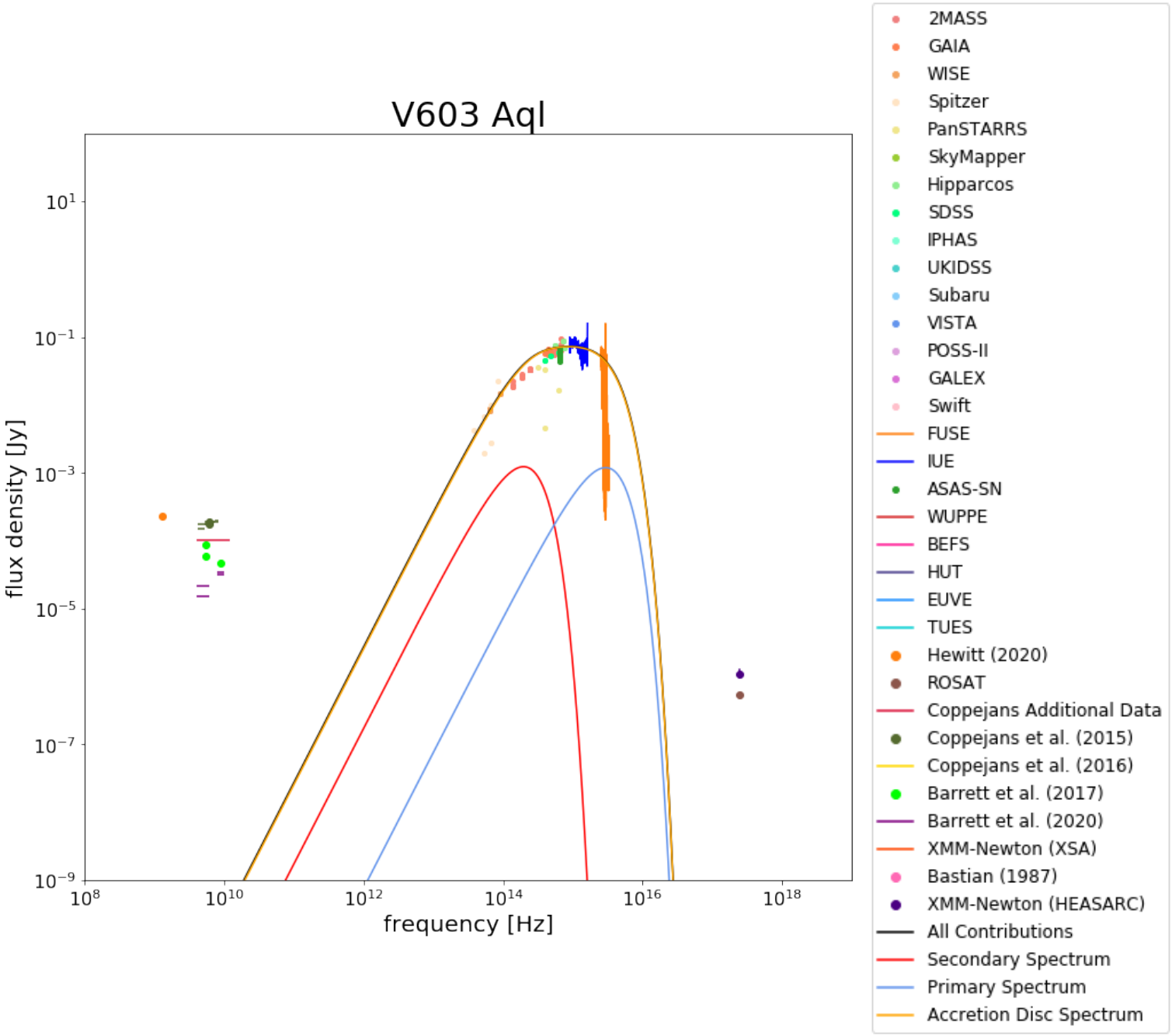

Figure 36: The broad SED of the nova-like V603 Aql. Overplotted are the contributions of the red dwarf (red), white dwarf (blue) and accretion disc (amber), as well as their combined contributions (black). The accretion disc spectra are fitted on data from *IRSA*, *ASAS-SN* and *IUE*. Different colours give the facility or survey from which data were obtained (see the legend to the right).

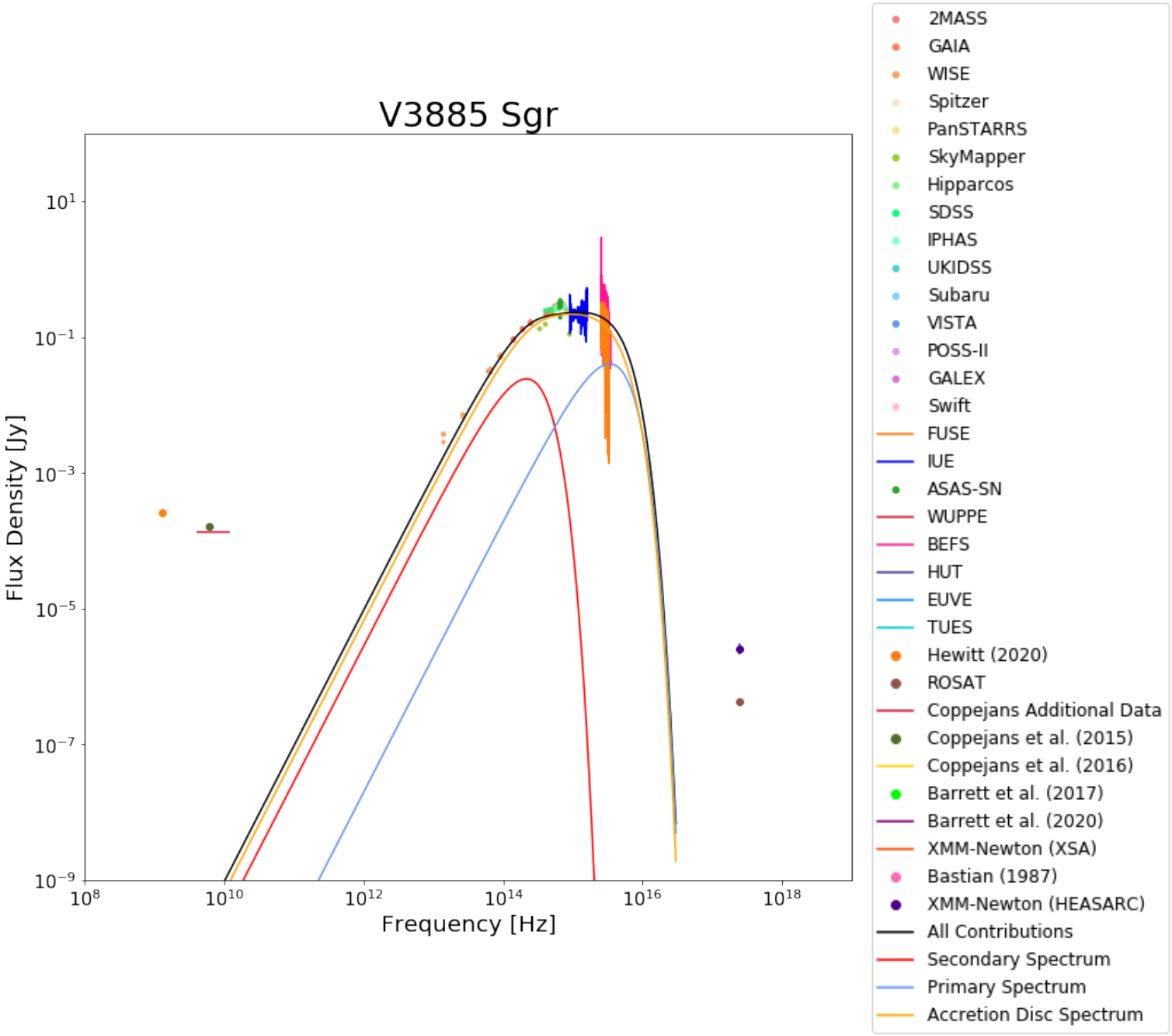

Figure 37: The broad SED of the nova-like V3885 Sgr. Overplotted are the contributions of the red dwarf (red), white dwarf (blue) and accretion disc (amber), as well as their combined contributions (black). The accretion disc spectra are fitted on data from *IRSA*, *ASAS-SN* and *IUE*. Different colours give the facility or survey from which data were obtained (see the legend to the right).

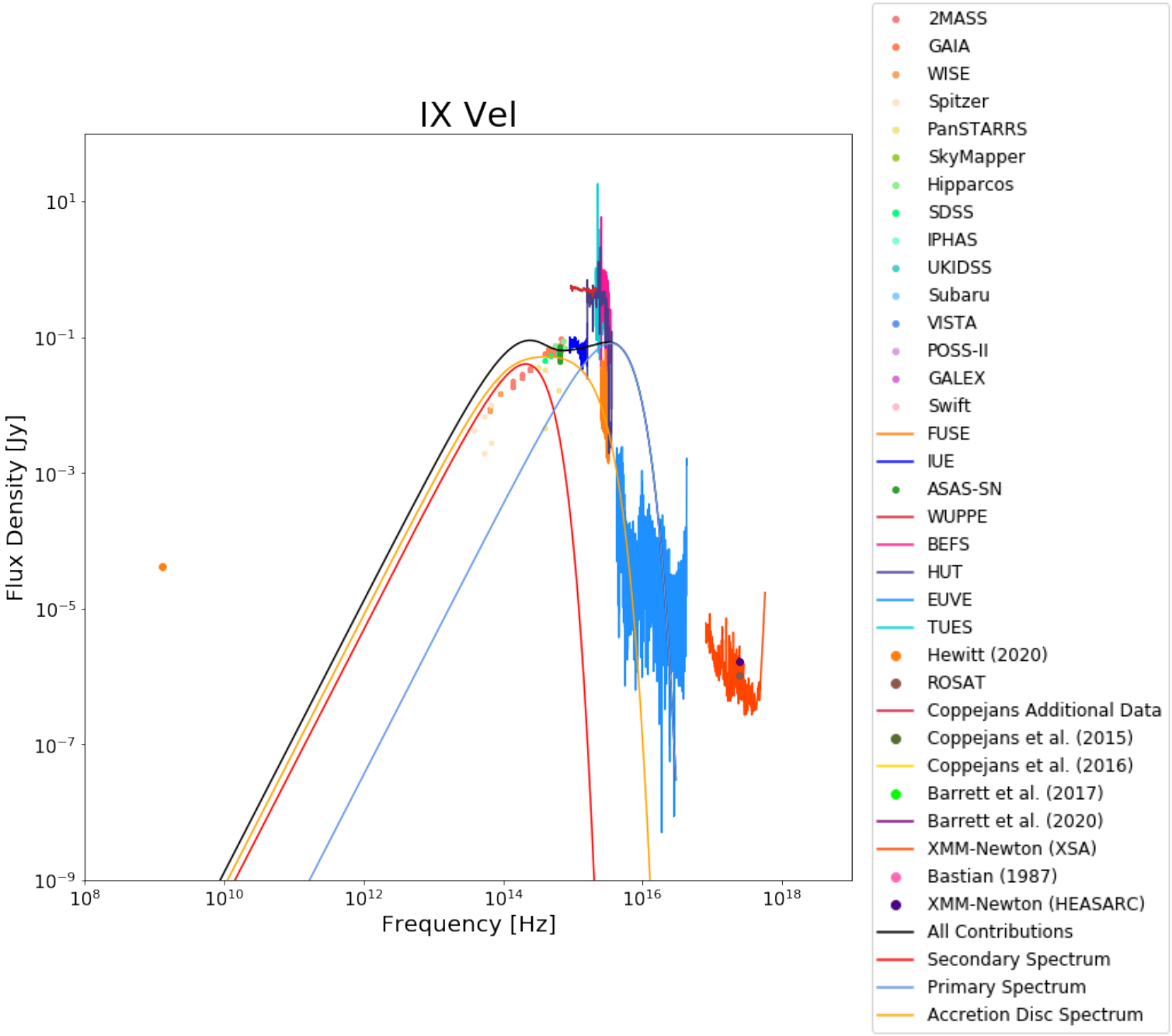

Figure 38: The broad SED of the nova-like IX Vel. Overplotted are the contributions of the red dwarf (red), white dwarf (blue) and accretion disc (amber), as well as their combined contributions (black).The accretion disc spectra are fitted on data from *IRSA*, *ASAS-SN* and *IUE*. Different colours give the facility or survey from which data were obtained (see the legend to the right).

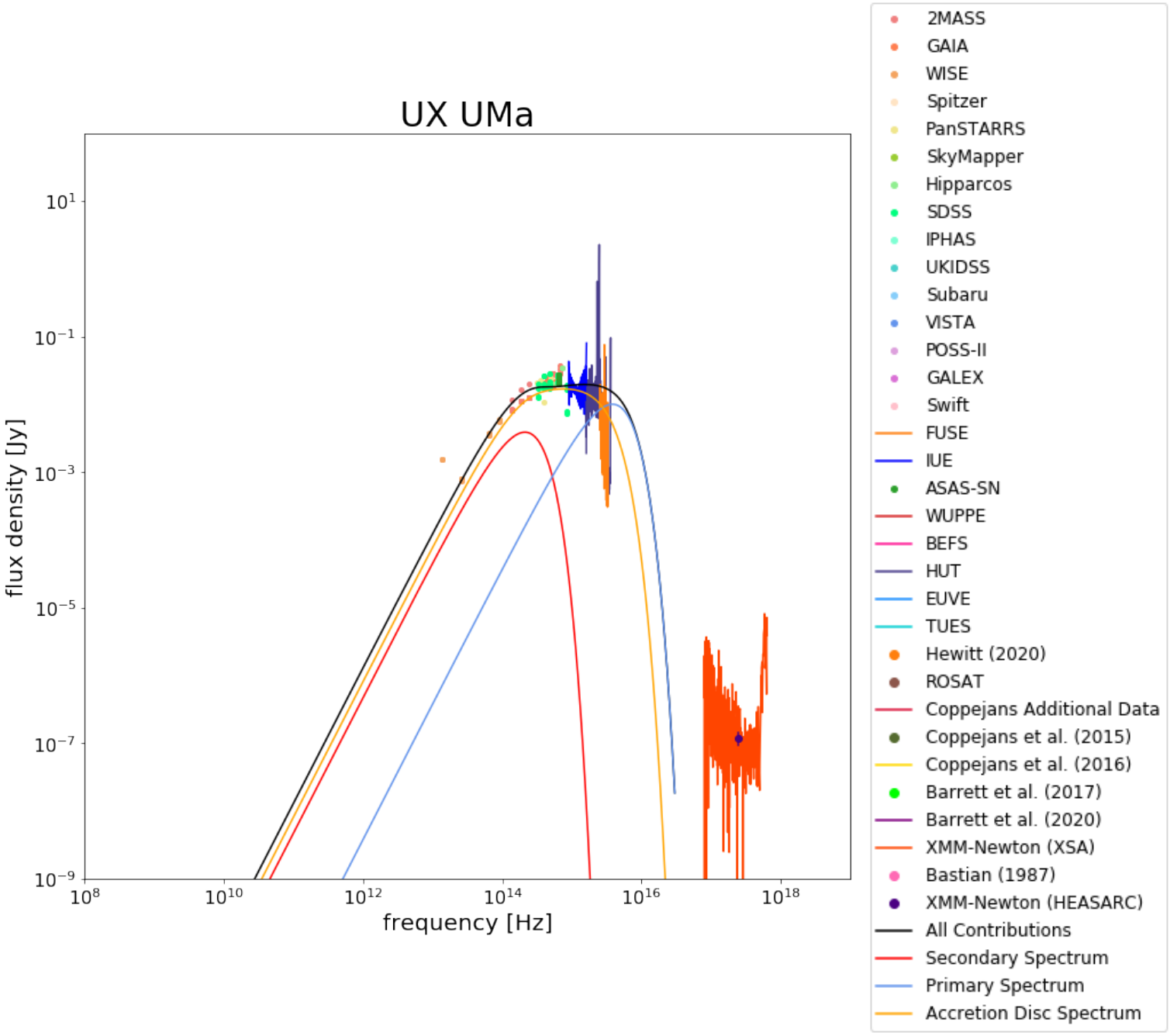

Figure 39: The broad SED of the nova-like UX UMa. Overplotted are the contributions of the red dwarf (red), white dwarf (blue) and accretion disc (amber), as well as their combined contributions (black). The accretion disc spectra are fitted on data from *IRSA*, *ASAS-SN* and *IUE*. Different colours give the facility or survey from which data were obtained (see the legend to the right).

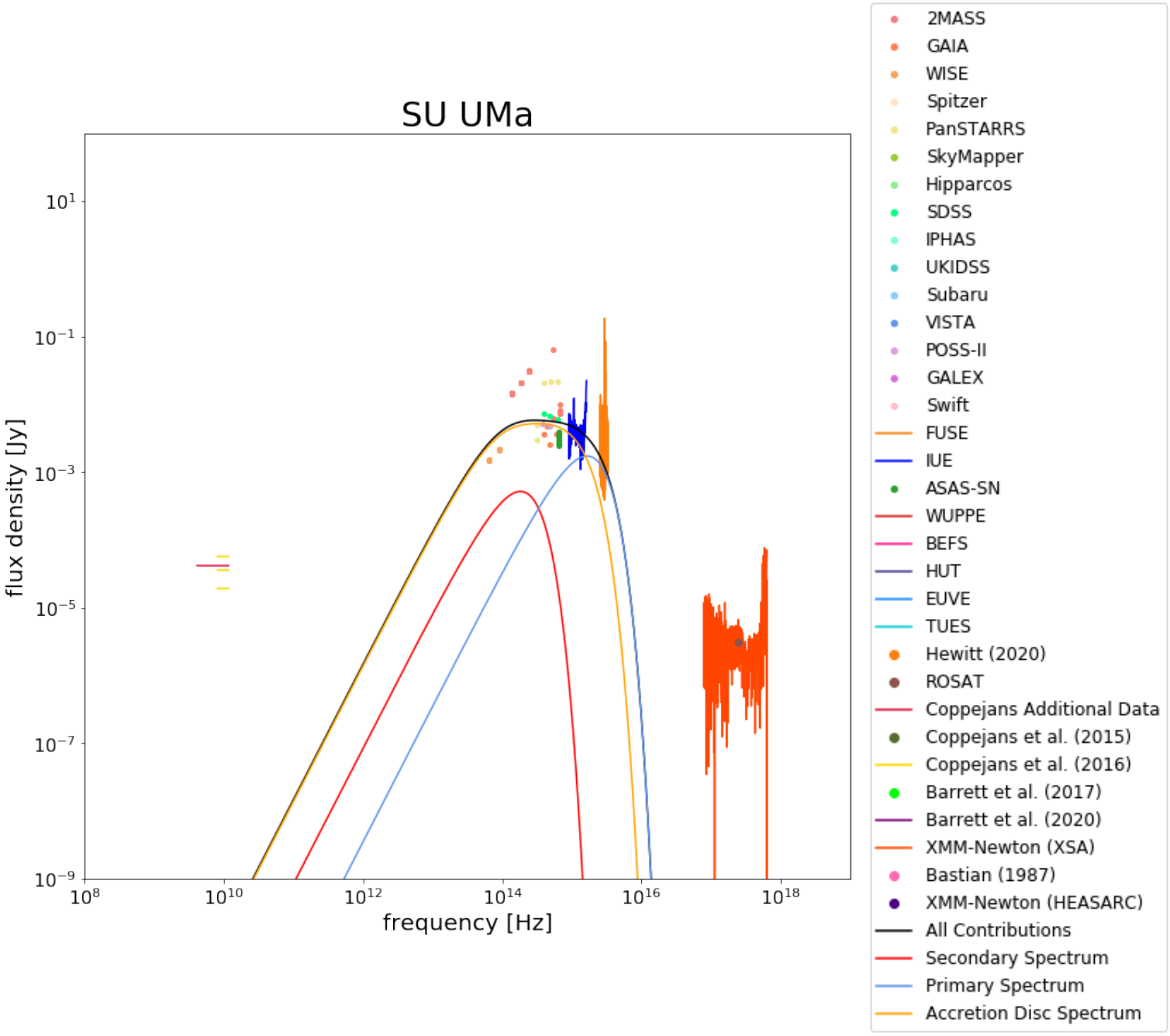

Figure 40: The broad SED of the dwarf nova SU UMa. Overplotted are the contributions of the red dwarf (red), white dwarf (blue) and accretion disc (amber), as well as their combined contributions (black). The accretion disc spectra are fitted on data from *IRSA*, *ASAS-SN* and *IUE*. Different colours give the facility or survey from which data were obtained (see the legend to the right).

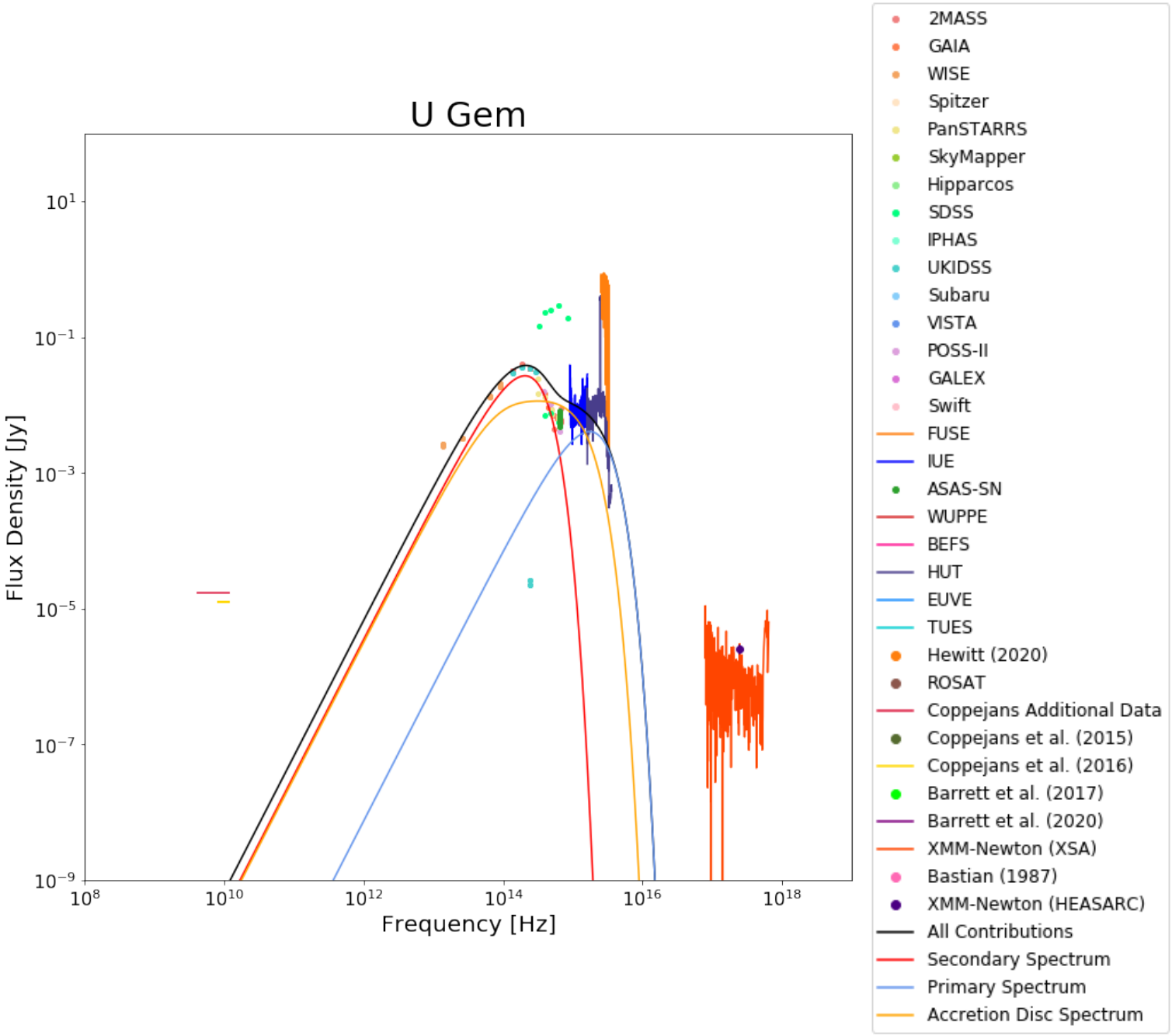

Figure 41: The broad SED of the dwarf nova U Gem. Overplotted are the contributions of the red dwarf (red), white dwarf (blue) and accretion disc (amber), as well as their combined contributions (black). The accretion disc spectra are fitted on data from *IRSA*, *ASAS-SN* and *IUE*. Different colours give the facility or survey from which data were obtained (see the legend to the right).

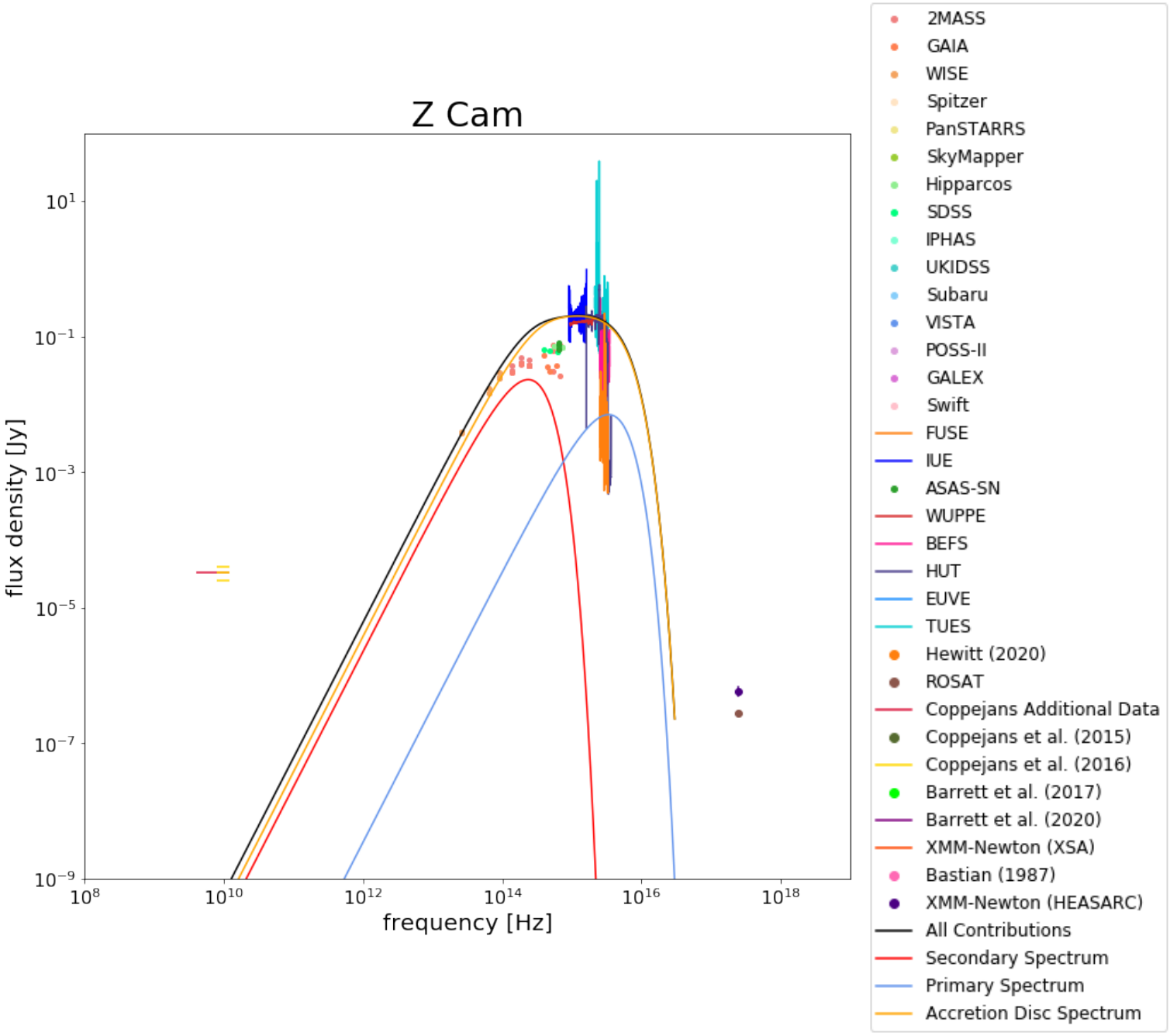

Figure 42: The broad SED of the dwarf nova Z Cam. Overplotted are the contributions of the red dwarf (red), white dwarf (blue) and accretion disc (amber), as well as their combined contributions (black). The accretion disc spectra are fitted on data from *IRSA*, *ASAS-SN* and *IUE*. Different colours give the facility or survey from which data were obtained (see the legend to the right).

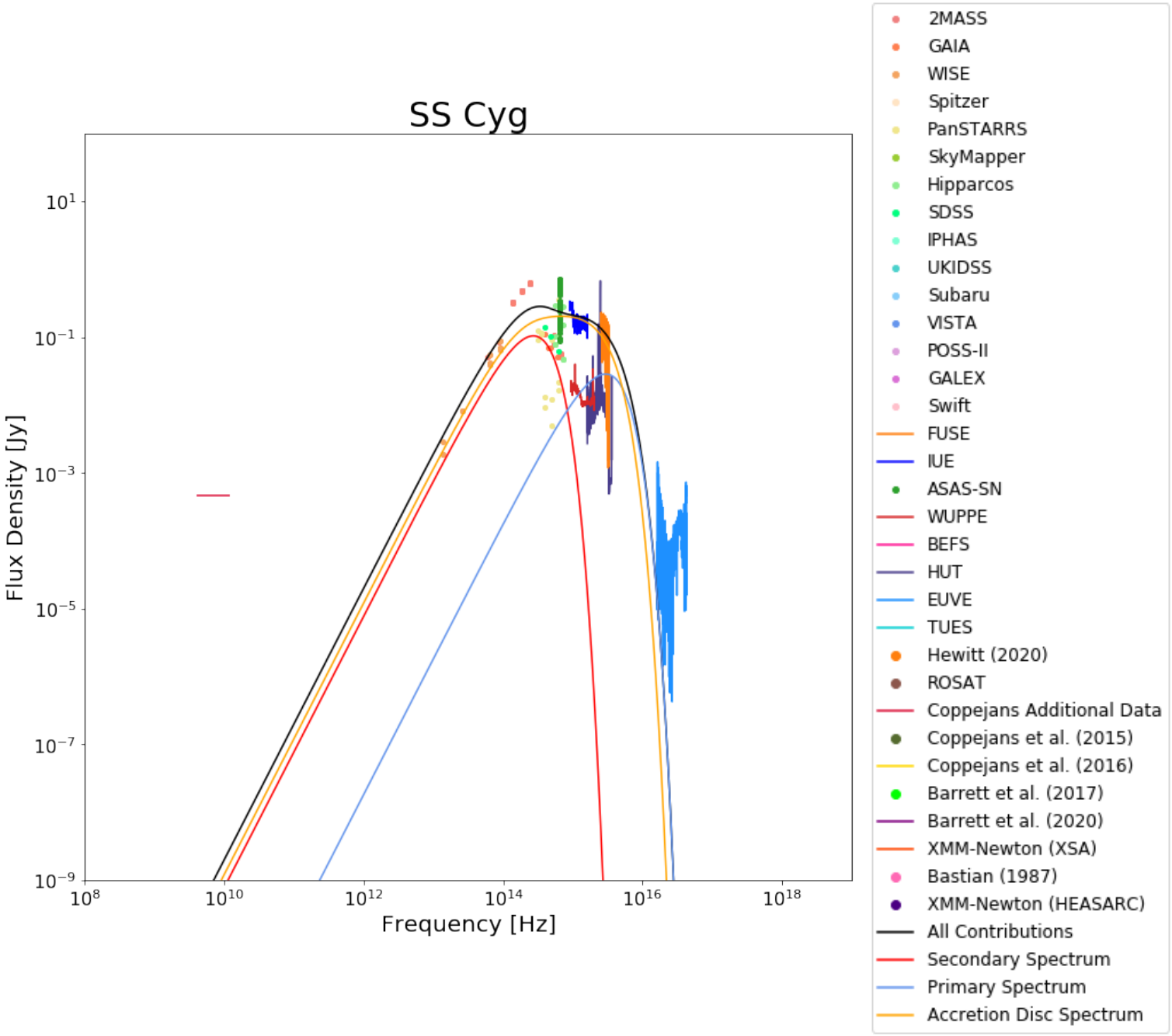

Figure 43: The broad SED of the dwarf nova SS Cyg. Overplotted are the contributions of the red dwarf (red), white dwarf (blue) and accretion disc (amber), as well as their combined contributions (black). The accretion disc spectra are fitted on data from *IRSA*, *ASAS-SN* and *IUE*. Different colours give the facility or survey from which data were obtained (see the legend to the right).

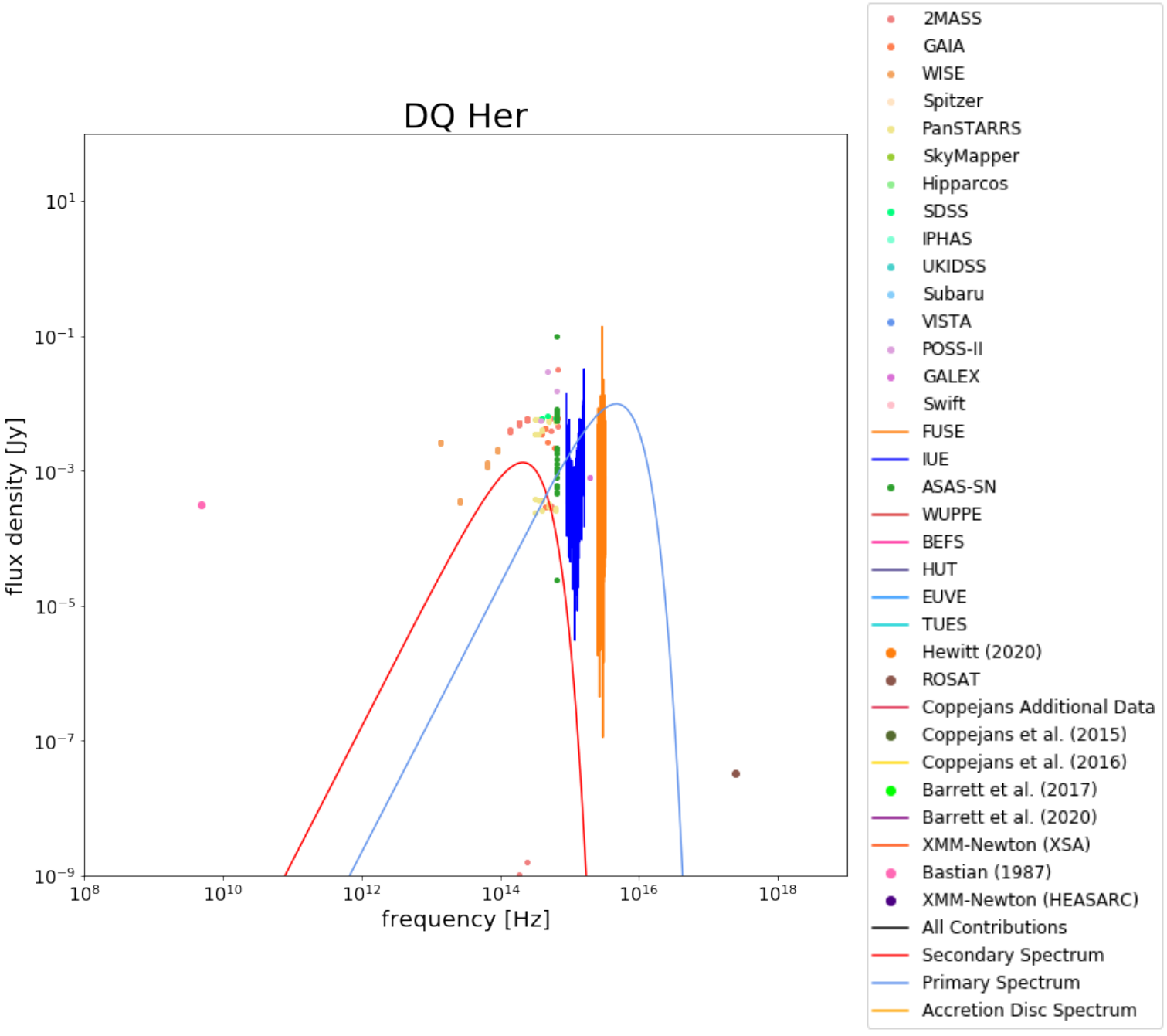

Figure 44: The broad SED of the intermediate polar DQ Her. Overplotted are the contributions of the red dwarf (red) and white dwarf (blue). Different colours give the facility or survey from which data were obtained (see the legend to the right).

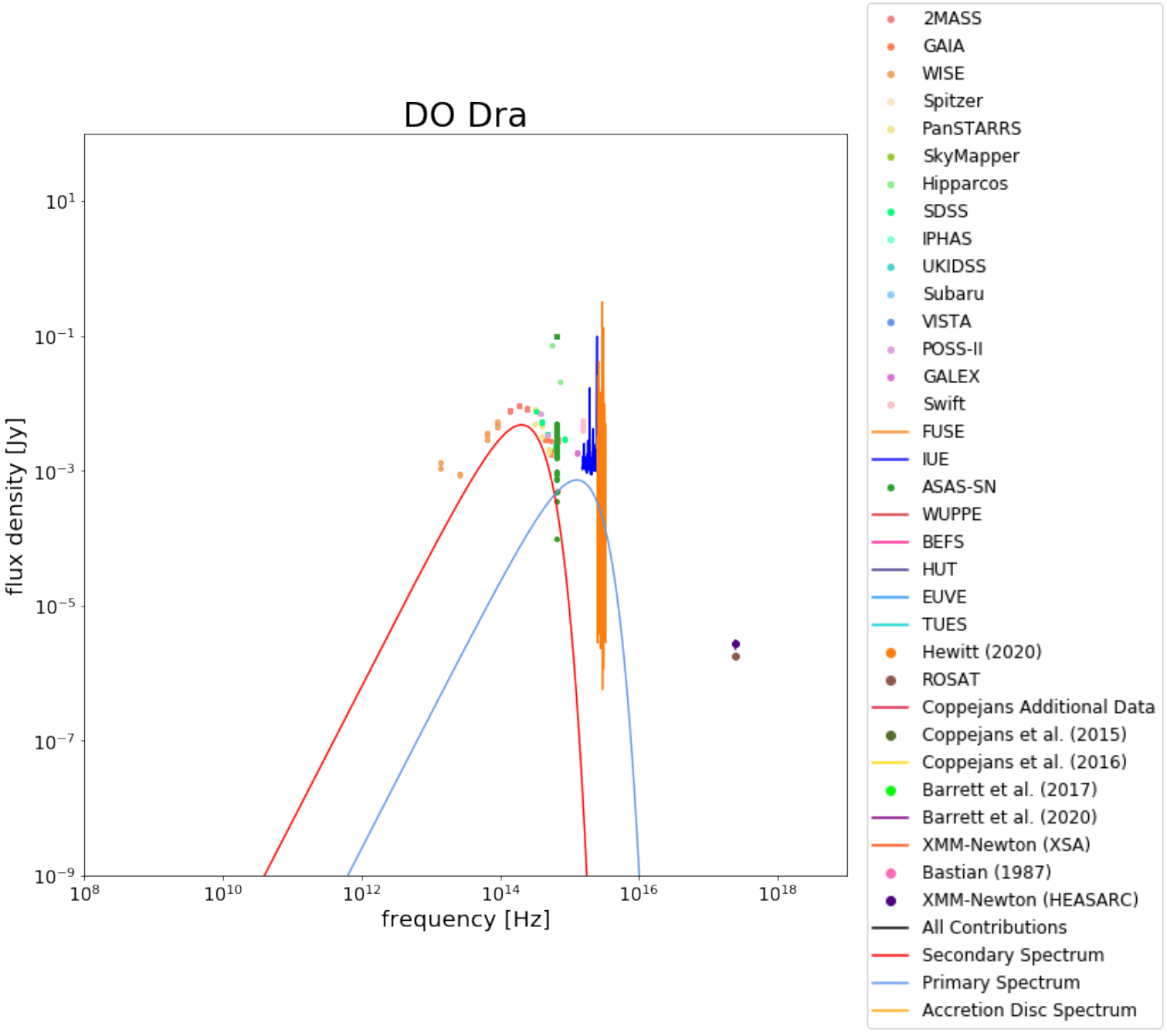

Figure 45: The broad SED of the intermediate polar DO Dra. Overplotted are the contributions of the red dwarf (red) and white dwarf (blue). Different colours give the facility or survey from which data were obtained (see the legend to the right).

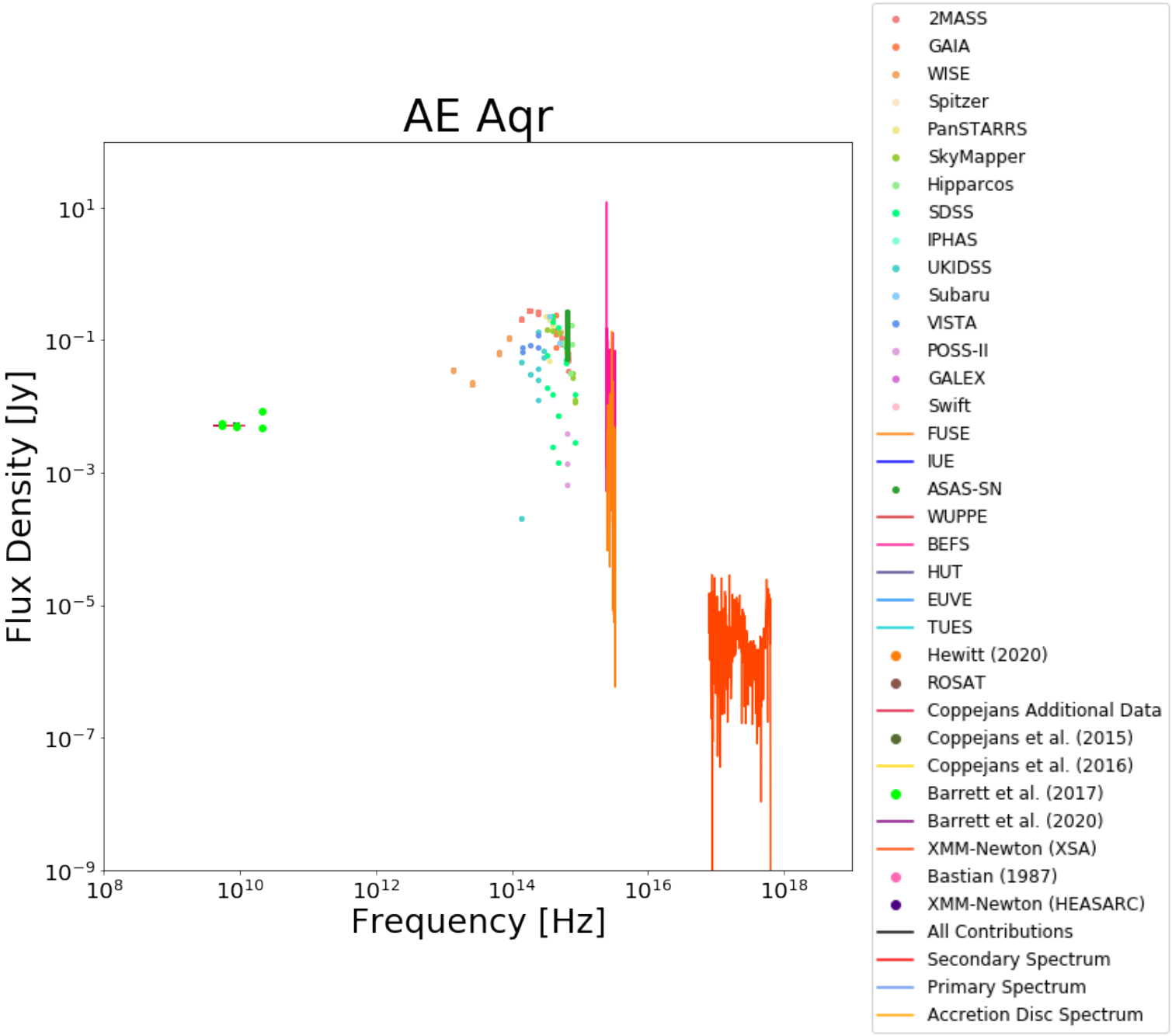

Figure 46: The broad SED of the intermediate polar AE Aqr. The spectra of the stellar components have not been overplotted as the radius of the donor and the temperature of the primary were not available in the literature. Different colours give the facility or survey from which data were obtained (see the legend to the right).

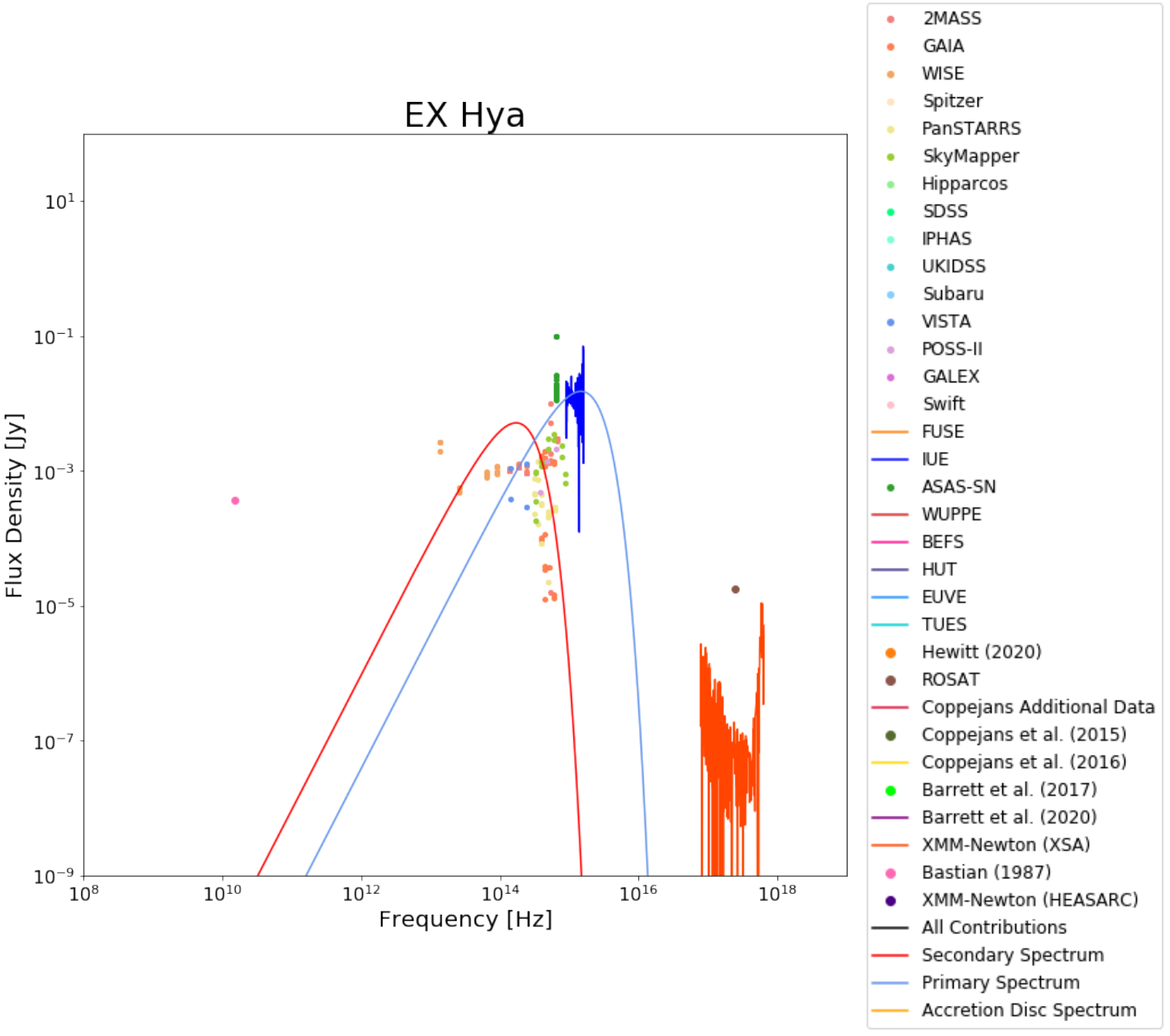

Figure 47: The broad SED of the intermediate polar EX Hya. Overplotted are the contributions of the red dwarf (red) and white dwarf (blue). Different colours give the facility or survey from which data were obtained (see the legend to the right).

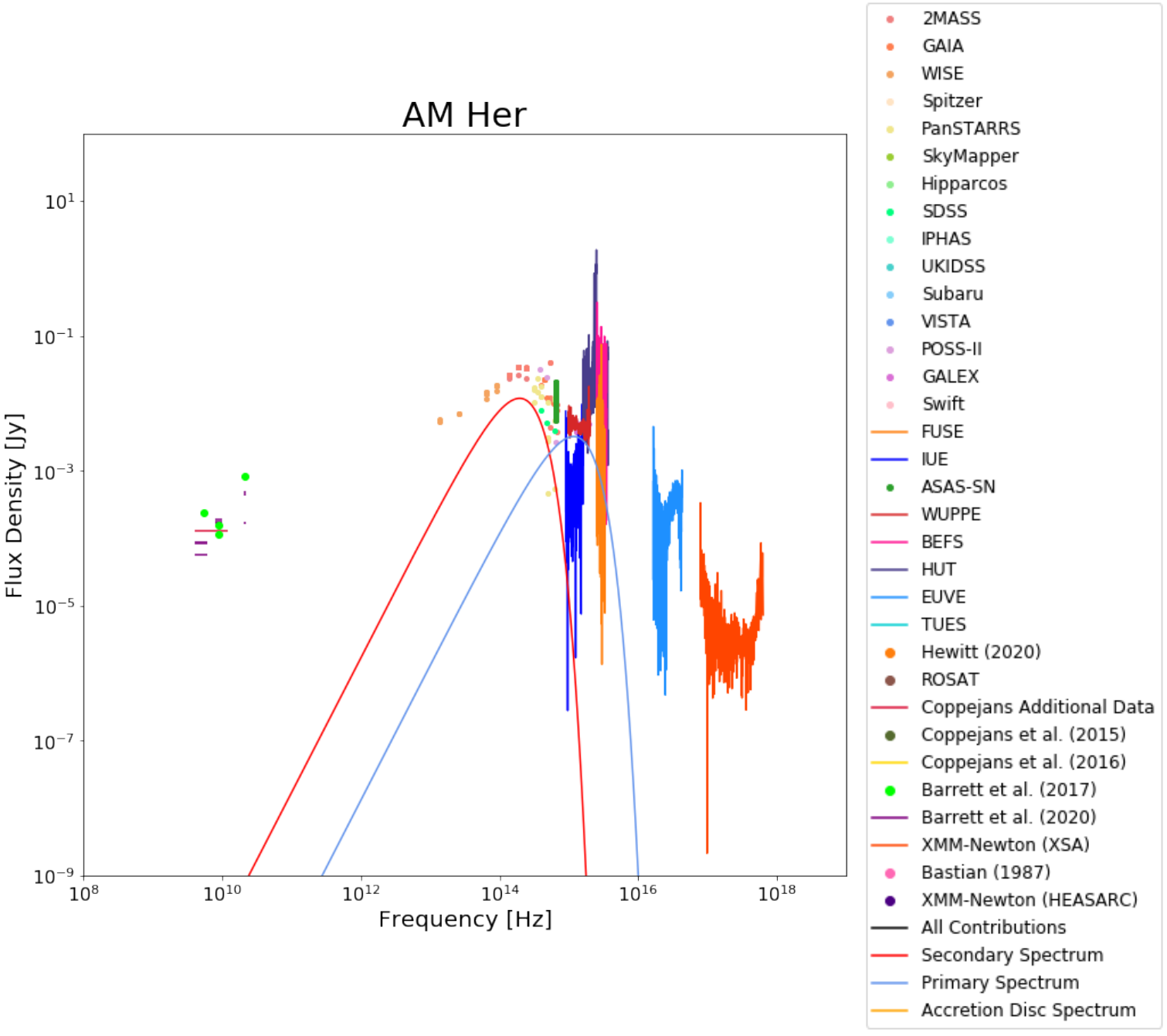

Figure 48: The broad SED of the polar AM Her. Overplotted are the contributions of the red dwarf (red) and white dwarf (blue). Different colours give the facility or survey from which data were obtained (see the legend to the right).

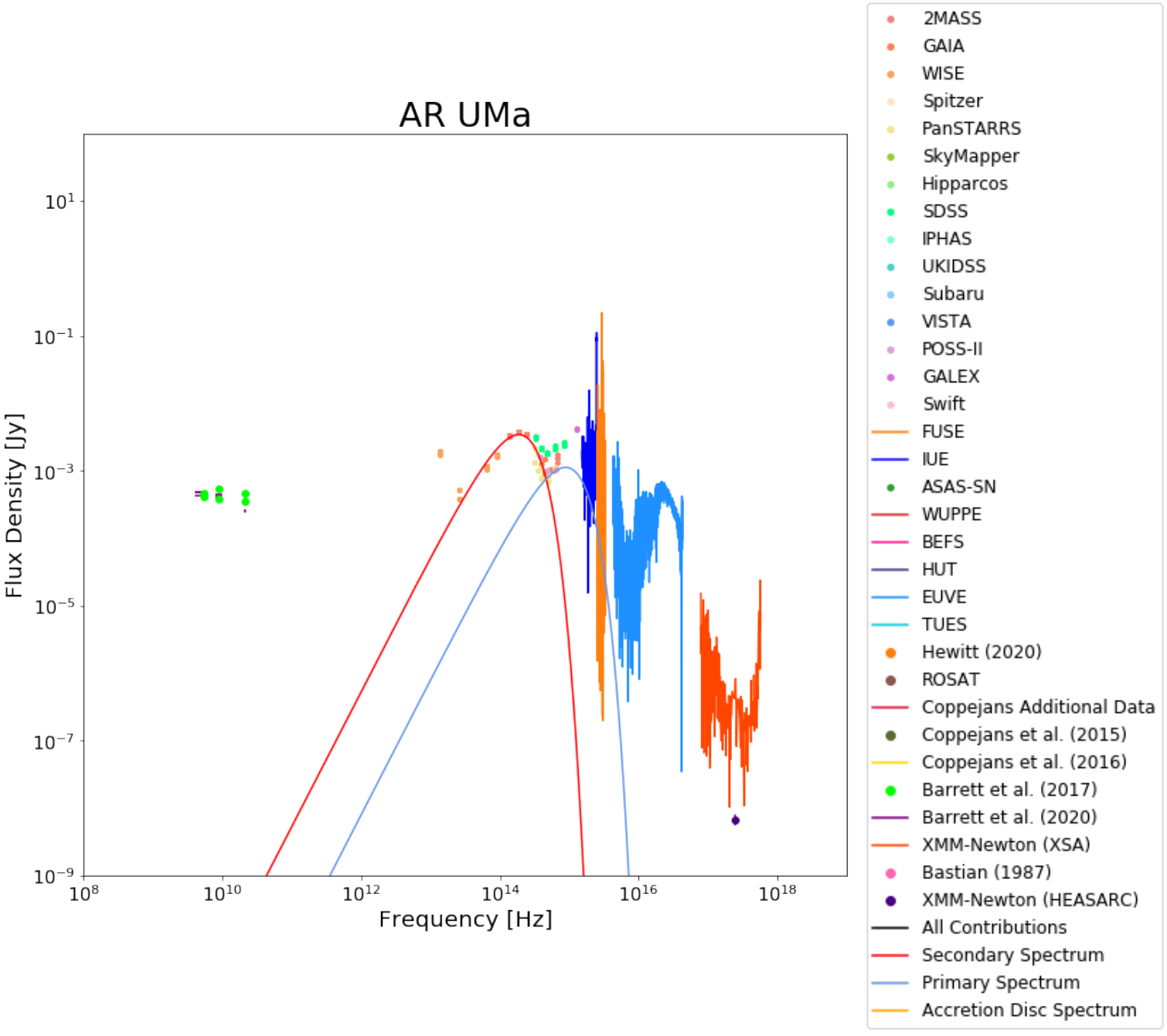

Figure 49: The broad SED of the polar AR UMa. Overplotted are the contributions of the red dwarf (red) and white dwarf (blue). Different colours give the facility or survey from which data were obtained (see the legend to the right).

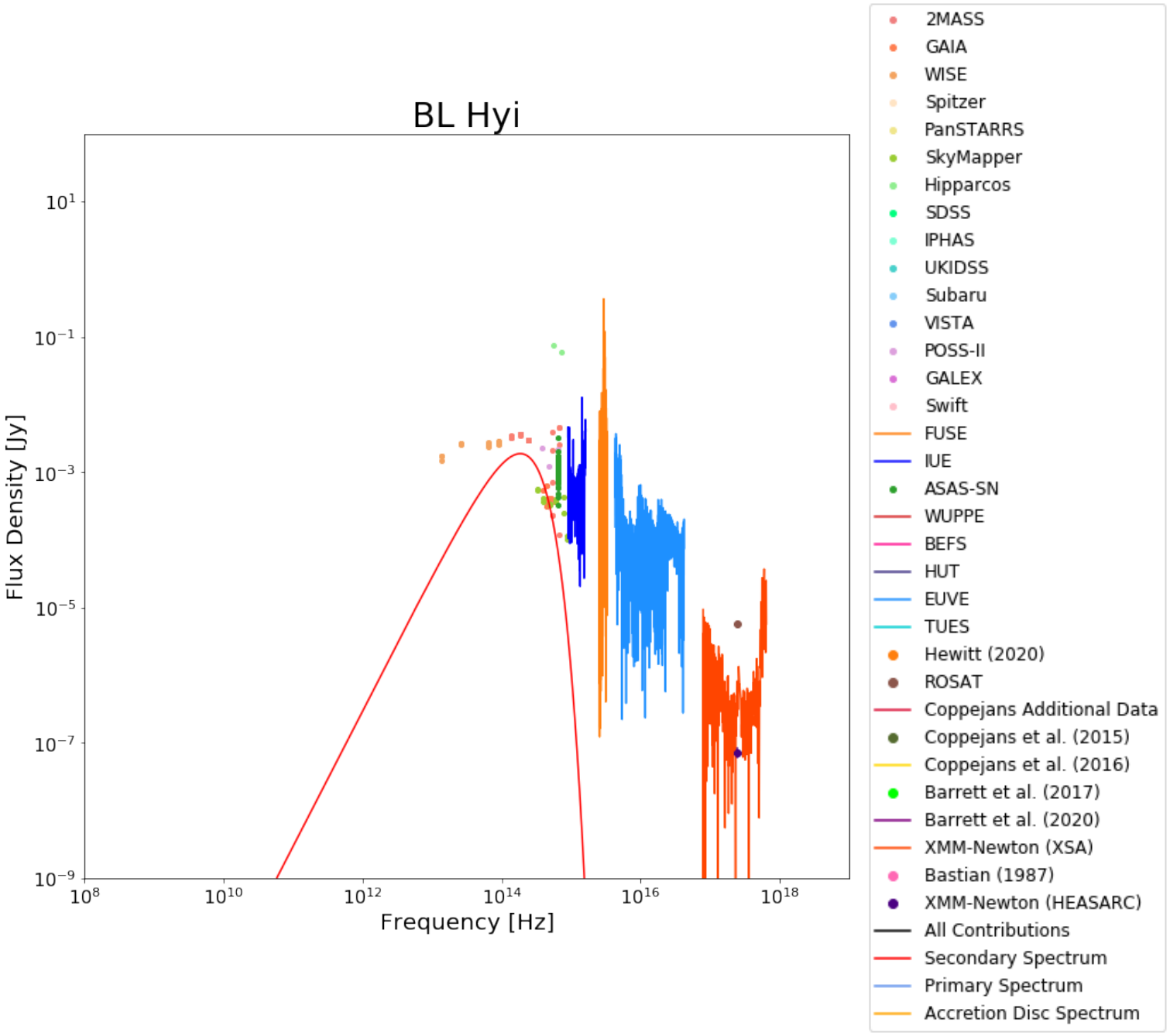

Figure 50: The broad SED of the polar BL Hyi. Overplotted is the contribution of the red dwarf (red). The contribution of the white dwarf has not been plotted, as its temperature is not available in the literature. Different colours give the facility or survey from which data were obtained (see the legend to the right).

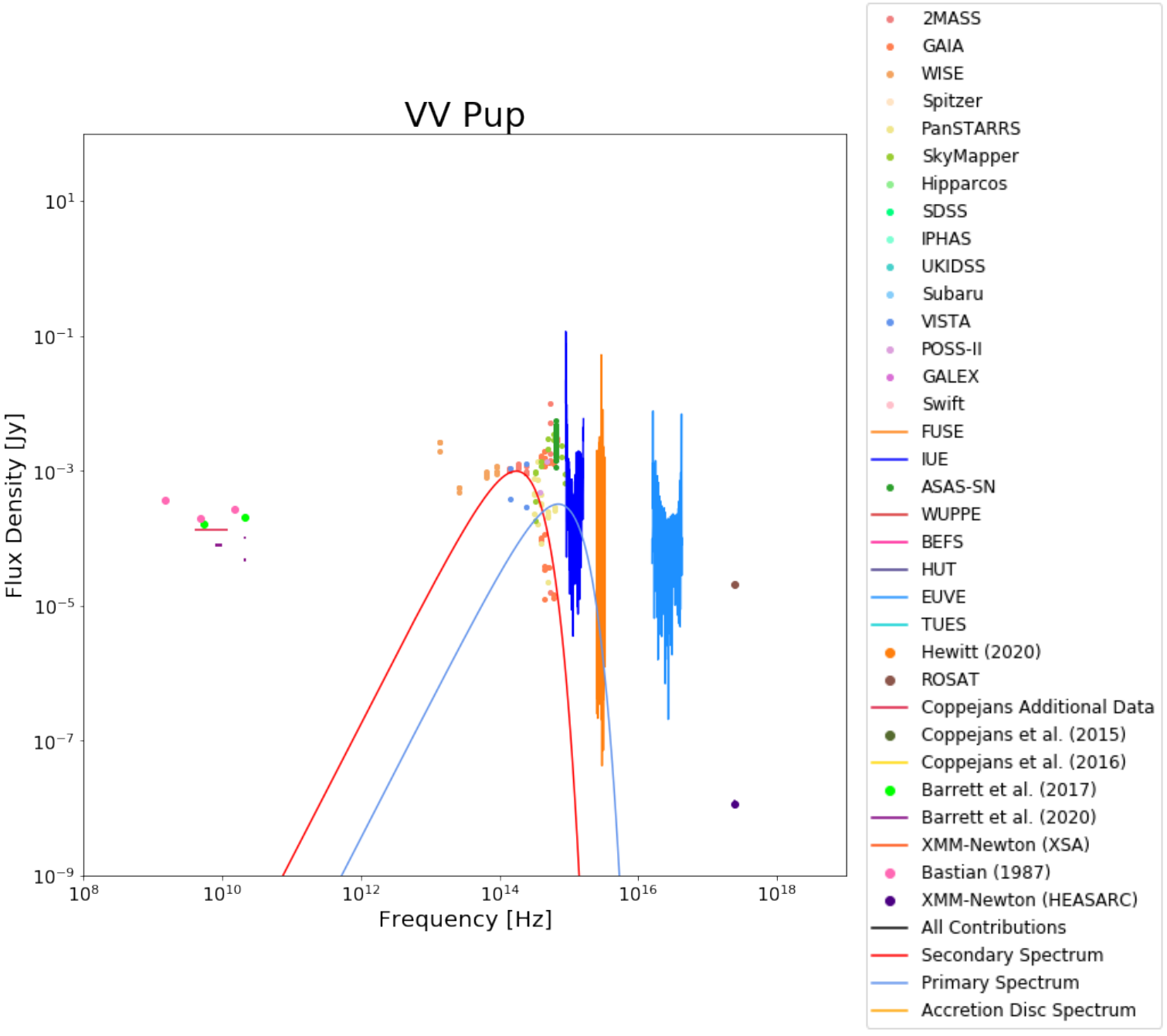

Figure 51: The broad SED of the polar VV Pup. Overplotted are the contributions of the red dwarf (red) and white dwarf (blue). Different colours give the facility or survey from which data were obtained (see the legend to the right).

The accretion disc spectra appear to flatten in the optical, as expected. It is worth noting that, even though the accretion disc is bright in most of these spectra, evidence of the white and red dwarfs are still visible in the data of some of the systems, such as in U Gem in particular, and as a result some of the combined spectra are bimodal (see Section 2.9.10.

The stellar components of V603 Aql (see figure 36) are particularly dim in comparison to the accretion disc, such that the spectrum of the disc is almost indistinguishable from the spectrum the entire system.

The model spectrum of IX Vel (see figure 38) does not appear to fit the data particularly well. The model SED is bimodal even though the observed SED does not appear to be, and there is a brightness peak at about 2×10^{15} Hz that is not well fitted by the combined spectrum. This may be because the properties of the white dwarf from the literature are not correct, and the white dwarf is actually much brighter, peaking at around 0.5 Jy. Increasing the temperature of the white dwarf would increase the brightness of its peak, but also shift the peak to shorter wavelengths. However, the peak of the white dwarf spectrum is already at a slightly higher frequency than the brightness peak in the data. Increasing the mass of the white dwarf while keeping the temperature constant would increase the brightness of its peak without shifting the peak in the frequency domain. By trial and error, I found that for the white dwarf spectrum to fit the data it would require a mass of about $M_1 = 0.15$ $M_\odot$, at the very lowest limit of white dwarf mass. Alternatively, the peak at around $10^{15.5}$Hz may be the contribution of the bright spot, or the strong disc wind that IX Vel is well known for. This is possibly the cause of the brightness in the UV, and may also account for the large UV variability (Hartley et al., 2002). Looking at the ASAS-SN lightcurve (see figure 32), the optical flux varied by about 0.4 mag for most of the last 3 years, but during the last few months appears to be showing a larger range of variability in the optical. Though here IX Vel is considered a nova-like, as mentioned in Section 5.1.3, it may in fact be a Z Cam-type dwarf nova (Kato, 2021).

The model red dwarf spectrum of EX Hya appears to be much brighter than the data. This may be due to a red dwarf temperature that is overestimated in the literature. The data does appear to flatten at the peak of the spectrum, so this may be the result of a red dwarf that is not a good fit for a blackbody. Alternatively, EX Hya is a high-inclination ($i = 76.0° - 77.6°$) eclipsing system, so the anomaly in the data may be a result of the red dwarf being eclipsed during its orbit (Beuermann et al., 2003).

The contributions of the stellar components are also clearly visible in the spectra of the mCVs, particularly that of DO Dra. In figure 52 I plot the spectra of the NLs and

DNe on one page, so they can be easily compared, and zoomed in on the peaks of the accretion discs to show the fits better. In this figure the data are coloured black to indicate that they are included in the fit, and grey to indicate that they are not. Data are excluded from the fit if they are outside the range of infrared – ultraviolet, as emission at those very long and very short wavelengths is dominated by contributions other than the disc or the stellar components. (see Section 2.9). Data was also excluded from the fit if they appeared to include significant outliers. Such datasets included those systems that were significantly broader in the flux density range than in the frequency domain, covering only about one order of magnitude in frequency, but more than three in flux density. Datasets that did not provide errors were also excluded from the fit. The result is that the accretion disc spectra are fitted on data from IRSA, ASAS-SN and *IUE*. It is worth noting that, though some data sources were excluded from the fits due to outliers, the parts of those spectra that are not expected to be outliers, where the majority of the data in the dataset lies, such as *FUSE* in V603 Aql and *HUT* in U Gem, still line up remarkably well with the estimated combined spectra of the systems.

6.1.3 Accretion Rate Estimates

In table 4 are the mass accretion rates of the systems from the literature, as well as the accretion rates I have estimated by fitting the *blackbody()* function, and their corresponding uncertainties. In most cases, while my estimates do not fall within the uncertainty of the accretion rates in the literature (in the cases where an uncertainty was provided), they differ by no more than about one order of magnitude. In the fourth column, I report the reduced χ^2 values for the model fits at the given accretion rates using equations 25 and 26, and in the final column I report the average of the errors for all the data used in the fits.

Reduced χ^2 is a goodness of fit estimate. It is a weighted sum of squared deviations per degree of freedom. For a given fit, if this statistic is close to 1, it is considered a good fit. If it is much greater than 1 it is an underfit, and if it is much less than 1 it is an overfit. Clearly, the formal goodness of fit parameters are poor. My fits do not properly capture the data, and are significantly underfitted. There may be several reasons for this. For one, the data I collected may contain underestimated uncertainties. There were several datapoints and some datasets that had to be excluded from the fits as they did not have uncertainties or their uncertainties were zero. This indicates that reported uncertainties may not be reliable. Many of the datasets were obtained over many decades and many outburst cycles, and were obtained when the sources were in different states and at different points in their outburst cycles. Thus the accretion rates are variable and depend on the state of the system. This is especially true for DNe, which undergo regular outburst periods, but

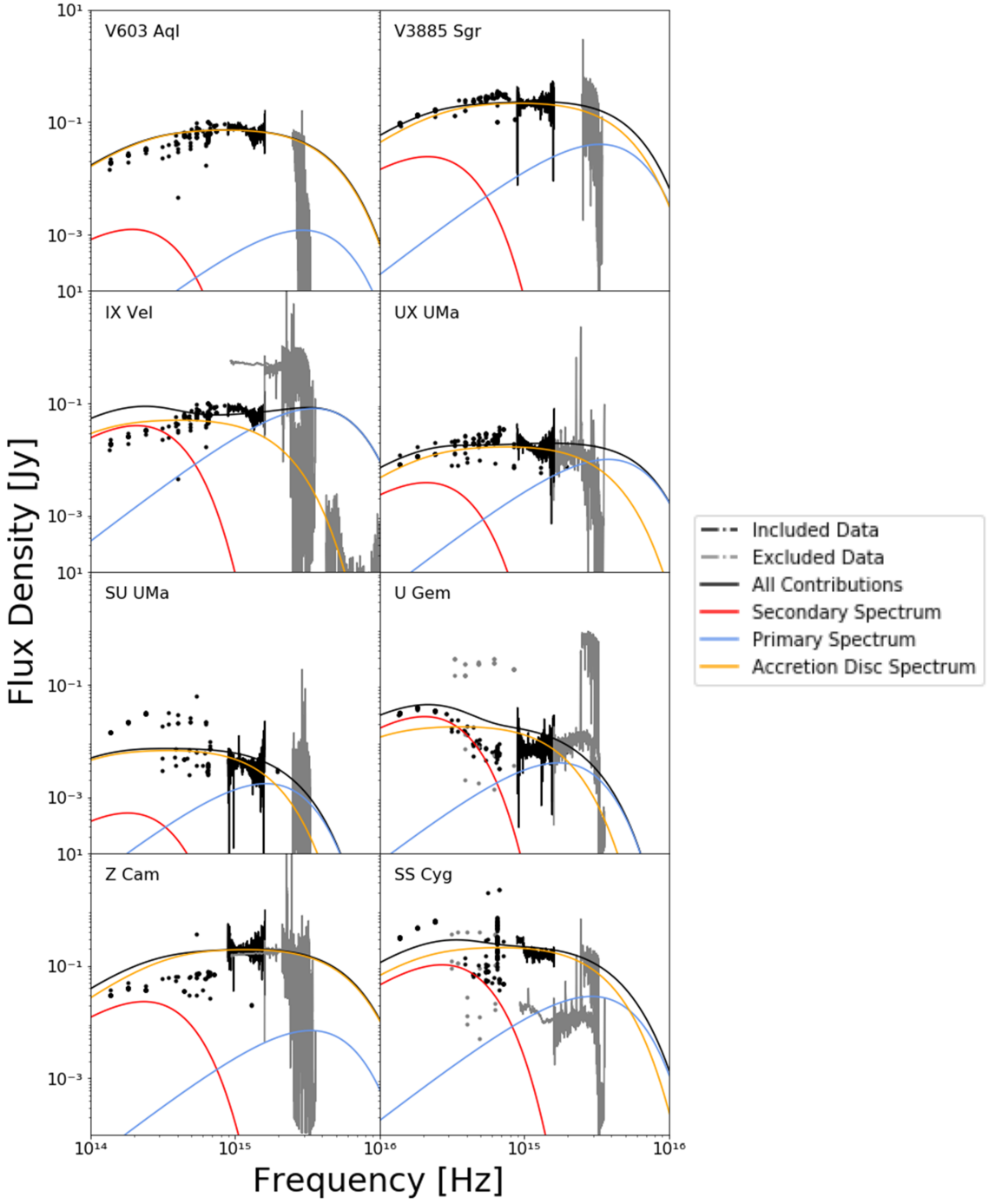

Figure 52: The spectral energy distributions of the nova-like and dwarf nova CVs, zoomed-in on the peaks of the accretion disc spectra. Overplotted are the contributions of the red dwarf (red), white dwarf (blue) and accretion disc (amber), as well as their combined contributions (black), the sum of the spectral contributions of the stars and the accretion disc.

is true for the NLs as well. Ideally, observations would be obtained simultaneously, at the same point in the outburst cycle for all sources. As this is impossible to do, studies such as this that aggregate over many outburst cycles are especially useful.

Additionally, the model I am using is quite simple, as it only accounts for the contributions of the accretion disc and the stars, which are modelled simply as blackbodies. It ignores the fact that all of these objects are variable (most significantly the DNe, but the NLs as well) and that the stars are not perfect blackbodies. It does not account for other contributions to the spectrum such as the bright spot, jets, and boundary layer. In some cases input parameters such as primary mass and inclination were not available in the literature or were not well constrained, and had to be estimated. Other variables were also ignored, such as eclipses, occultation of the components, possible parts of the disc that are not part of the blackbody component and self-occultation of the disc. Exposure of the disc rim in high-inclination systems will affect the SEDs of the systems (see Section 2.9.5).

Table 4: Estimates of the accretion rates of the nova-likes and dwarf novae in this study, and their corresponding errors, as well as estimates from the literature.

Name	$\dot{M}$ [$M_\odot$ yr^{-1}] (literature)	$\dot{M}$ [$M_\odot$ yr^{-1}] (this work)	χ^2_{red}	ave. error [mJy]
V603 Aql		$(2.19\pm0.02)\times10^{-9}$	160	5.85
V3885 Sgr	$(5\pm2)\times10^{-9}$	$(5.08\pm0.06)\times10^{-9}$	243	28.99
IX Vel	$(5\pm1)\times10^{-9}$	$(1.68\pm0.04)\times10^{-10}$	509	5.47
UX UMa	$(1\pm0.4770)\times10^{-8}$	$(1.82\pm0.03)\times10^{-9}$	300	2.27
SU UMa	9.8×10^{-13}	$(6.69\pm0.33)\times10^{-11}$	95	0.96
U Gem	$(1.815\pm1.685)\times10^{-9}$	$(3.80\pm0.44)\times10^{-11}$	86587	2.11
Z Cam	1.59×10^{-8}	$(9.41\pm0.21)\times10^{-9}$	431	33.49
SS Cyg	5×10^{-11}	$(1.14\pm0.03)\times10^{-9}$	450207	15.88

The uncertainties quoted in table 4 are very small, and do not contain the majority of the data. In figure 53 I plot the SEDs, overplotted with the combined spectra of all contributions, the sum of the spectral contributions of the stars, and the best-fit accretion disc. I have also plotted the spectra of all contributions where the accretion rates have been adjusted by factors of two and five from the best-fit accretion rate ($\dot{M}' = 2\dot{M}; 0.5\dot{M}; 5\dot{M}; 0.2\dot{M}$). As is clear from these plots, most of the data included in the fits is contained within a factor of two, and almost all within a factor of five.

The shapes of the CV spectra change in these plots. This is because, in the cases where the accretion rate in the model is greater than my estimate ($\dot{M}' = 2\dot{M}$ and $5\dot{M}$), the contribution of the stars is less significant in comparison to the accretion disc, and therefore the combined spectrum is smoother. In the cases where the

accretion rate in the model is less than my estimate ($\dot{M}' = 0.5\dot{M}$ and $0.2\dot{M}$) the accretion disc is dimmer, and the stars are therefore brighter by comparison, so their contribution to the spectrum is more significant, in some cases causing the spectrum to be bimodal (see Section 2.9.10).

As is evident from figure 53 and the reduced χ^2 values in table 4, the formal errors returned by the fitting routine are not realistic. About half of the accretion rate estimates are accurate to within a factor of 5 of the estimates in the literature, however, the estimates for IX Vel, SU UMa, U Gem and SS Cyg are well outside of this margin of error. U Gem and SS Cyg both have particularly large reduced χ^2 values, indicating that the fits for these systems are particularly poor. This may be due to significant variability in the data, particularly large errors, or simply poor fits. However, from the average errors listed in table 4, it is clear that, in this sample, neither large differences between the calculated accretion rates and those in the literature, nor large reduced χ^2 values, correlate with large average errors in the data. In figure 54 I plot the maxima and minima of the ASAS-SN g-band data for the past three years in green, overplotted with the combined spectra for the systems. As is clear from these plots, the flux range for data in the visible region is quite broad, and my SED fits for these systems do lie within this range.

6.1.4 A Comparison of the Spectral Properties between CV Classes

In figure 55 I have plotted the spectral data of all 16 the systems in my sample. Here all SEDs are plotted on the same scale, to facilitate a comparison between them. The NLs are plotted in the top row of panels, the DNe in the second row from the top, the IPs in the row third from the top, and the polars in the bottom row.

As already noted in Section 6.1.1, the nova-like and dwarf-novae systems appear to have blackbody-like spectra in the infrared to ultraviolet domain, while the IP and polar systems tend not to, appearing to have a flatter spectrum throughout the entire frequency domain. However, some parts of the spectra of some of the magnetic CVs, such as DQ Her, DO Dra, AM Her and AR UMa, appear to have a blackbody-like shape, likely evidence of the stellar components. Also visible in these SEDs are the contributions in the radio, possibly from jets, and in the X-ray, from the boundary layer for nova-likes and dwarf novae and the accretion column for IPs and polars.

The DN and NL SEDs are relatively uniform, with a clear blackbody-like spectrum, though the DNe tend to be quite variable in the visible range, as they outburst semi-regularly, causing variability in the SED data. In contrast, the IPs and polars are much more heterogenous. While DQ Her and DO Dra have relatively similar spectra, that are similar to those of the non-magnetic systems, the other magnetic

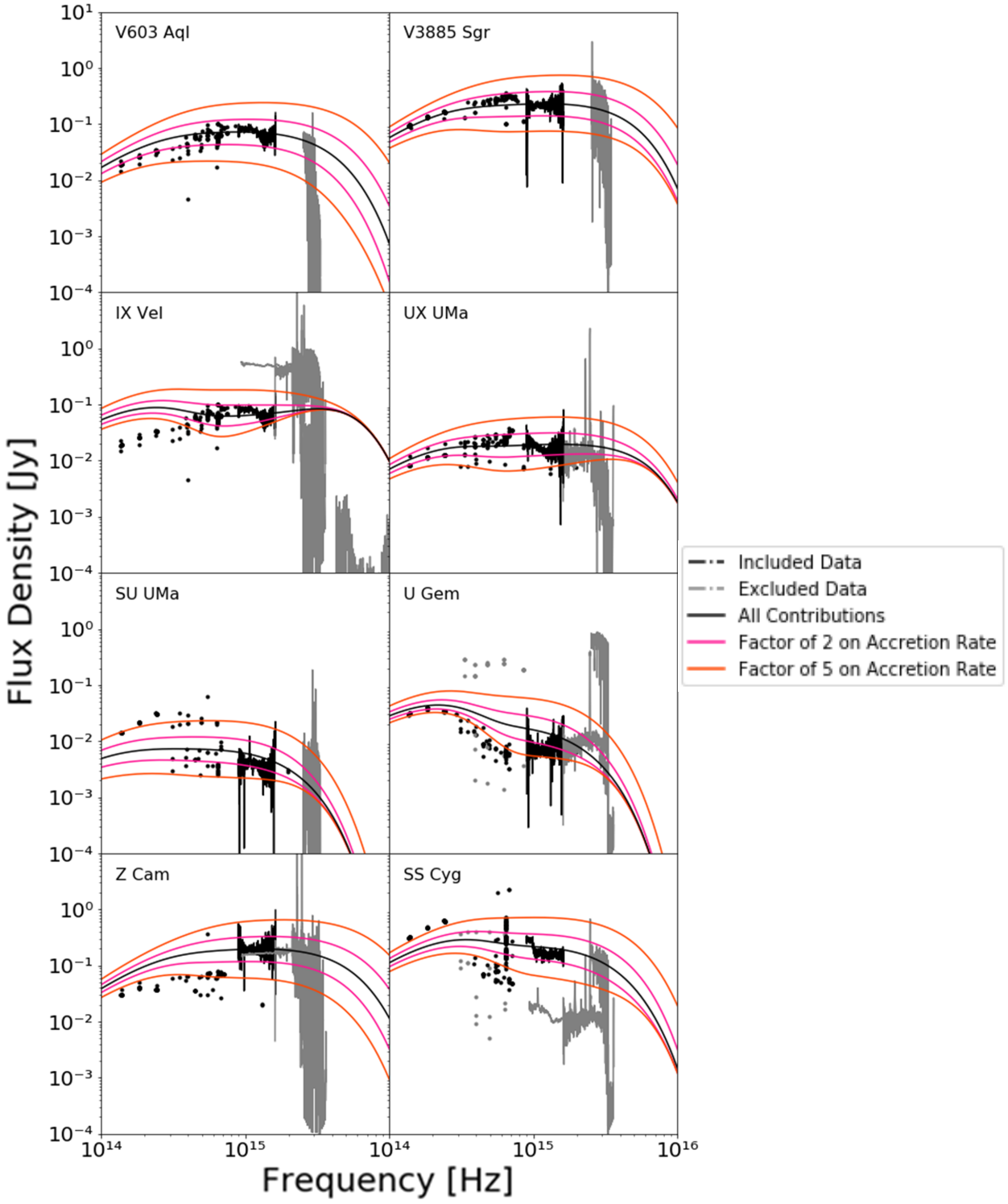

Figure 53: The spectral energy distributions of the nova-like and dwarf nova CVs, zoomed-in on the peaks of the accretion disc spectra. The black curve is the best fit disc model plus the contributions of the white dwarf and donor star. The pink curves are the same, except the accretion rate of the disc model has been adjusted by a factor of 2 ($\dot{M}' = 2\dot{M}; 0.5\dot{M}$). For the orange curves, the accretion rate of the disc model has been adjusted by a factor of 5 ($\dot{M}' = 5\dot{M}; 0.2\dot{M}$).

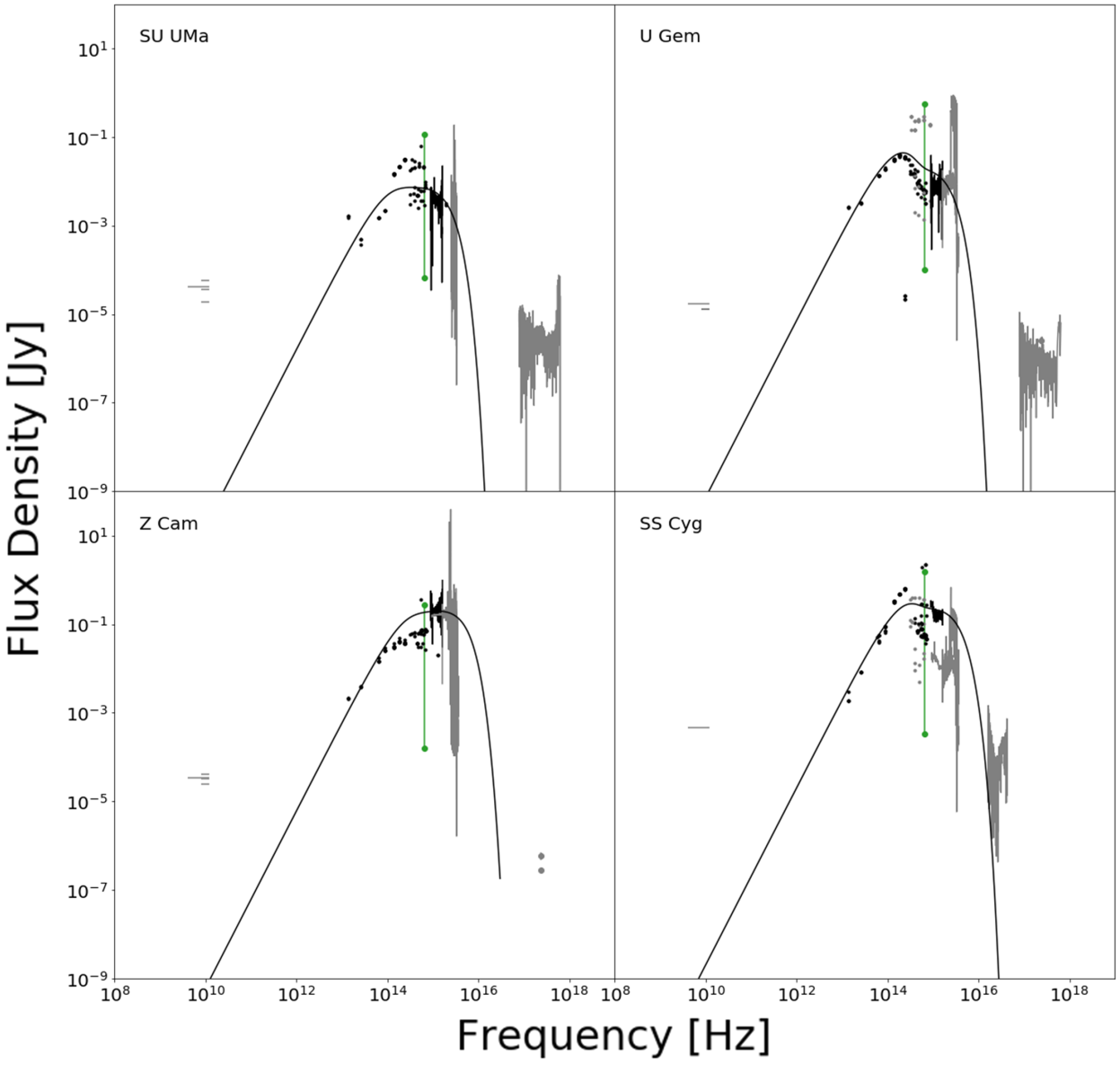

Figure 54: The SEDs of the dwarf-novae in my sample with data that is included in the fits shown in black and data that is excluded shown in grey. Overplotted is the combined spectra of the stars and accretion disc, as well as the maxima and minima of the ASAS-SN g-band data for the past three years, in green.

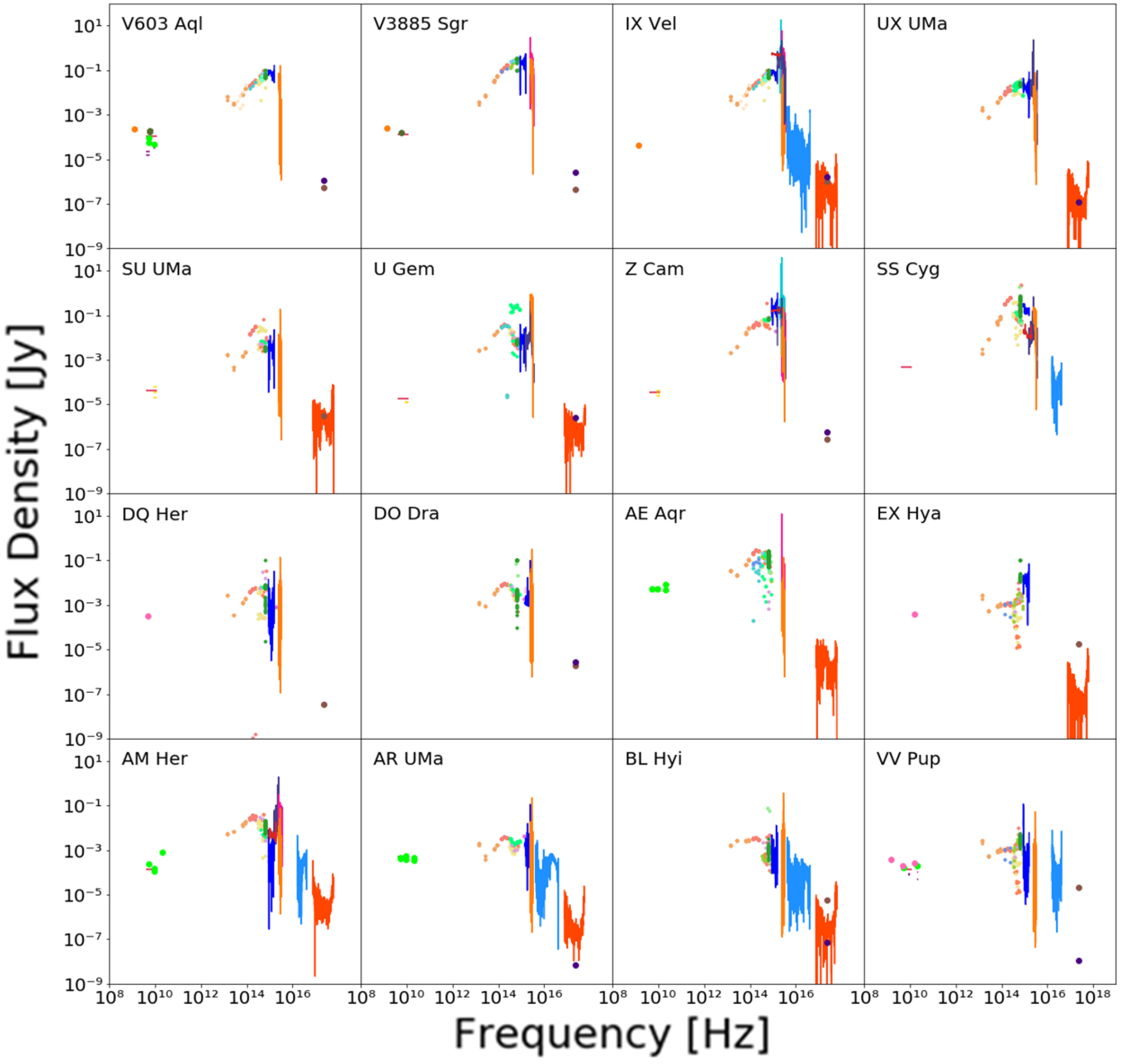

Figure 55: The spectral energy distributions of the 16 systems observed in this study. Top row: Nova-likes. Second row: Dwarf novae. Third row: Intermediate polars. Bottom row: Polars. See the detailed SEDs presented in further in Section 6.1.2 for a legend specifying the meaning of the different colours.

systems are not much alike.

Most of the magnetic systems appear to have much higher radio flux densities, compared to their IR, optical, and UV flux densities, than do the non-magnetic systems. In order to illustrate this more clearly, and to identify anything else that my be apparent from comparing the flux densities in different wavebands, I plot flux density ratios in this section. Refer to Section 4.4.8 for a detailed description of how this was achieved.Figure 58 shows the X-ray/UV, X-ray/vis, and X-ray/radio flux ratios. Data in X-ray/radio, is a bit sparse, but there doesn't appear to be any correlation. X-ray/UV and X-ray/Vis are similar. Shorter-period systems have a higher X-ray to optical ratio than do longer-period systems. This correlation has been noted before by van Teesling & Verbunt (1994). The ratios in all of these plots are less than one. The X-ray flux is typically less than the ultraviolet flux, especially in high-accretion rate systems. On average the magnetic systems have larger X-ray to optical flux ratios. Magnetic CVs are expected to have high X-ray luminosity due to their radial accretion flow, particularly in polar CVs. This expectation has also been observed before, by Beuermann & Thomas (1993).

Since it has not been explicitly shown in the literature before, in order to further illustrate the observation that polars are radio bright in comparison to non-magnetic CVs, I plot the radio/visible flux density ratios of all CVs with radio detection from Barrett et al. (2017, 2020); Coppejans et al. (2015, 2016b); Hewitt (2020) and Coppejans' additional radio data in figure 59. Visible flux densities are in the *GAIA* G-band, retrieved from IRSA. Any CVs that were not detected in the radio in these papers were excluded from the sample, as well as any systems that did not have *GAIA*-G data recorded by IRSA. Orbital periods were taken from the papers in which radio detections were published. For Coppejans' additional radio data, which reports luminosities, distance estimates *GAIA* and used in equation 19 to convert these readings to Jansky (Bailer-Jones et al., 2018).

The average of all detections for each source was taken. Any detections that did not include an error were excluded. As is clear from the plot, the trend of radio brightness of polars in comparison to non-magnetic CVs remains for a larger sample.

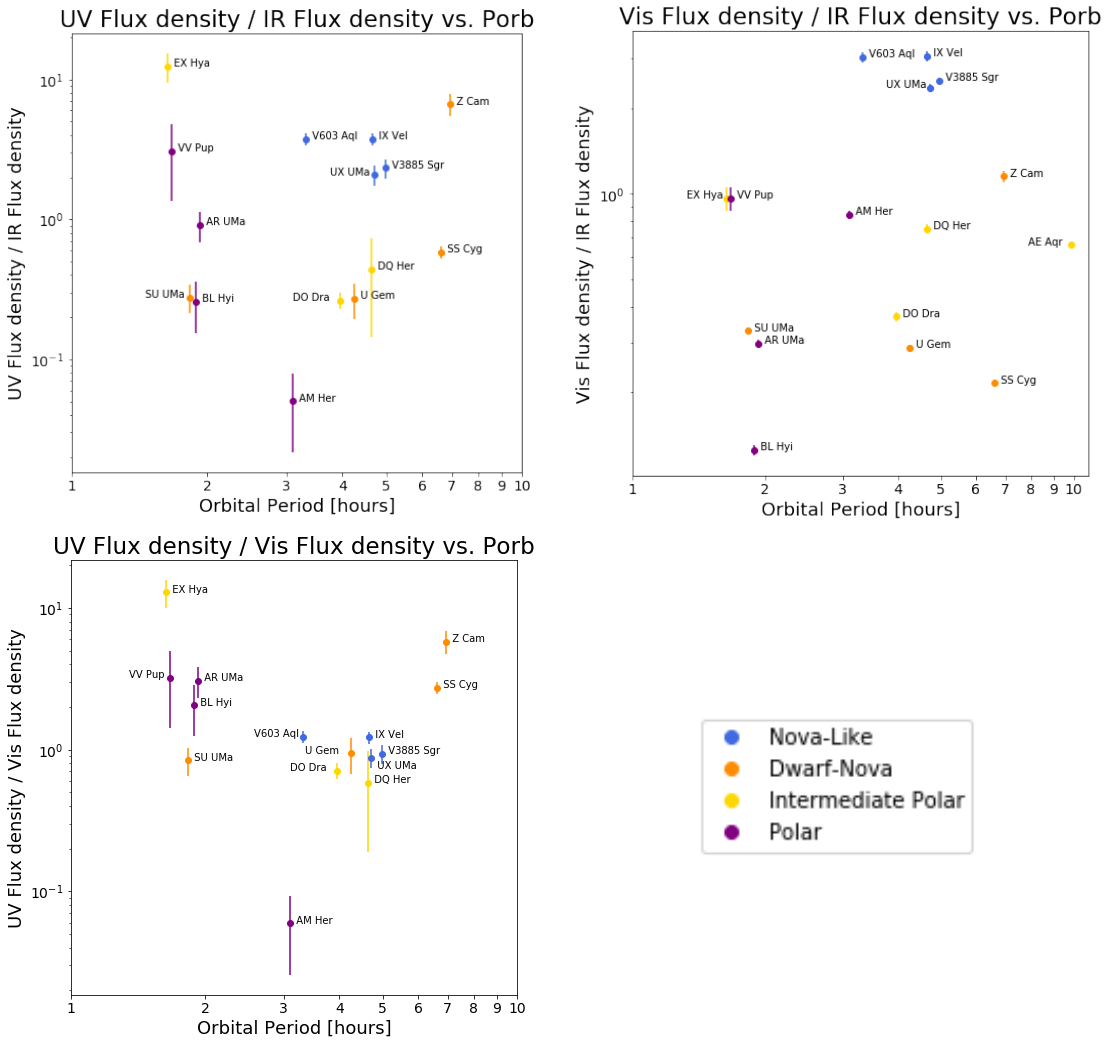

Figure 56: Flux density ratios of the infrared, visible, and ultraviolet wavebands.

Figure 56 shows the UV/IR, vis/IR, and UV/vis flux ratios. These flux density ratios appear to be evenly distributed, and have little correlation with the orbital period. In the wavelength region where the accretion disc is most prominent, in the infrared to ultraviolet range, the nova-likes appear to have a similar flux density ratio, while the ratios of the other types tend not to be so predictable. AM Her is an outlier in the UV/Visible plot, having a ratio almost an order of magnitude lower than the rest of the sample.

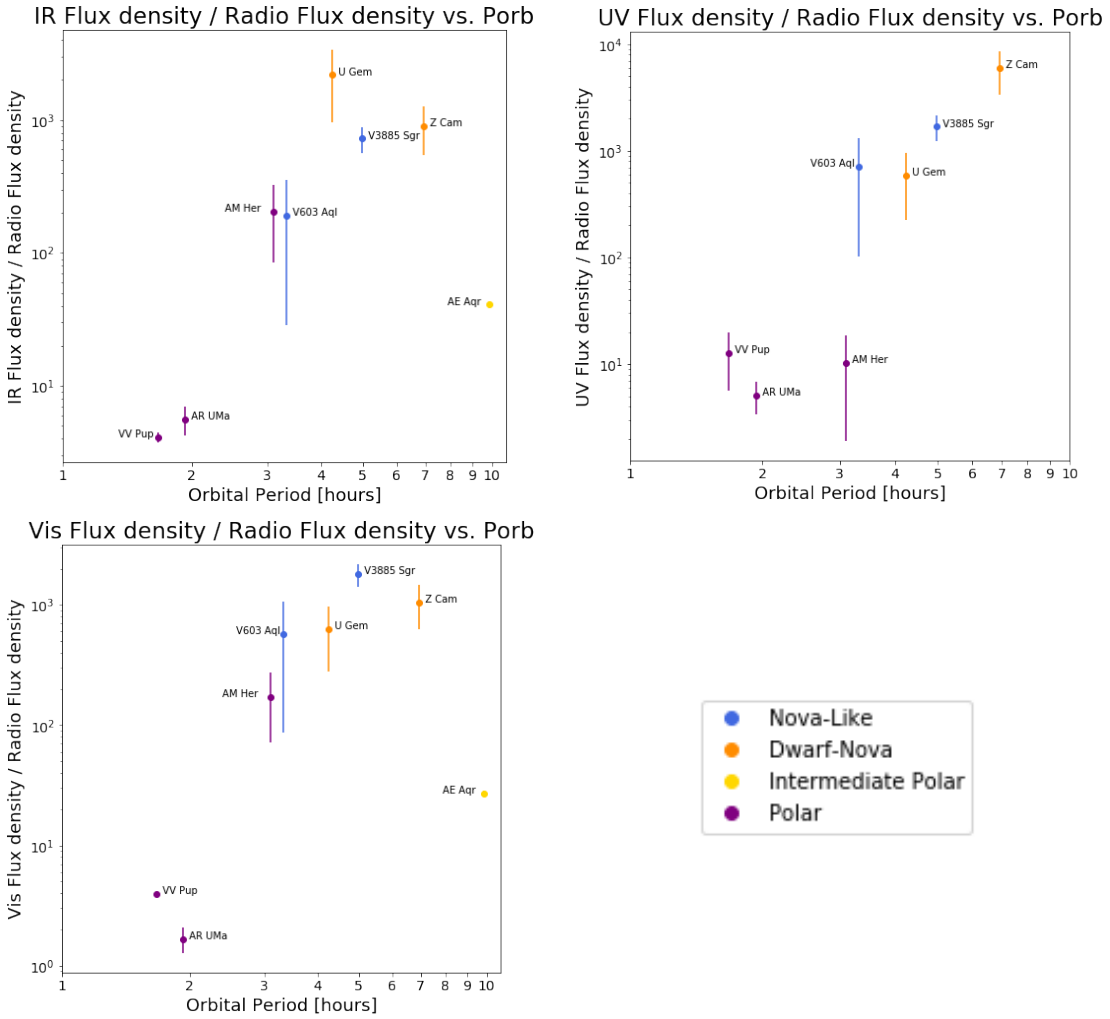

Figure 57: Flux density ratios of the infrared, visible, and ultraviolet wavebands over the radio waveband.

Figure 57 shows the IR/radio, UV/radio, and vis/radio flux ratios. Here one can compare the brightness of accretion light vs. radio emission. The polars tend to be radio bright compared to the non-magnetic CVs, however, once again AM Her is anomalous. AM Her is the only long-period (above the period gap) polar in my sample; the vast majority of polars are short-period systems. This may why it is different.

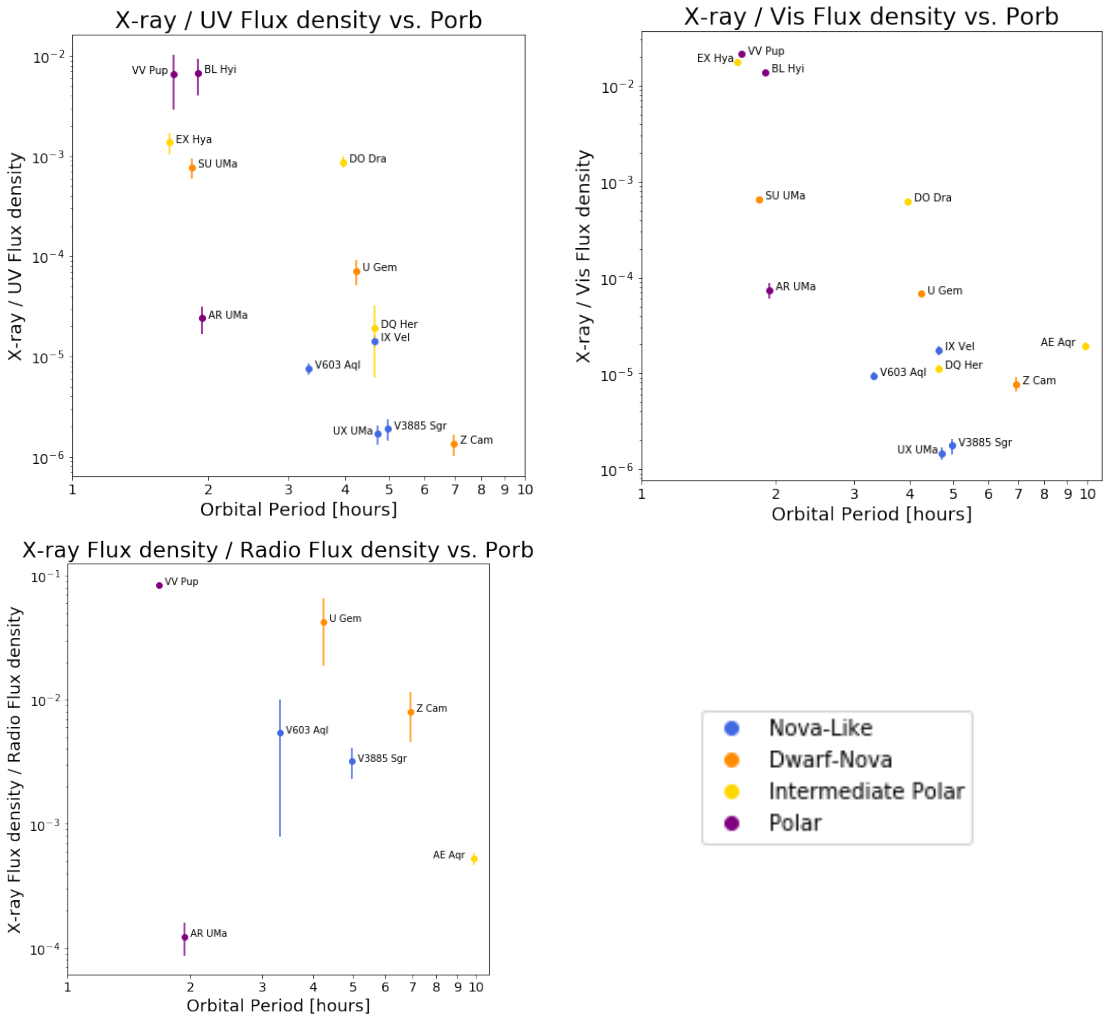

Figure 58: Flux density ratios of the X-ray waveband over the ultraviolet, visible and radio wavebands.

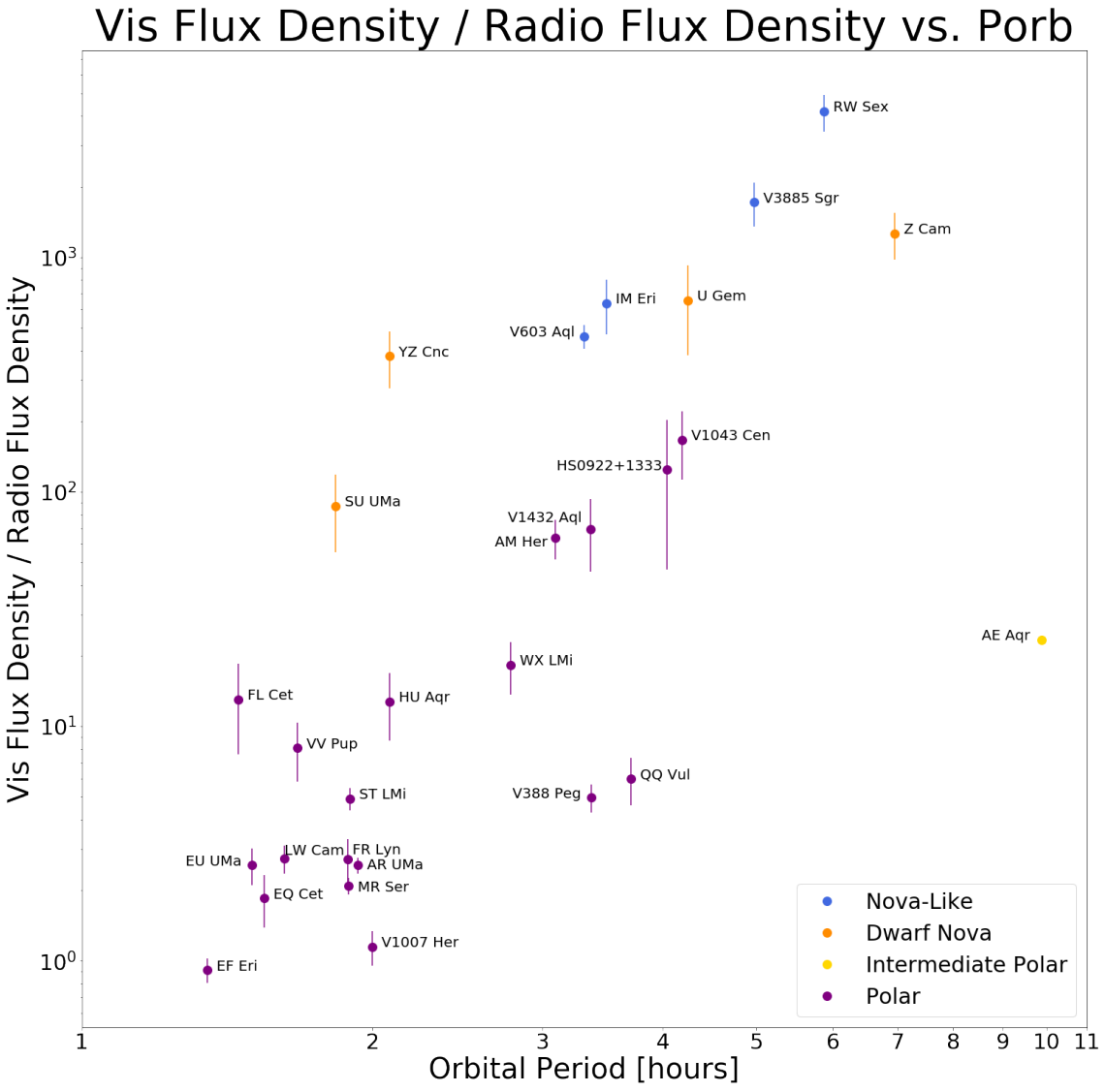

Figure 59: The Visible Flux Density / Radio Flux Density vs. Orbital Period for a large sample of CVs with radio detections.

6.2 Pala et al. (2020) Volume-Limited Sample

I attempt here to estimate accretion rates for the non-magnetic CVs in the sample of Pala et al. (2020). Because this sample is volume-limited, and hence not affected by observational bias, a complete set of mass transfer rates for these systems should be powerful in constraining CV evolution theory.

6.2.1 SED Fits and Accretion Rate Estimates

An Attempt to Fit Disc Models to the SEDs of the Pala et al. (2020) Sample

I have compiled SEDs for the non-magnetic systems in the Pala et al. (2020) volume-limited sample of CVs, using only IR, visible, and UV data provided by IRSA. The SEDs and fits, obtained from the *blackbody()* function, are shown in this subsection, and the accretion rate estimates resulting from these fits are also listed here.

I plot the spectra of the nova-likes and dwarf novae of the Pala et al. (2020) volume-limited sample of CVs in figure 60. I use data from IRSA, and use the *blackbody()* function to fit the spectra. The input values for the *blackbody()* function are taken from Pala et al. (2020). CVs from the sample where IRSA data are not available are excluded. Any datapoints that do not include an error, have an error of zero, or have an error greater than their flux are excluded. This is why some of these plots, such as V627 Peg, GW Lib and IP Peg, are so sparse. The datasets of some systems include no flux readings with appropriate errors, and these systems are also excluded. The white dwarf and red dwarf contributions are not subtracted.

Some of these spectra do appear to fit the data well, such as IX Vel and V3885 Sgr. It is however clear from these plots that almost all of these fits are unacceptable. What this means is that this quick and simple method of fitting that takes a small dataset and does not account for the contributions of other spectral components is not accurate, and would not be useful on a larger sample of systems that may contain systems that are not so well-studied.

I use these fits to estimate accretion rates for the systems. These results, along with their uncertainties and reduced χ^2 values, are listed in table 5. These results are all within about two orders of magnitude of Pala et al. (2020)'s estimates, but, as is clear from the plots, they are generally not good estimates. This is reflected in the reduced χ^2 values for the fits which are generally unacceptably large and vary significantly. The reduced χ^2 values of V627 Peg, GW Lib and IP Peg appear to indicate that the fits for these systems are either acceptable or overfitted, but this actually reflects the lack of data for these systems, which is evident in their plots.

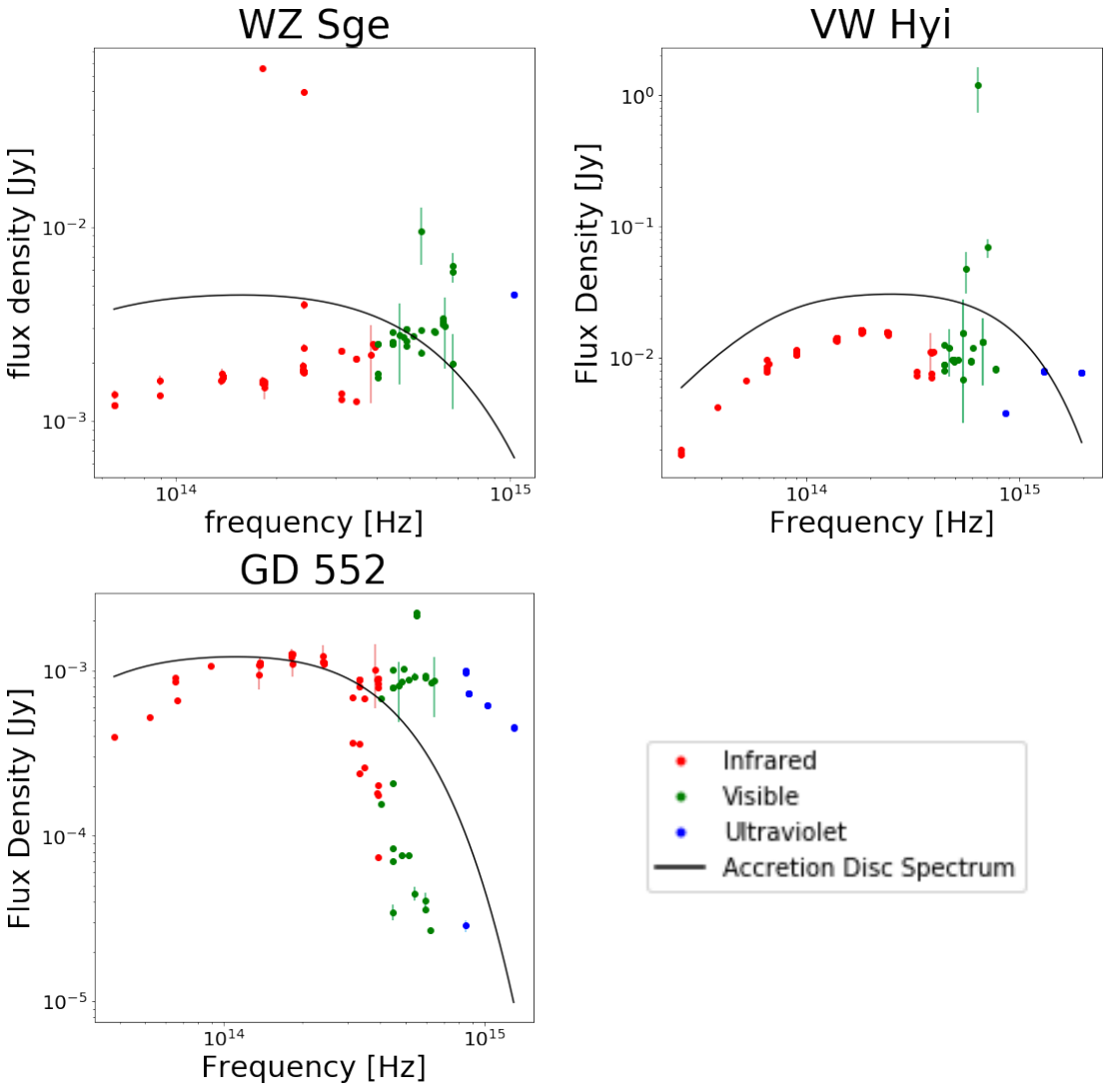

Figure 60: The spectral energy distributions of the Pala et al. (2020) volume-limited sample, overplotted with the best-fit model spectra.

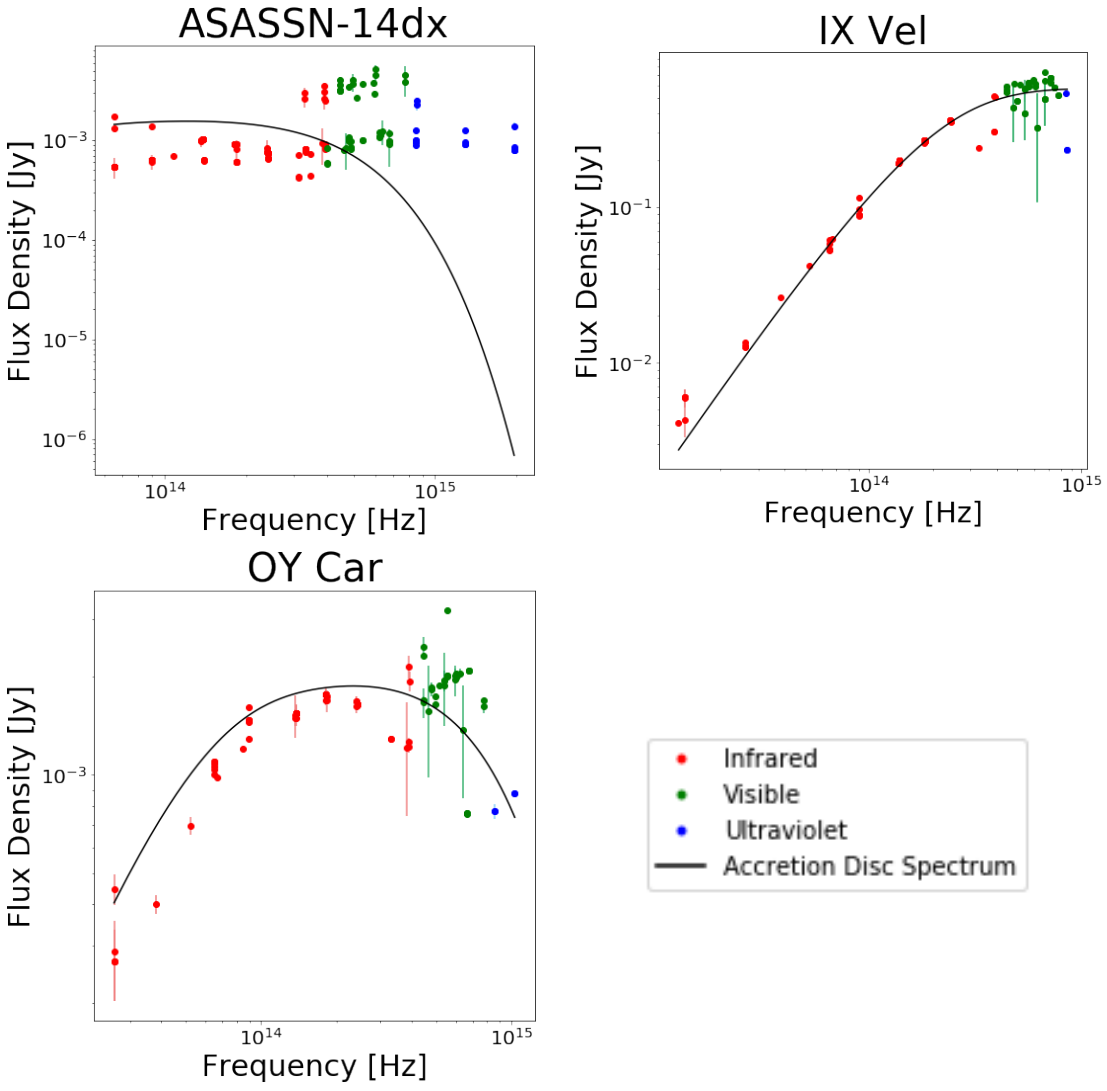

Figure 60: The spectral energy distributions of the Pala et al. (2020) volume-limited sample, overplotted with the best-fit model spectra.

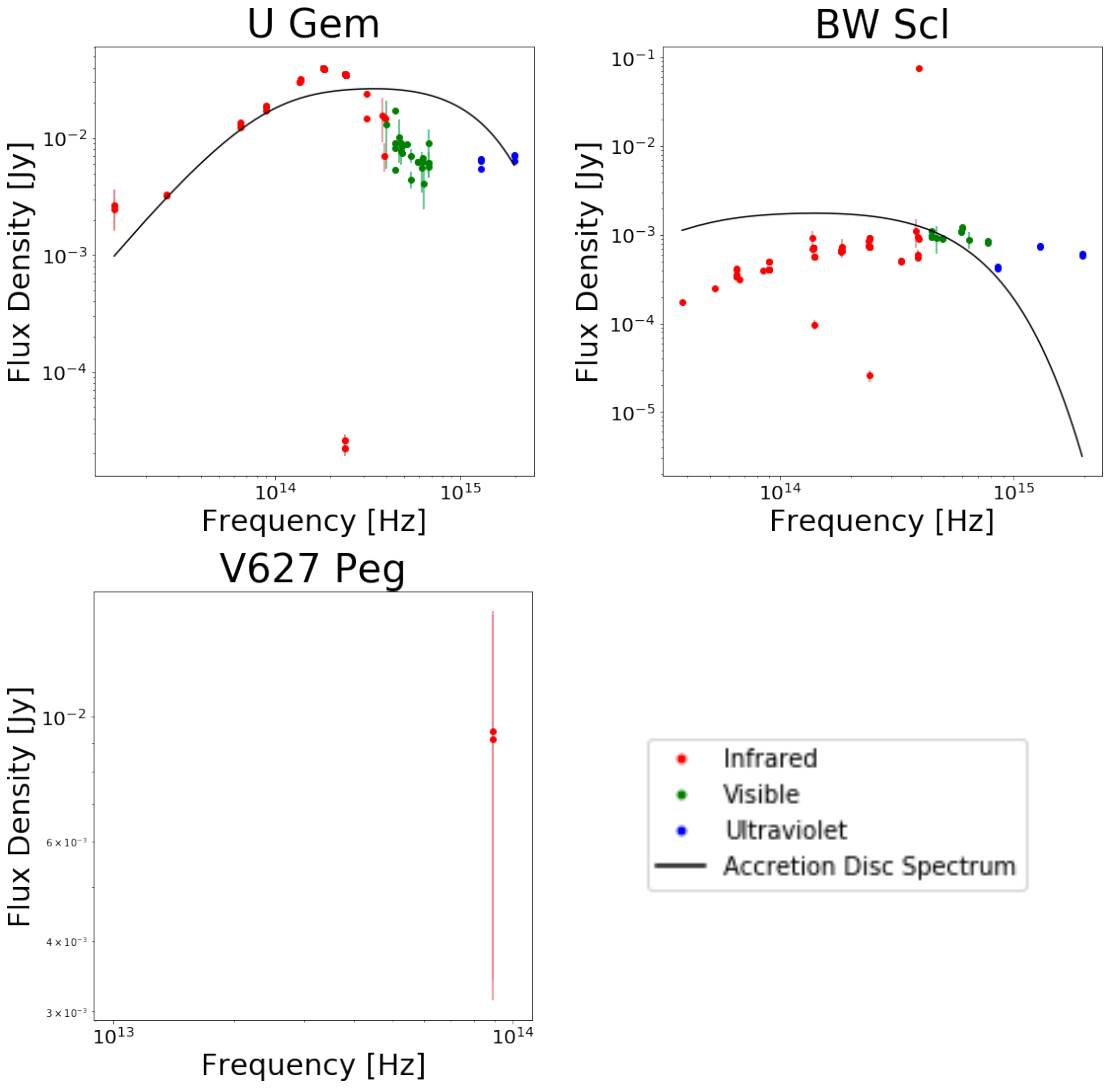

Figure 60: The spectral energy distributions of the Pala et al. (2020) volume-limited sample, overplotted with the best-fit model spectra.

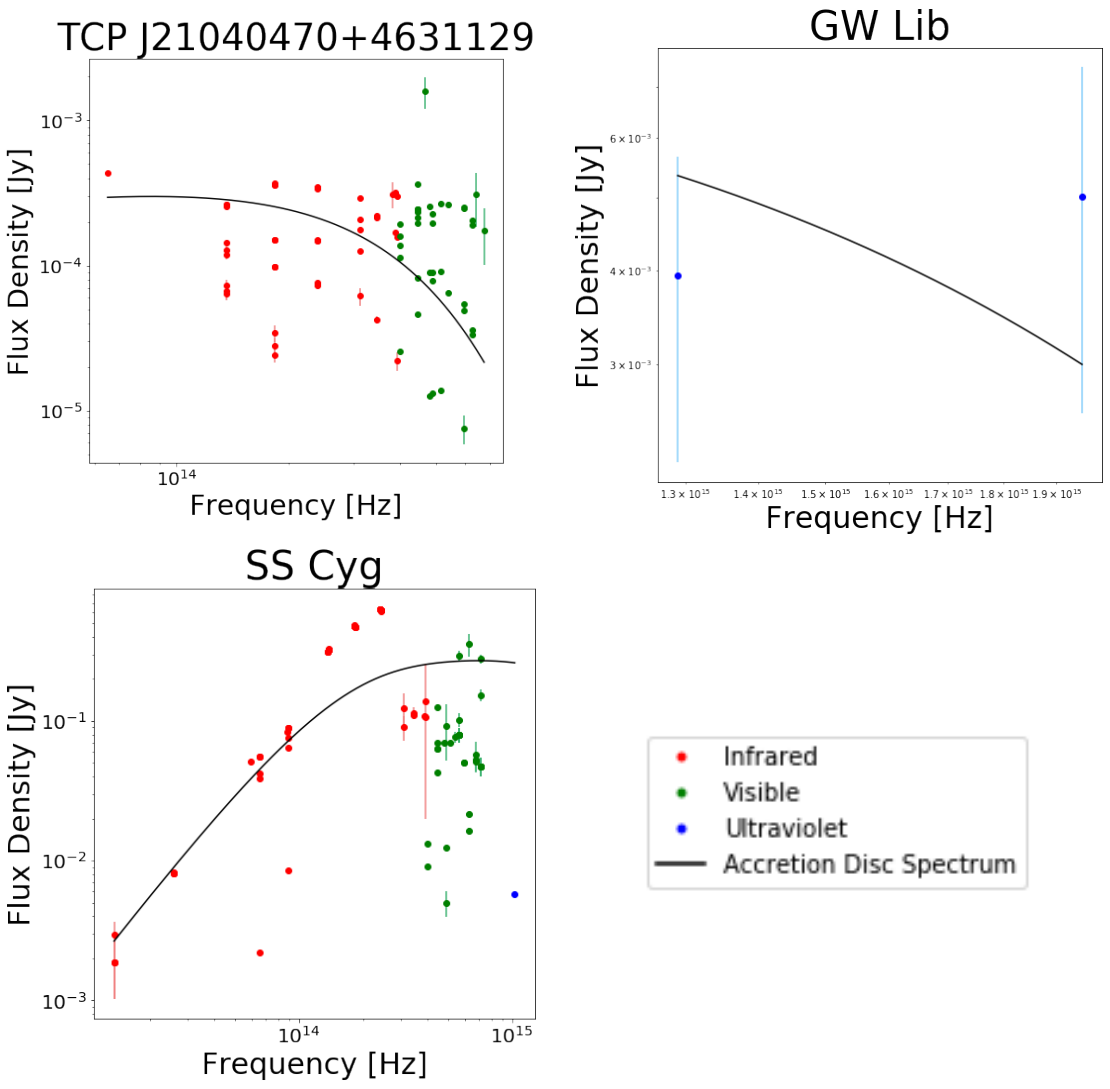

Figure 60: The spectral energy distributions of the Pala et al. (2020) volume-limited sample, overplotted with the best-fit model spectra.

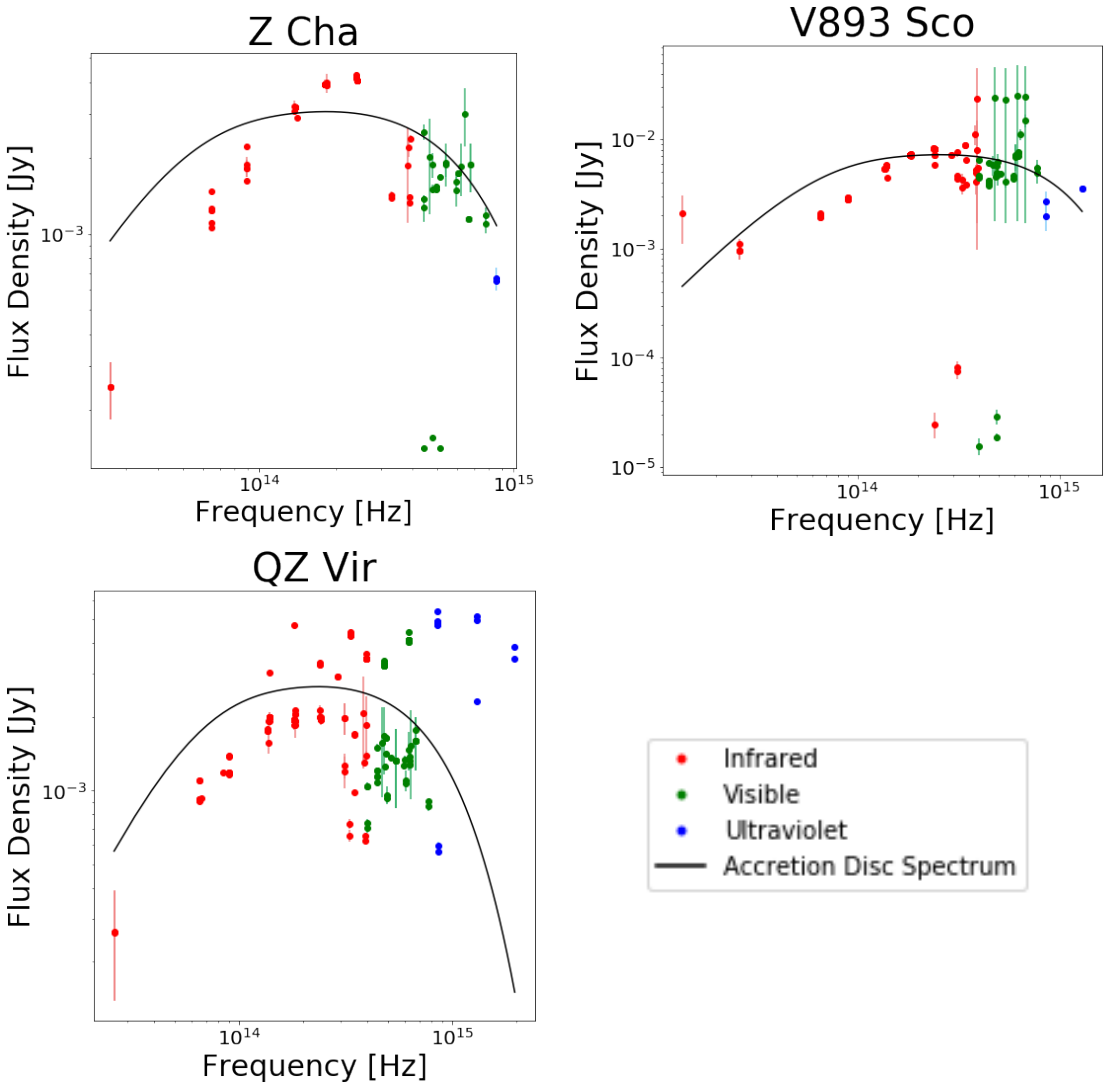

Figure 60: The spectral energy distributions of the Pala et al. (2020) volume-limited sample, overplotted with the best-fit model spectra.

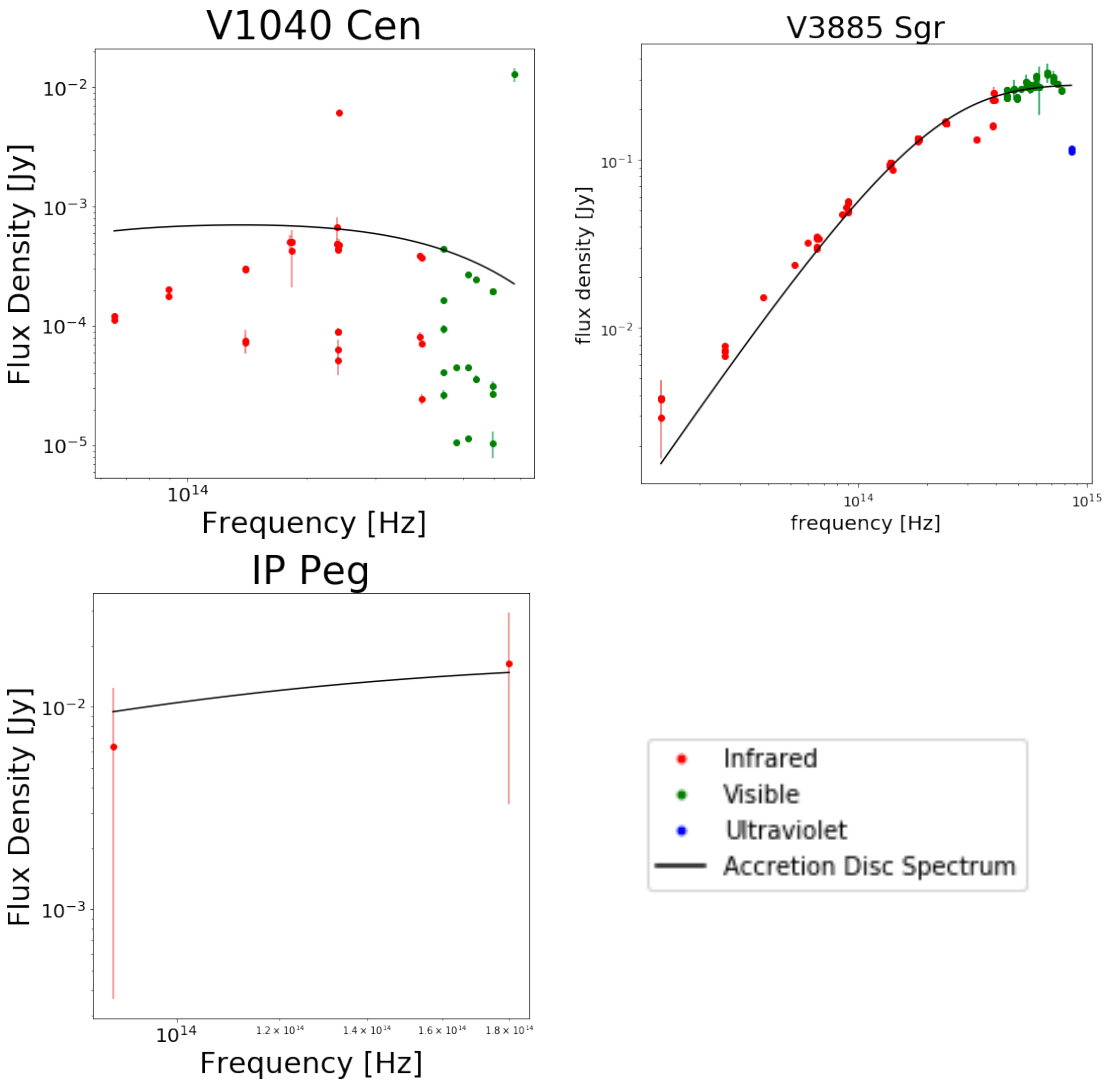

Figure 60: The spectral energy distributions of the Pala et al. (2020) volume-limited sample, overplotted with the best-fit model spectra.

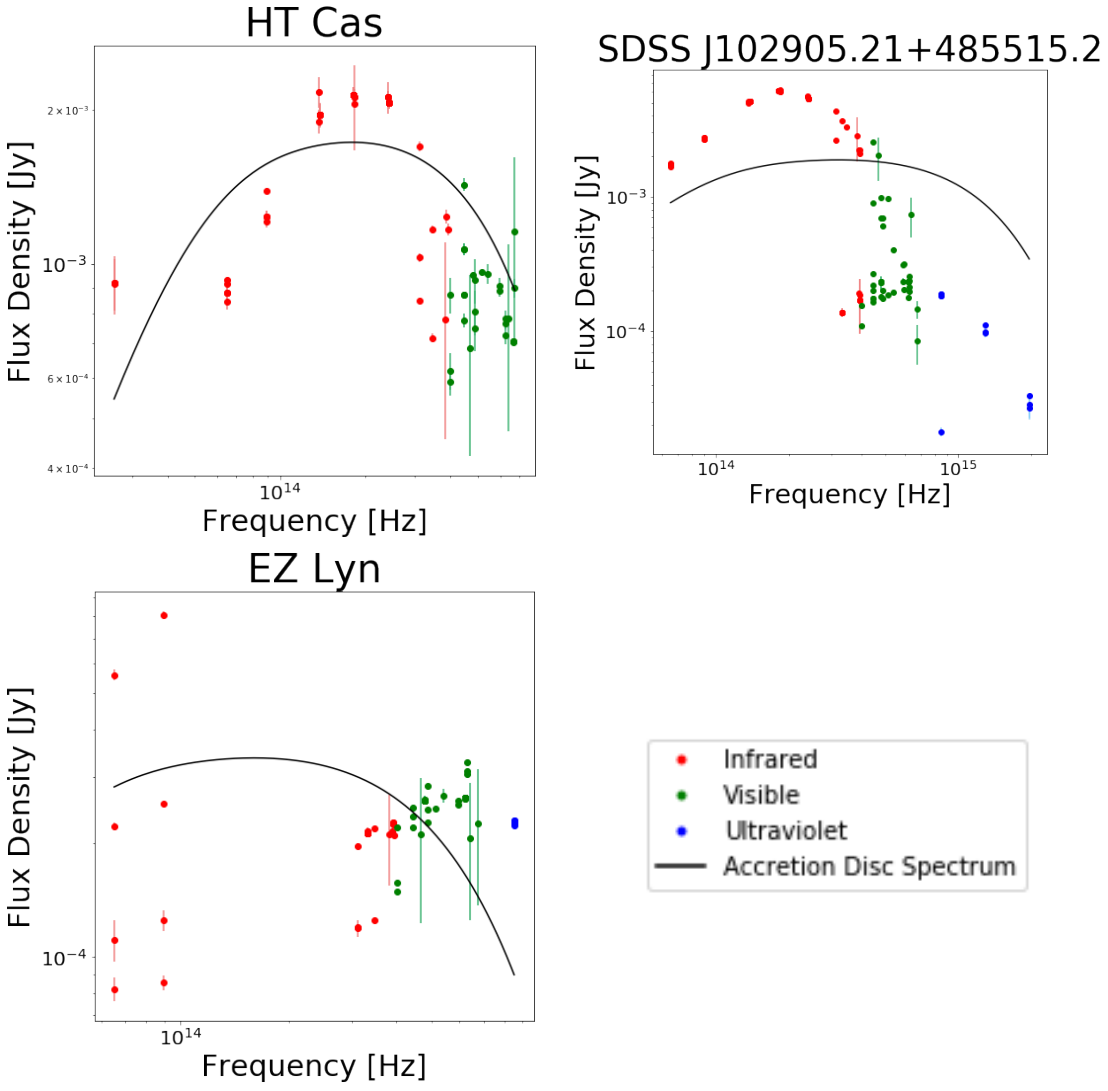

Figure 60: The spectral energy distributions of the Pala et al. (2020) volume-limited sample, overplotted with the best-fit model spectra.

Table 5: The portion of the Pala et al. (2020) volume-limited sample used in this study and their respective accretion rates as calculated using the *blackbody()* function.

Name	$\dot{M}$ [$M_\odot$ yr^{-1}] (Pala et al. (2020))	$\dot{M}$ [$M_\odot$ yr^{-1}] (this text)	χ^2_{red}
WZ Sge	$(7.4\pm1.3)\times10^{-11}$	$(1.55\pm0.48) \times 10^{-12}$	8192
VW Hyi	$(50\pm34)\times10^{-11}$	$(1.27\pm0.72) \times 10^{-11}$	61298
GD 552	$(2.9\pm1.9)\times10^{-11}$	$(3.38\pm0.22) \times 10^{-13}$	180980
ASASSN-14dx		$(4.73\pm0.52) \times 10^{-13}$	3434
IX Vel		$(2.05\pm0.05) \times 10^{-09}$	2218
OY Car	$(8\pm5)\times10^{-11}$	$(1.00\pm0.03) \times 10^{-11}$	1431
U Gem	$(31\pm6)\times10^{-11}$	$(3.02\pm0.21) \times 10^{-11}$	2216610
BW Scl	$(10\pm7)\times10^{-11}$	$(8.37\pm0.58) \times 10^{-12}$	30316
V627 Peg	$(13\pm9)\times10^{-11}$	$(7.50\pm0.23) \times 10^{-11}$	0.001
TCP J21040470+4631129		$(1.16\pm0.17) \times 10^{-13}$	5231
GW Lib	$(13\pm3)\times10^{-11}$	$(9.48\pm3.60) \times 10^{-11}$	1.354
SS Cyg		$(6.06\pm1.04) \times 10^{-10}$	6917585
Z Cha	$(10\pm3)\times10^{-11}$	$(3.00\pm0.14) \times 10^{-12}$	162766
V893 Sco		$(9.57\pm0.72) \times 10^{-12}$	225577
QZ Vir		$(7.48\pm0.45) \times 10^{-12}$	4671
V1040 Cen		$(4.87\pm3.16) \times 10^{-12}$	369155
V3885 Sgr		$(1.62\pm0.03) \times 10^{-09}$	119
IP Peg		$(4.12\pm1.30) \times 10^{-11}$	0.280
HT Cas	$(22\pm8)\times10^{-11}$	$(2.26\pm0.08) \times 10^{-12}$	768
SDSS J102905.21+485515.2		$(2.00\pm0.32) \times 10^{-11}$	402569
EZ Lyn	$(6\pm4)\times10^{-11}$	$(2.34\pm0.14) \times 10^{-12}$	2004

Many of these SEDs are sparse and/or very noisy, and the majority of the fits are very poor. I therefore do not pursue the idea of obtaining a volume limited set of mass transfer rates further.

6.2.2 Absolute Magnitude vs. Orbital Period

Although the SED fits were not a success, the Pala et al. (2020) sample can still provide an indication of whether the 16 systems in my sample are at all typical CVs, or whether (as one might suspect, given that they are amongst the brightest, best-known CVs) they are particularly luminous.

In figures 61 and 62 I plot the absolute magnitudes in the Gaia G-band against the orbital periods of the Pala et al. (2020) systems, as well as the systems in my sample.

One can clearly see the period gap in these plots, as well as a general positive correlation. This result is not unexpected, as long orbital periods indicate large orbital separations, massive stars, and larger accretion discs, and hence a system that is brighter in the optical.

The systems in my sample are mostly above the period gap, and on average brighter than the rest of the sample. This is because I selected well-studied systems, so as to have as much data to perform the fits on as possible. Because brighter objects are easier to study, and because the longer-period systems are generally brighter, the systems in my sample are therefore on average long period and bright. They are generally longer-period and brighter than the Pala et al. (2020) sample, and are likely not representative of the total population of cataclysmic variables. This is particularly significant for the DNe, which, in the Pala et al. (2020) sample, tend to be clustered in the bottom-left (faint, short orbital period) corner of the plot, but this cluster is not represented by any of the DNe in my sample.

6.3 Overview of Results

6.3.1 A Collection of SEDs

This is the biggest study of its kind to date, but not the only one. Hewitt (2020) constructed SEDs of a sample of 11 NLs. Castro Segura et al. (2021) constructed a detailed SED of the NL V341 Ara, and Dubus et al. (2007) constructed an SED of AE Aqr. Mine is a bigger sample than that of previous studies, and contains many types of CVs. This kind of study has previously been done for a smaller sample and/or a sample of just one type of CV. The broad SEDs of this, the largest sample of CVs for this kind of study to date, are given in figure 55. This is the central result of my work. This sample is not representative of the underlying CV population, it is a sample of particularly bright and long-period systems.

6.3.2 Estimates of $\dot{M}$

All CVs are variable. The data I have used are from many different epochs, and are sampled over a range of orbital phases and outburst cycles. Even NLs, that are constantly in outburst, have different brightnesses at different times due to flickering. This variability is expected to add significant noise to the data.

An attempt was made to use stellar spectral flux data from Pickles (1998) to represent the spectra of the secondaries. Unfortunately, while this may have been more accurate than modelling them as simple blackbodies, I found that the Pickles (1998) spectra were not sufficiently broad-spectrum for the purposes of this study of broad spectral energy distributions.

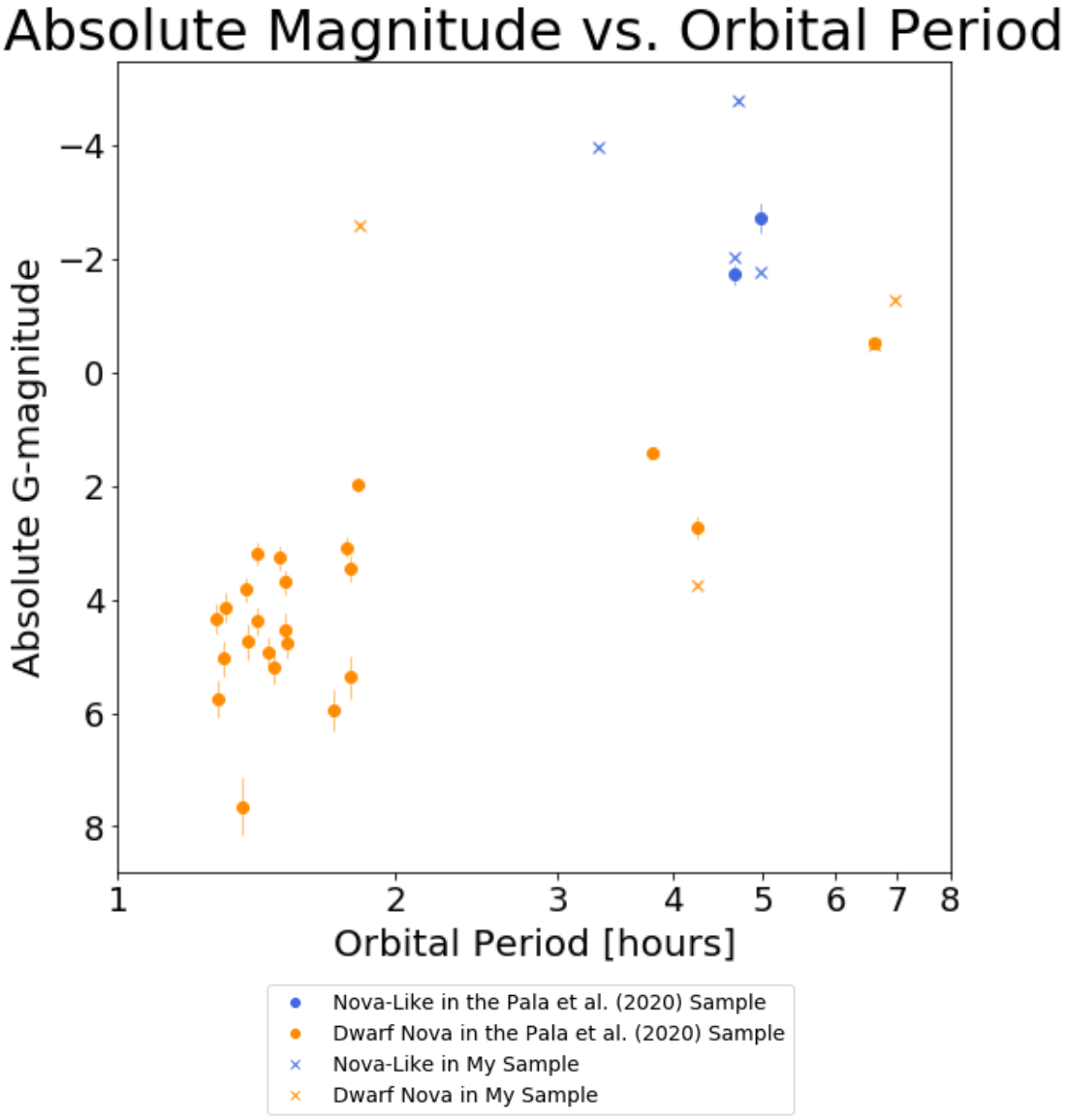

Figure 61: Absolute magnitudes in the G-band vs. orbital period for the non-magnetic systems in the Pala et al. (2020) volume-limited sample in my sample.

While the contributions of the stellar components have been subtracted from the data in order to estimate the spectrum of the accretion disc and the accretion rate, the contribution of the bright spot has not been considered. This contribution may depend on its size and temperature, as well as the orientation of the system, among other factors. The contribution of the bright spot may be significant, and will be more important during quiescence, as it may be outshone by the disc during

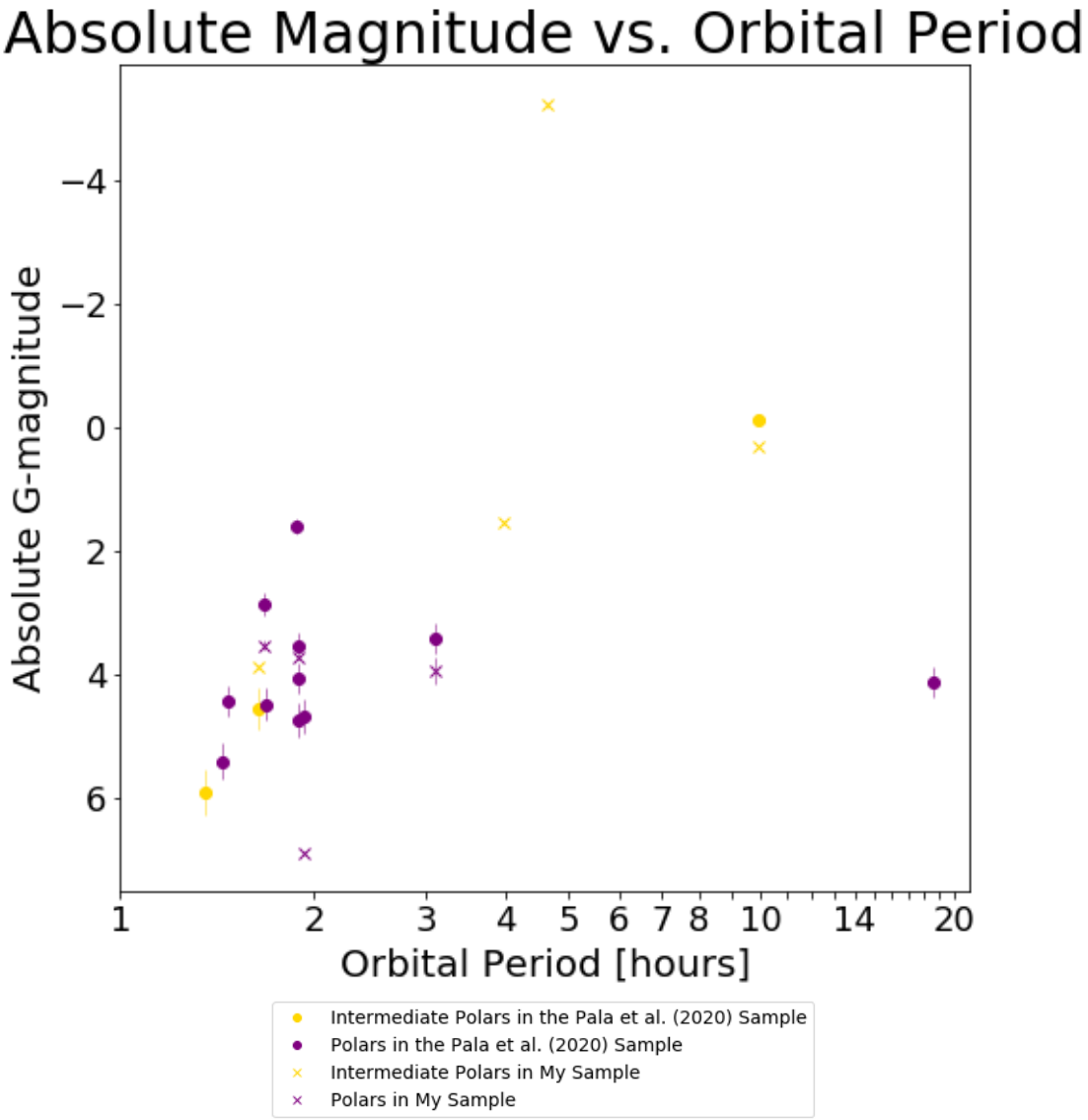

Figure 62: Absolute magnitudes in the G-band vs. orbital period for the magnetic systems in the Pala et al. (2020) volume-limited sample in my sample.

outburst. Due to the lack of theoretical treatment of the bright spot, it was not clear how its contribution could be calculated in order for it to be subtracted from the data. Because of the lack of theoretical treatment, it would be necessary to provide an ad hoc consideration of the bright spot Frank et al. (2002). Given the variability of the bright spot it would be a particularly difficult task to do so with any reasonable degree of accuracy, especially considering these SEDs are constructed from data over a wide time period and from all points in the outburst and eclipse

cycles. Such consideration is therefore outside of the scope of this work, and it remains the task of subsequent research to consider the contribution of the bright spot to the spectral energy distributions of cataclysmic variables.

From the discussion on page 105, the choice to include/exclude data points from the fits is in some cases somewhat subjective. Also, I did not apply any extinction corrections for the optical/IR data, though this is a small detail as these are nearby objects.

The fits for the DNe were largely not successful. This is not too surprising, as the sum of blackbodies is a good model for high-$\dot{M}$, steady state discs. However, for a DN in quiescence the disc emission is much harder to model (Tylenda, 1981).

6.3.3 The Radio to Optical Flux Ratios of Polars

I have demonstrated that polar CVs are radio bright in comparison to non-magnetic CVs. This result is not entirely unexpected, as several polars were detected in the radio decades ago, whereas reliable detections of non-magnetic CVs are more recent, and require more sensitive facilities. However, this result has not been explicitly demonstrated before.

7 Conclusions

In this work, I compiled a set of multi-wavelength data for 16 nearby CVs representing the 4 main classes of CVs (DNe, NLs, IPs, and polars). This sample contains magnetic and non-magnetic systems, with orbital inclinations that range from very low to eclipsing systems. Most of the orbital period range in which CVs are usually found is sampled, and amongst the 4 DNe are systems with both low and high outburst duty cycles.

I constructed broad SEDs for these systems and discussed the extent of uniformity of SEDs in a particular class and difference between the SEDs of different classes. In aid of these comparisons, I calculated and plotted the flux density ratios between the different wavebands. In addition, I modelled the accretion discs of 8 well-studied non-magnetic cataclysmic variables as rings of blackbodies, in order to estimate mass accretion rates. I have also performed this fit on the Pala et al. (2020) volume-limited sample and estimated their accretion rates.

My conclusions are:

1. In all cases, it is clear that more than one spectral component is present in the SED of a CV. This implies that the light from these systems originate from more than one emission mechanism.

2. Nova-like and dwarf-novae systems tend to have clear blackbody-like spectra in the infrared to ultraviolet range.

3. IP and polar systems tend to have relatively flat spectra throughout the entire frequency domain. Some parts of the spectra of magnetic CVs may have a blackbody-like shape that is likely evidence of the stellar components.

4. Contributions in the radio, possibly from jets, and in the X-ray, from the boundary layer for NLs and DNe and the accretion column for IPs and polars, are clearly visible in their spectra, and are clearly not part of the (typically blackbody) spectrum that is seen in the IR to UV wavelength range.

5. Because of the contributions of the stellar components, the spectra of some CVs are bimodal.

6. For the most part, the most successful accretion disc fits are those of nova-likes, with their bright, steady-state discs (with the exception of IX Vel). The data for the dwarf novae are a mix of both quiescent and outburst states, and the fits are therefore not as good.

7. The formal errors on mass transfer rate, from the fitting routine used here, are clearly significant underestimates of the uncertainty. Furthermore, the good-

ness of fit parameters calculated indicate that the fits do not properly capture the data. It is therefore not surprising that many of my accretion rate estimates are inconsistent with estimates in the literature. However, investigating plausible ranges in $\dot{M}$ show that about half of the estimates are good to within about a factor of 5.

8. The attempt to apply this method to the Pala et al. (2020) sample resulted mostly in very poor fits. First, for several of those systems, no suitable data are publicly available. Furthermore, the method cannot be applied to a small amount of data quickly and simply. It must be performed on as large a dataset as possible, and other contributions to the spectrum must be accounted for. This illustrates that, while mass accretion rates for a volume-limited sample of non-magnetic CVs would be of great value, measurements for that sample will require significant observational and modelling effort.

9. As has been noted in the past, shorter-period systems have higher X-ray to optical ratios than longer-period systems, and magnetic systems have larger X-ray to optical flux ratios than non-magnetic systems.

10. Investigating flux ratios reveals that polars tend to be radio bright compared to non-magnetic CVs.

Bibliography

Adams F.C. et al., 2004, Red Dwarfs and the End of the Main Sequence, University of Michigan, Ann Arbor, MI 48109, USA, RevMexAA (Serie de Conferencias), vol. 22, p. 46–49

Agrawal P.C., et al., 1981, H0139-68, International Astronomical Union Circulars, vol. 2, p. 3649

Agrawal P.C., Riegler G.R., Rao A.R., 1983, A New AM Her-Like X-ray Source, Nature, vol. 301, p. 318-321

Andrades A.G., 2017, Aplicaciónes de la Rediacion Cherenkov, Departamento de Electrónica y Electromagnetismo, Facultad de Física, Universidad de Sevilla

Andrae R., Schulze-Hartung T. Melchior P., Dos and Don'ts of Reduced Chi-Squared, arXiv e-prints, p. arXiv:1012.3754

Andronov I.L., et al., 2008, Multiple Timescales in Cataclysmic Binaries. The low-field magnetic dwarf nova DO Draconis, Astronomy and Astrophysics, vol. 486, p. 855-865

Arenas J., et al., 2000, A spectroscopic Study of V603 Aquilae: Stellar parameters and Continuum-Line Variations, Monthly Notices of the Royal Astronomical Society, vol. 311, p. 135-148

Armijo M.M., 2012, Review: Accretion Disk Theory, Departamento de Astronomía y Astrofísica, Pontificia Universidad Católica de Chile, Santiago de Chile

Arnaboldi M.A., 2010, The Wide-Field Imaging with VISTA and the ESO Public Surveys, Proceedings of Science

Aschenbach B., et al., 1981, The ROSAT Mission, Sustainable Science and Resources, vol. 30, p. 569-573

Aschenbach B., et al., 1989, The XMM X-ray Telescopes, Astronomische Gesellschaft Abstract Series, p. 7

Bailer-Jones C.A.L., 2018, Estimating Distance from Parallaxes. IV. Distances to 1.33 Billion Stars in Gaia Data Release 2, Astronomical Journal, vol. 156, p. 58

Bailey J., 1981, The Distances of Cataclysmic Variables, Monthly Notices of the Royal Astronomical Society, vol. 197, p. 31-39

Balman S., 2012, The X-ray Properties of Cataclysmic Variables, Memorie della Società Astronomica Italiana, vol. 83, p. 585

Baptista R., et al., 1995, Hubble Space Telescope and R-Band Eclipse Maps of the UX Ursae Majoris Accretion Disk, Astrophysical Journal, vol. 448, p. 395

Barrett P.E., et al., 2017, A Jansky VLA Survey of Magnetic Cataclysmic Variable Stars: I. The Data, United States Naval Observatory

Barrett P.E., et al., 2020, Radio Observations of Magnetic Cataclysmic Variables, George Washington University

Bastian T.S., 1987, Aperture Synthesis Observations of Solar and Stellar Radio Emission, Ph.D. Thesis, University of Colorado, Boulder

Bersier D., 2016, The All-Sky Automated Survey for Supernavae, Revista Mexicana de Astronomia y Astrofisica Conference Series, vol. 48, p. 78-82

Beuermann K., Schwope A., Weissieker H., Motch C., 1985, EXOSAT / Optical Observations of the Am-Herculis Star H0139-68, Space Science Reviews, vol. 40, p. 135-138

Beuermann K., Thomas H.C., 1993, The ROSAT View of the Cataclysmic Variable Sky, Advances in Space Research, vol. 13, p. 115-124

Beuermann K., 2000, Secondary Stars in CVs - the Observational Picture, New Astronomy Review, vol. 44, p. 93-98

Beuermann K., et al. 2003, A Precise HST Parallax of the Cataclysmic Variable EX Hydrae, its System parameters, and Accretion Rate, Astronomy and Astrophysics, vol. 412, p. 821-827

Beuermann K., Reinsch K., 2008, High-Resolution Spectroscopy of the Intermediate Polar EX Hydrae. I. Kinematic Study and Roche Tomography, Astronomy and Astrophysics, vol. 480, p. 199-212

Bevington P., Robinson D.K., 2003, Data Reduction and Error Analysis for the Physical Sciences, 3rd edition

Bianchi L., et al., 1997, The Galaxy Evolution Explorer, American Astronomical Society Meeting Abstracts, vol. 190, p. 09.09

Bitner M.A., Robinson E.L., Behr B.B., 2007, The Masses and Evolutionary State of the Stars in the Dwarf Nova SS Cygni, Astrophysical Journal, vol. 662, p. 564-573

de Blok E., Booth R., Frank B., 2009, HI Science with MeerKAT, Panoramic Radio Astronomy: Wide-field 1-2 GHz Research on Galaxy Evolution, p. 7

Bode M.F., Evans A., Bruch A., 1982, Did SU UMa Undergo a Classical Nova Outburst, IAU Colloq. 69: Binary and Multiple Stars as Tracers of Stellar Evolution, vol. 98, p. 475-481

Bond H.E., 1978, CD -42 14462: A Dwarf Nova in Permanent Outburst, Publications of the Astronomical Society of the Pacific, vol. 90, p. 216-218

Boothe R.S., et al., 2009, An open invitation to the Astronomical Community to propose Key Project Science with the South African Square Kilometer Array Precursor MeerKAT, SKA South African Square Kilometer Array

Bornak J., McNamara B., Harrison T., 2008, Quantifying the Variabilities and Periodicities of Synchrotron Jets in X- Ray Binaries, National Optical Astronomy Observatory Proposal, p. 332

Bowyer S., 1982, The Extreme Ultraviolet Explorer, Advances in Space Research, vol. 2, p. 157-165

Bowyer S., Hurwitz M., 1990, ORFEUS-SPAS - The Berkeley EUV Spectrometer, Observatories in Earth Orbit and Beyond, p. 475-480

Bowyer S., 1996, Highlights of recent results from the Extreme Ultraviolet Explorer, Memorie della Societa Astronomica Italiana, vol. 67, p. 113-120

Brown A.G.A., 2013, GAIA, Counting Down to Launch, Société Francaise d'Astronomie et d'Astrophysique

Bruch A., 1991, Multicolour photometry of the unusual cataclysmic variable AE Aquarii, Astronomy and Astrophysics, vol. 251, p. 59

Burgarella D., Martin C., Schiminovich D., 2003, GALEX, the Galaxy Evolution Explorer: a 28-months UV mission, Semaine de l'Astrophysique Francaise, p. 239

Burton W.B., 1974, Remarks on the Very Large Array (VLA) radio telescope project, Journal of The Franklin Institute, vol. 298, p. 299-306

Campbell L., 1935, Harvard College Observatory Bulletin, 898, 20

Campbell R.K., Harrison T.E., Kafka S., 2008, Cyclotron Modeling Phase-Resolved Infrared Spectroscopy of Polars. III. AM Herculis and ST Leo Minoris, Astrophysical Journal, vol. 683, p. 409-423

Canuto V.M., Goldman I., Hubickyj O., 1984, A Formula for the Shakura-Sunyaev Turbulent Viscosity parameter, The Astrophysical Journal, vol. 280, p. L55-L58

Cash W., 1984, The Far Ultraviolet Spectroscopic Explorer, Journal of the British Interplanetary Society, vol. 37, p. 81-85

Castro Segura N., et al., 2021, Bow Shocks, Nova Shells, Disc Winds and Tilted Discs: The Nova-Like V341 Ara has it All, Monthly Notices of the Royal Astronomical Society, vol. 501, p. 1951-1969

Chambers K.C., 2004, Pan-STARRS Telescope No. 1, American Astronomical Society Meeting Abstracts, vol. 204, p. 97.02

Christy C.T., et al. 2022, The ASAS-SN Catalog of Variable Stars X: Discovery of 116,000 New Variable Stars Using g-band Photometry, arXiv e-prints, p. arXiv:2205.02239

Code A.D., 1949, The Effect of Electron Scattering in Stellar Atmospheres, Astronomical Journal, vol. 54, p. 124-125

Code A.D., 1991, Observations with the Wisconsin Ultraviolet Photopolarimetry Experiment (WUPPE), Bulletin of the American Astronomical Society, vol. 23, p. 971

Conrad S.J., et al., 2000, The Far Ultraviolet Spectroscopic Explorer Optical System: Lessons Learned, Barbara A. Mikulski Archive for Space Telescopes, vol. 4139, p. 186

Coppejans D.L., et al., 2015, Novalike Cataclysmic Variables are Significant Radio Emitters, Monthly Notices of the Royal Astronomical Society, vol. 451, p. 3801-3813

Coppejans D.L., et al., 2016, Statistical Properties of Dwarf Novae-type Cataclysmic Variables: The Outburst Catalogue, Monthly Notices of the Royal Astronomical Society, vol. 456, p. 4441-4454

Coppejans D.L., et al., 2016, Dwarf Nova-Type Cataclysmic Variable Stars are Significant Radio Emitters, Monthly Notices of the Royal Astronomical Society, vol. 463, p. 2229-2241

Coppejans D.L., Knigge C., 2020, The Case for Jets in Cataclysmic Variables, New Astronomy Review, vol. 89, p. 101540

Cowley A.P., Crampton D., Hesser J.E., 1977, The Flickering White Dwarf CD -42 14462: A Noneruptive Close Binary, Astrophysical Journal, vol. 214, p. 471-477

Cutri R. M., et al. 2003, VizieR Online Data Catalog: 2MASS All-Sky Catalog of Point Sources, VizieR Online Data Catalog

Dai Z., Qian S., 2009, Orbital Period Analysis of Eclipsing Dwarf Novae: U Geminorum, Astrophysics and Space Science, vol. 321, p. 91-100

Dai Z.B., Qian S.B., 2009, Plausible explanations for the variations of orbital period in the old nova DQ Herculis, Astronomy and Astrophysics, vol. 503, p. 883-888

Davidsen A.F., et al., 1981, The Johns Hopkins Ultraviolet Telescope for Shuttle Astronomy, Shuttle Pointing of Electro-Optical Experiments, Society of Photo-Optical Instrumentation Engineers (SPIE) Conference Series, vol. 265, p. 375-380

Davidsen A.F., Fountain G.H., 1985, The Hopkins Ultraviolet Telescope, Johns Hopkins APL Technical Digest, vol. 6, p. 28-37

Davidsen A.F., 1990, The Hopkins Ultraviolet Telescope, Observatories in Earth Orbit and Beyond, vol. 166, p. 292

de Miguel E, et al., 2016, Accretion-Disc Precession in UX Ursae Majoris, Monthly Notices of the Royal Astronomical Society, vol. 457, p. 1447-1455

Dial O.L., Cooley J.L., 1977, Mission design implications of an inclined elliptical geosynchronous orbit (International Ultraviolet Explorer), Journal of Spacecraft and Rockets, vol. 14, p. 401-408

Ding J., 2020, A Brief Analysis of the Research Scheme of the Cyclotron Radiation from a Single Electron, Physics & Astronomy International Journal, vol. 4, p. 60-64

Dixon W, et al., 2002, Final Calibration of the Berkeley Extreme and Far-Ultraviolet Spectrometer on the ORFEUS-SPAS I and II Missions, Publications of the Astronomical Society of the Pacific, vol. 114, p. 112-124

Drechel H., Rahe J., Holm A., Krautter J., 1981, Phase-dependent optical and ultraviolet observations of the old nova V603 AQL (1918), Astronomy and Astrophysics, vol. 99, p. 166-172

Drew J.E., et al., 2005, The INT Photometric Hα Survey of the Northern Galactic Plane (IPHAS), Monthly Notices of the Royal Astronomical Society, vol. 362, p. 735-776

Drew J.E., et al., 2005, IPHAS: Surveying the North Galactic Plane in Hα, The Newsletter of the Isaac Newton Group of Telescopes, vol. 9, p. 3-7

Dubus G., et al., 2007, Spitzer Space Telescope Observations of the Magnetic Cataclysmic Variable AE Aquarii, Astrophysical Journal, vol. 663, p. 516-521

Duval V.G., et al., 2004, The Wide-Field Infrared Survey Explorer (WISE), Optical, Infrared, and Millimeter Space Telescopes p.101-111

Eberhard H., Werner N., 2004, The Elementary Process of Bremsstrahlung

Echevarría J., et al., 2008, High-Dispersion Absorption-Line Spectroscopy of AE Aqr, Monthly Notices of the Royal Astronomical Society, vol. 387, p. 1563-1574

Eisenbart S., et al., 2002, Multi-Wavelength Spectrophotometry of EX Hydrae, Astronomy and Astrophysics, vol. 382, p. 984-998

European Space Agency, 1997, VizieR Online Data Catalog: The Hipparcos and Tycho Catalogues, VizieR Online Data Catalog

Feast M.W., Glass I.S., 1974, Infra-red photometry of some old novae, Monthly Notices of the Royal Astronomical Society, vol. 167, p. 81-85

Fender R., et al., 2016, ThunderKAT: The MeerKAT Large Survey Project for Image-Plane Radio Transients, Proceedings of Science, MeerKAT Science: On the Pathway to the SKA, p. 13

Frank J., King A., Raine D. J., 2002, Accretion Power in Astrophysics, 3rd edition

Frater R.H., 1984, The Australia telescope - the radio astronomer's highwaz to the future, Publications of the Astronomical Society of Australia, vol. 5, p. 440-445

Friedjung M., 1997, The Characteristics of the Cool Component of the Cataclysmic Binary AE Aquarii Derived from its HIPPARCOS Parallax, New Astronomy, vol. 2, p. 319-322

Froning C.S., 1999, The Near-Infrared Properties of Compact Binary Systems, Ph.D. Thesis, University of Texas, Austin

Gänsicke B.T., Long K.S., Barstow M.A., Hubney I., 2006, FUSE and HST STIS Far-Ultraviolet Observations of AM Herculis in an Extended Low State, Astrophysical Journal, vol. 639, p. 1039-1052

Gänsicke B.T., et al., 2001, Phase-resolved Hubble Space Telescope/STIS Spectroscopy of the Exposed White Dwarf in the High-Field Polar AR Ursae Majoris, Astrophysical Journal, vol. 555, p. 380-392

Garrison R.F., et al., 1982, CPD-48° 1577: The Brightest Known Cataclysmic Variable, Bulletin of the American Astronomical Society, vol. 14, p. 978

Garrison R.F., et al., 1984, CPD -48 1577 : The Brightest Known Cataclysmic Variable, Astrophysical Journal, Letters, vol. 276, p. L13-L16

Gehrels N., 1999, Swift - Phase A Study of a Gamma Ray Burst MIDEX Mission, American Astronomical Society Meeting Abstracts, vol. 194, p. 97.03

Gehrels N., et al., 2004, The Swift Gamma-Ray Burst Mission, American Astronomical Society Meeting Abstracts, American Astronomical Society Meeting Abstracts, vol. 205, p. 116.01

Georgantopoulos I., et al., 1991, A Deep ROSAT Survey, The Space Distribution of Quasars, Astronomical Society of the Pacific Conference Series, vol. 21, p.6

Green R.F., et al., 1982, Cataclysmic variable candidates from the Palomar Green Survey, Publications of the Astronomical Society of the Pacific, vol. 94, p. 560-564

Grewling M., 2002, VizieR Online Data Catalog: Tubingen Ultraviolet Echelle Spectrometer (TUES, 1993-1996), VizieR Online Data Catalog

Gunn J.E., Weinberg D.H., 1995, The Sloan Digital Sky Survey, Wide Field Spectroscopy and the Distant Universe, p. 3

Haefner R., Metz K., 1984, The Old Nova V603 AQL : An Intermediate Polar?, Astronomy and Astrophysics, vol. 145, p. 311-320

Hall P.J., 1996, Phase Correction Strategies for the Australia Telescope Compact Array at Short Wavelengths, Science with Large Millimeter Arrays, p. 375-379

Hartley L.E., et al., 2002, Testing the line-driven disc wind model: time-resolved ultraviolet spectroscopy of IX Vel and V3885Sgr, Monthly Notices of the Royal Astronomical Society, vol. 332, p. 127-143

Hartley L.E., et al. 2005, The Far-Ultraviolet Spectrum of Z Camelopardalis in Quiescence and Standstill, Astrophysical Journal, vol. 623, p. 425-441

Harrison T.E., Campbell R.K., 2015, The WISE lightcurves of Polars, Astrophysical Journal, Supplement, vol. 219, p. 32

Hessman F.V., et al., 1984, Time-Resolved Spectroscopy of SS Cygni at Minimum and Mmaximum Light, Astrophysical Journal, vol. 286, p. 747-759

Haswell C.A., et al., 1997, Pulsations and Accretion Geometry in YY Draconis: A Study Based on Hubble Space Telescope Observations, Astrophysical Journal, vol. 476, p. 847-864

Hayashi S.S., et al., 1992, Performance of SUBARU telescope in 0.3-30 micron, Publications of the National Astronomical Observatory of Japan, vol. 2, p. 547-550

Hecht E., 1987, Optics, 2nd edition

Heeschen D.S., 1967, Radio Astronomy: A Large Antenna Array, Science, vol. 158, p. 75-78

Heeschen D.S. 1975, The Very Large Array, Sky and Telescope, vol. 49, p. 344

Heise J., Verbunt F., 1988, Ultraviolet observations of AM Her, Astronomy and Astrophysics, vol. 189, p. 112-118

Hellier C., 2007, Cataclysmic variable Stars: How and Why they Vary, Springer-Praxis Books in Astronomy and Space Science, Praxis Publishing, Chichester, UK

Hewitt D., 2020, A MeerKAT Survey of Nearby Novalike Cataclysmic Variables, South African Astronomical Observatory

Hoard D.W., 2005, Spin-resolved Far-Ultraviolet Observations of the Magnetic White Dwarf in YY Draconis, Astrophysical Journal, vol. 130, p. 214-223

Hodapp K.W., et al. 2004, Design of the Pan-STARRS Telescopes, Astronomische Nachrichten, vol. 325, p. 636-642

Hodapp et al., 2004, Optical Design of the Pan-STARRS Telescopes, Ground-based Telescopes, Society of Photo-Optical Instrumentation Engineers (SPIE) Conference Series, vol. 5489, p. 667-678

Hoffman N.M., 1974, Coronas with Bremsstrahlung Cooling, Ph.D. Thesis, Wisconsin University, Madison.

Horne K., Welsh W.F., Wade R.A., 1993, On the Mass of Nova DQ Herculis (1934), Astrophysical Journal, vol. 410, p. 357

Howell S.B., et al., 2006, Low-State Phase-Resolved Infrared Spectroscopy of VV Puppis, Astronomical Journal, vol. 131, p. 2216-2222

IUE Project Staff, Science Commissioning Team, 1978, Early Operations with the International Ultraviolet Explorer, Bulletin of the American Astronomical Society, vol. 10, p. 460

Iye M., Yamashita T., 2000, Overview of Subaru instrumentation, Optical and IR Telescope Instrumentation and Detectors, Society of Photo-Optical Instrumentation Engineers (SPIE) Conference Series, vol. 4008, p. 18-27

Jansen F.A., 1999, XMM: Advancing Science with the High-Throughput X-ray Spectroscopy Mission, European Space Agency Bulletin, vol. 100, p. 9-12

Jewitt D., 2003, Project Pan-STARRS and the Outer Solar System, Earth Moon and Planets, vol. 92, p. 465-476

Jenkins A.J., White H.E., 1957, Fundementals of Optics 3rd edition

Johnstone C.P., 2015, Stellar winds on the main-sequence. I. Wind model, Astronomy and Astrophysics, vol. 577, p. A27

Joy A.H., 1954, Spectroscopic Observations of AE Aquarii, Astrophysical Journal, vol. 120, p. 377

Joy A.H., 1956, Radial-Velocity Measures of SS Cygni at Minimum Light, Astrophysical Journal, vol. 124, p. 317

Kafka S., et al., 2010, Low-state Magnetic Structures in Polars: Nature or Nurture?, Astrophysical Journal, vol. 721, p. 1714-1724

Kalomeni B., Pekünlü E.R., Yakut K., Cyclotron emission from accretion plasma columns in magnetic cataclysmic variable stars, Astronomy and Astrophysics, vol. 439, p. 823-833

Kaiser N., 2005, The Pan-STARRS Large Survey Telescope Project, American Astronomical Society Meeting Abstracts, vol. 206, p. 24.02

Kato T., 2021, Study of the Low-Amplitude Z Cam Star IX Vel, arXiv e-prints , p. arXiv:2111.15145

Keller S.C., et al., 2007, The SkyMapper Southern Sky Survey, The Future of Photometric, Spectrophotometric and Polarimetric Standardization, Astronomical Society of the Pacific Conference Series, vol. 364, p. 177-185

Keller S.C., et al., 2007, The SkyMapper Telescope and The Southern Sky Survey, Astronomical Society of Australia, vol. 24, p. 1-12

Kinch B.E. et al, 2020, Inverse Compton Cooling in the Coronae of Simulated Black Hole Accretion Flows, Astrophysical Journal, vol. 904, p. 117

Kitaguchi T., et al., 2014, NuSTAR and Swift Observations of the Fast Rotating Magnetized White Dwarf AE Aquarii, Astrophysical Journal, vol. 782, p. 3

Knigge et al., 1997, Disks, Winds, and Veiling Curtains: Dissecting the Ultraviolet Spectrum of the Dwarf Nova Z Camelopardalis in Outburst, Astrophysical Journal, vol. 476, p. 291-310

Knigge et al., 2000, A Self-occulting Accretion Disk in the SW Sextantis Star DW Ursae Majoris, Astrophysical Journal, Letters, vol. 539, p. L49-L53

Knigge C., 2006, Monthly Notices of the Royal Astronomical Society, 373, 484

Knigge C., 2011, The Donor Stars of Cataclysmic Variables, Monthly Notices of the Royal Astronomical Society, vol. 375, p. 484-502

Knigge C., Baraffe I., Patterson J., 2011, The Evolution of Cataclysmic Variables as Revealed by Their Donor Stars, Astrophysical Journal, Supplement, vol. 194, p. 28

Koch-Miramond L., 1985, XMM: The X-ray Multiple Mirror Observatory, Non-thermal and Very High Temperature Phenomena in X-ray Astronomy, p. 291

Kraft R.P., 1959, The Binary System Nova DQ Herculis. II. an Interpretation of the Spectrum during the Eclipse Cycle, Astrophysical Journal, vol. 130, p. 110

Krimm H.A., et al., 2004, The Swift γ-ray Burst MIDEX Mission, New Astronomy Review, vol. 48, p. 551-557

Kruszewski A., et al., 1982, Variability of Soft X-ray Emission of EX Hydrae Observed with Einstein Observatory, IAU Colloq. 69: Binary and Multiple Stars as Tracers of Stellar Evolution, Astrophysics and Space Science Library, vol. 98, p. 457-466

Kubiak M., Pojmanski G., Krzeminski W., 1999, Spectroscopic Observations of IX Vel, Acta Astronomica, vol. 49, p. 73-84

Lawrence A., et al., 2007, The UKIRT Infrared Deep Sky Survey (UKIDSS), Monthly Notices of the Royal Astronomical Society, vol. 379, p. 1599-1617

Lawrence A., 2013, The UKIRT Infrared Deep Sky Survey (UKIDSS): Origins and Highlights, Thirty Years of Astronomical Discovery with UKIRT, Astrophysics and Space Science Proceedings, vol. 37, p. 271

Lesniak M.V., Sion E.M., 2003, The Accretion Rate and Temperature of the Accreting White dwarf in the Dwarf Nova SS Cygni During Quiescence, American Astronomical Society Meeting Abstracts, vol. 203, p. 44.12

Lindegren L., Söderhjelm S., 1982, The Astrometric Satellite HIPPARCOS - A Status Report, Reports of the Lund Observatory, vol. 18, p. 74-75

Linnell A.P., et al., 2007, A Synthetic Spectrum and Light-Curve Analysis of the Cataclysmic Variable IX Velorum, Astrophysical Journal, vol. 662, p. 1204-1219

Linnell A.P., et al., 2008, Modeling UX Ursae Majoris: An Abundance of Challenges, Astrophysical Journal, vol. 688, p. 568-582

Linnell A.P., et al., 2009, V3885 Sagittarius: A Comparison with a Range of Standard Model Accretion Disks, Astrophysical Journal, vol. 703, p. 1839-1850

Long K.S., Brammer G., Froning C.S., 2006, FUSE Spectroscopy of the White Dwarf in U Geminorum, Astrophysical Journal, vol. 648, p. 541-558

Longair M.S., 2011, High Energy Astrophysics

Loveday J., 1999, The Sloan Digital Sky Survey and Dark Matter, Dark matter in Astrophysics and Particle Physics, p. 305-314

Macchetto F., 1976, The International Ultraviolet Explorer (IUE), Memorie della Societa Astronomica Italiana, vol. 47, p. 431

Malina R.F., et al., 1982, The Extreme Ultraviolet Explorer, Optical Engineering, vol. 21, p. 764-768

Manchester R.N., 1991, The Australia Telescope, Advances in Space Research, vol. 11, p. 403-406

Margon B., 1999, The Sloan Digital Sky Survey, Philosophical Transactions of the Royal Society of London Series A, vol. 357, p. 93-103

Marshall F.E., 2003, Swift Science Analysis Tools, American Astronomical Society Meeting Abstracts, vol. 202, p. 48.07

Mason E., et al., 2008, VV Puppis in a Low State: Secondary-Star Irradiation or Stellar Activity?, Astronomy and Astrophysics, vol. 490, p. 279-286

Masters A.R., et al., 1977, Cyclotron Emission from Accreting Magnetic White Dwarfs, Monthly Notices of the Royal Astronomical Society, vol. 178, p. 501-504

Mateo M., Szkody P., Garnavich P., 1991, Near-Infrared Time-resolved Spectroscopy of the Cataclysmic Variable YY Draconis, Astrophysical Journal, vol. 370, p. 370

Mattei J.A., et al. 1996, Z Camelopardalis lightcurves 1927 - 1995, AAVSO Monogr, vol. 6

Mehlin T.G., 1959, Astronomy, New York John Wiley and Sons, inc.

Mereghetti S., et al., 2021, New X-ray Observations of the Hot Subdwarf Binary HD 49798/RX J0648.0-4418, Monthly Notices of the Royal Astronomical Society, vol. 504, p. 920-925

Millard B., et al., 2001, The Galaxy Evolution Explorer (GALEX), Mining the Sky, p. 201

Miller K., et al., 2020, Spitzer Final Voyage VR: A new Interactive Experience to Explore Spitzer's Observational Achievements, American Astronomical Society Meeting Abstracts, vol. 235, p. 211.04

Miller-Jones J.C.A., 2013, An Accurate Geometric Distance to the Compact Binary SS Cygni Vindicates Accretion Disc Theory, Science, vol. 340, p. 950-952

Morris S.L., 1999, The Limits of Inclination for Binary Star Partial Eclipses, Astrophysical Journal, vol. 520, p. 797-804

Moos H.W., McCandliss, S.R., Kruk J.W., 2004, FUSE: Lessons Learned for Future FUV Missions, UV and Gamma-Ray Space Telescope Systems, vol. 5488, p. 1-'12

Moos H.W., Sonneborn G., 2006, A Brief History of the FUSE Mission, Astrophysics in the Far Ultraviolet: Five Years of Discovery with FUSE, Astronomical Society of the Pacific Conference Series, vol. 348, p. 4

Mukai K., et al., 2002, Chandra Observations of Old Novae, Classical Nova Explosions, American Institute of Physics Conference Series, vol. 372-376, p. 372-376

Mukai K., Orio M., 2005, X-ray Observations of the Bright Old Nova V603 Aquilae, Astrophysical Journal, vol. 622, p. 602-612

Nauenberg M., 1972, Analytic Approximations to the Mass-Radius Relation and Energy of Zero-Temperature Stars, Astrophysical Journal, vol. 417, p. 417-430

Nava L., Nakar E., Piran T., 2016, Linear and Circular Polarization in Ultra-Relativistic Synchrotron Sources – Implications to GRB Afterglows, Monthly Notices of the Royal Astronomical Society, vol. 455, p. 1594–1606

Nordsieck K.H., et al., 1991, Overview of WUPPE Observations Obtained on the ASTRO-1 Mission, Bulletin of the American Astronomical Society, vol. 23, p. 842

Nordsiek K.H., et al. 1991, The Wisconsin Ultraviolet Photo-Polarimeter Experiment (WUPPE), Bulletin of the American Astronomical Society, vol. 23, p. 906

Nussbaumer H., 1982, On the Origin of Planetary Nebulae, Astronomy and Astrophysics, vol. 110, p. L1-L2

O'Connell R.F., 1973, Bremsstrahlung Model of Polarized Radiation from Magnetic White Dwarfs. Physics Letters A, vol. 46, p. 249-250

Oppenheimer B.D., Kenyon S.J., Mattei J.A., 1998, An Analysis of AAVSO Observations of Z Camelopardalis, Astronomical Journal, vol. 115, p. 1175-1189

Osaki Y., 1974, An Accretion Model for the Outbursts of U Geminorum Stars, Publications of the Astronomical Society of Japan, vol. 26, p. 429

Pala A.F., et al., 2020, A Volume-limited Sample of Cataclysmic Variables from Gaia DR2: Space Density and Population Properties, Monthly Notices of the Royal Astronomical Society, vol. 494, p. 3799-3827

Pandel D., Córdova F.A., 2005, Irregular Mass Transfer in the Polars VV Puppis and V393 Pavonis during the Low State, Astrophysical Journal, vol. 620, p. 416-421

Patterson J., 1979, Rapid Oscillations in Cataclysmic Variables. III. an Oblique Rotator in AE Aqr, Astrophysical Journal, vol. 234, p. 978-992

Patterson J., et al., 1982, Identification of the Bright X-ray Source 3A1148+719 with the Cataclysmic Variable YY Draconis, Bulletin of the American Astronomical Society, vol. 14, p. 618

Patterson J., 1994, The DQ Herculis Stars, Publications of the Astronomical Society of the Pacific, vol. 106, p. 209

Perryman M.A.C., et al., 2001, GAIA: Composition, formation and evolution of the Galaxy, Astronomy and Astrophysics, 369, p. 339–363

Pfleiderer J., Grewing M., 1966, Inverse Compton Effect: Some Consequences for Quasars, Science, vol. 154, p. 1452-1453

Picard A., 1991, The Large-Scale Structure of the Universe, California Institute of Technology

Pickles A.J., 1998, A Stellar Spectral Flux Library: 1150-25000 Å, Publications of the Astronomical Society of the Pacific, vol. 110, p. 863-878

Piirola V., Reiz A., Coyne G.V., 1987, Five-Colour (UBVRI) Polarimetry of H 0139-68 = BL Hydri, Astronomy and Astrophysics, vol. 185, p. 189-195

Pols O.R., 2008, Stellar Structure and Evolution

Postnov K.A., Yungelson, L.R., 2006, The Evolution of Compact Binary Star Systems, Living Reviews in Relativity volume 9, Article number: 6 (2006)

Pottasch S., 1959, The Nova Outburst: V. The Temperature and Radius of the Central Exciting Star and Observation of Elements Other than Hydrogen, Annales d'Astrophysique, vol. 22, p. 412

Potter S.B., 1999, A Multiwavelength Study Of The Accretion Region In Magnetic Cataclysmic Variables, Ph.D. Thesis, University of London

Pretorius M.L., 2004, Rapid Oscillations on Cataclysmic Variable Stars, University of Cape Town

Prialnik D., 2009, An Introduction to the Theory of Stellar Structure and Evolution, 2nd edition, Tel Aviv University, Cambridge University Press

Prieto J.L., et al., ASAS-SN and Swift Follow-Up of PSN J10081059+5150570: An Unusual Type IIn Supernova?. The Astronomer's Telegram, vol. 3749, p. 1

Pringle J.E., Wade R.A., 1985, Interacting Binary Stars, Cambridge Astrophysics Series, Cambridge, Cambridge University Press

Reese R.L., 1999, University Physics, Washington and Lee University, Brooks/Cole Publishing Company

Reid I.N., et al. 1991, The Second Palomar Sky Survey, Publications of the Astronomical Society of the Pacific, vol. 103, p. 661

Reid N., Djorgovski S., 1993, The Second Palomar Sky Survey, Sky Surveys. Protostars to Protogalaxies, Astronomical Society of the Pacific Conference Series, vol. 43, p. 125

Remillard R.A., et al., 1994, 1ES 1113+432: Luminous, Soft X-ray Outburst from a Nearby Cataclysmic Variable (AR Ursae Majoris), Astrophysical Journal, vol. 426, p. 288

Riberto F.M.A., Diaz M.P., 2007, Emission-Line Flickering from the Secondary Star in Cataclysmic Variables? A Study of V3885 Sagittarii, Astronomical Journal, vol. 133, p. 2659-2668

Ridpath I., 2012, Palomar Observatory Sky Survey (POSS), A Dictionary of Astronomy, 2nd edition, Oxford University Press

Riegler G., 1998, The International Ultraviolet Explorer Final Archive, Ultraviolet Astrophysics Beyond the IUE Final Archive, ESA Special Publication, vol. 413, p. 687

Ritter H., Kolb U., 2003, Catalogue of Cataclysmic Binaries, Low-Mass X-Ray Binaries and Related Objects (Seventh edition), Astronomy and Astrophysics, vol. 404, p. 301-303

Robertson J.K., 1941, Introduction to Physical Optics, 3rd edition

Rouan D., 2011, Johnson UBV Bandpasses, Encyclopedia of Astrobiology, p. 880

Rubinov A.V., 2004, Dynamical Evolution of Multiple Stars: Influence of the Initial parameters of the System, Astronomy Reports, vol. 48, Issue 1, p. 45-51

Rupen M.P, Mioduszewski A.J., Sokoloski J.L., 2008, An Expanding Shell and Synchrotron Jet in RS Ophiuchi, Astrophysical Journal, vol. 688, p. 559-567

Rutten R.G.M., et al,, 1994, Spectral Eclipse Mapping of the Accretion Disk in the Nova-Like Variable UX Ursae Majoris, Astronomy and Astrophysics, vol. 238, p. 441-454

Saito R.K., et al., 2010, Spectral Mapping of the Intermediate Polar DQ Herculis, Astronomical Journal, vol. 139, p. 2542-2556

Savaglio S., Grothkopf U., 2013, Swift Publication Statistics: A Comparison With Other Major Observatories, Publications of the Astronomical Society of the Pacific, vol. 125, p. 287

Scaringi S., 2015, Broad-Band Variability in Accreting Compact Objects, Acta Polytechnica CTU Proceedings, vol. 2, p. 107-110

Schmidt et al. 1996, AR Ursae Majoris: The First High-Field Magnetic Cataclysmic Variable, Astrophysical Journal, vol. 473, p. 483

Schmidt B.P., et al., 2005, The SkyMapper Telescope and Southern Sky Survey, American Astronomical Society Meeting Abstracts, vol. 206, p. 15.09

Schneider D.P., Young P., 1980, VV Puppis and AN Ursae Majoris: a Radial Velocity Study, Astrophysical Journal, vol. 240 p. 871-884

Schöder A., et al., 2009, MeerKAT Configuration Studies, Panoramic Radio Astronomy: Wide-field 1-2 GHz Research on Galaxy Evolution, p. 32

Schuerenberg B., 1989, XMM: high-throughput X-ray observatory, Astronomische Gesellschaft Abstract Series, p. 6

Schwope A., Beuermann K., 1985, Geometry and Magnetic Field of the Am-Herculis Star H:0139-68, Recent Results on Cataclysmic Variables. The Importance of IUE and Exosat Results on Cataclysmic Variables and Low-Mass X-ray Binaries, p. 173

Sekiguchi K., 1999, Prospects for Studying the Local Group with the Subaru Telescope, The Stellar Content of Local Group Galaxies, vol. 192, p. 503-507

Serway R.A, 1985, Physics for Scientists and Engineers with Modern Physics with Modern Physics, 2nd edition, James Madison University, Saunders College Publishing

Shafter A.W., 1983, On the Masses of White Dwarfs in Cataclysmic Binaries, Ph.D. Thesis, California University, Los Angeles

Shahbaz T., 2019, Polarimetry of Binary Systems: Polars, Magnetic CVs, XRBs, Astrophysics and Space Science Library, vol. 460

Shakura N. I., Sunyaev R. A., 1973, Black Holes in Binary systems. Observational Appearance, Astronomy and Astrophysics, vol. 500, p. 33

Shi, C. 2021, Compton Scattering in the Optically Thick Uniform Spherical Corona around the Neutron Star in an X-ray Binary in Two Conditions, Monthly Notices of the Royal Astronomical Society, vol. 504, p. 2961-2967

Shiao B., et al., 2014, New GALEX UV Data Products At MAST For Stellar Astrophysics, American Astronomical Society Meeting Abstracts, vol. 223, p. 441.38

Showstack R., 2007, In Brief: Reaching the end of the FUSE, EOS Transactions, vol. 88, p. 427

Silber A.D., 1992, Studies of an X-Ray Selected Sample of Cataclysmic Variables, Ph.D. Thesis, Massacusetts institute of Technology

Sion E.M., et al., 2010, The Accreting White Dwarf in SS Cygni Revealed, Astrophysical Journal, Letters, vol. 716, p. L157-L160

Skrutskie M.F., et al., The Two Micron All Sky Survey (2MASS), The Astronomical Journal, vol. 131, p. 1163–1183

Smak J.I., 1976, Spectroscopic Observations of U GEM, Structure and Evolution of Close Binary Systems, vol. 73, p. 149

Smith R.C., 2007, Cataclysmic variables, University of Sussex

Stover R.J., et al., 1980, Time Resolved Spectroscopy of Cataclysmic Variables : SS Cyg, Astrophysical Journal, vol. 240, p. 597-607

Suzuki T.P., 2013, Evolution of Solar-Type Stellar Winds, Astronomische Nachrichten, vol. 334, p. 81-84

Tapia S., 1977, Discovery of a Magnetic Compact Star in the AM Herculis / 3U 1809+50 System, Astrophysical Journal, vol. 212, p. L125-L12

Tapia S., 1977, VV Puppis, International Astronomical Union Circulars, vol. 3054, p. 1

van Teeseling A., Verbunt F., 1994, ROSAT X-Ray Observations of Ten Cataclysmic Variables, Astronomy and Astrophysics, vol. 292, p. 519-533

Thompson et al., 1980, The Very Large Array, Astrophysical Journal, Supplement, vol. 44, p. 151-167

Thorstensen J.R., Wade R.A., Oke J.B., 1986, A Spectroscopic Study of the Cataclysmic Binary Star SU Ursae Majoris, Astrophysical Journal, vol. 309, p. 721

Thorstensen J.R., 2003, Parallaxes and Distance Estimates for 14 Cataclysmic Variable Stars, Astronomical Journal, vol. 126, p. 3017-3029

Toone J., 2012, The Extraordinary Flickering Behaviour of U Geminorum, Journal of the British Astronomical Association, vol. 122, p. 279-283

Tryka S., 1997, Angular Distribution of the Solid Angle at a Point Subtended by a Circular Disk, Optics Communications, vol. 137, p. 317-333

Trümper J., 1982, The ROSAT Mission, Advances in Space Research, vol. 2, p. 241-249

Trümper J., 1999, Highlights from the ROSAT Years, High Energy Astrophysics Division, vol. 4, p. 25.01

Tryon E.P., 2003, Cosmic Inflation, Encyclopedia of Physical Science and Technology (Third Edition)

Turon C., 1995, GAIA: A New Era for Cosmic Distance Scale Determination, Observatorie de Paris-Meudon

Tylenda R., 1981, Radiation from Optically Thin Accretion Discs, Acta Astronomica, vol. 31, p. 127

Unda-Sanzana E., 2005, A spectroscopic analysis of three cataclysmic variable stars, Ph.D. Thesis, University of Southampton, United Kingdom

Unda-Sanzana E., Marsh T.R. Morales-Rueda L., 2006, Optical Spectroscopy of the Dwarf Nova U Geminorum, Monthly Notices of the Royal Astronomical Society, vol. 369, p. 805-818

Urban J.A., Sion E.M., 2006, The Dwarf Novae during Quiescence, Astrophysical Journal, vol. 642, p. 1029-1041

Vande Putte D., et al., 2003, A Spectroscopic Search for Faint Secondaries in Cataclysmic Variables, Monthly Notices of the Royal Astronomical Society, vol. 342, p. 151-162

Vaytet N.M.H., O'Brien T.J., Rushton A.P., 2007, Evidence for ablated flows in the shell of the nova DQ Herculis, Monthly Notices of the Royal Astronomical Society, vol. 380, p. 175-180

Visvanathan N., Pickles A., 1982, Optical Identification of X-ray Source H0139 - 68 with an AM Herculis-type System, Nature, vol. 298, p. 41-44

Visvanathan N., Bessell M.S., Wickramasinghe D.T., 1984, H0139-68, International Astronomical Union Circulars, vol. 3923, p. 2

Vogt N., Krzeminski W., Sterken C., 1980, Periodic and Secular Variations in the lightcurve of Dwarf Nova EX Hya, Astronomy and Astrophysics, vol. 85, p. 106-112

Vuillaume T., Henri G. Petrucci P., 2012, Anisotropic inverse Compton process in the vicinity of an accretion disk, High Energy Gamma-Ray Astronomy: 5^{th} International Meeting on High Energy Gamma-Ray Astronomy, American Institute of Physics Conference Series, vol. 1505, p. 669-672

Wade R.A., 1979, A Spectrophotometric Parallax for U Geminorum, Astronomical Journal, vol. 84, p. 562-566

Walker M.F., 1965, New Observations of AE Aquarii, Sky and Telescope, vol. 29, p. 23

Walker R., 2017, Spectroscopic Binaries, Spectral Atlas for Amateur Astronomers: A Guide to the Spectra of Astronomical Objects and Terrestrial Light Sources, Cambridge University Press, p. 123–131

Walton N.A., et al., 2004, IPHAS: The INT/WFC Photometric H-alpha Survey of the Northern Galactic Plane, American Astronomical Society Meeting Abstracts, vol. 205, p. 133.03

Warner B., Odonoghue D., Allen S., 1985, Rapid oscillations in CPD -48 1577, Monthly Notices of the Royal Astronomical Society, vol. 212, p. 9P-13

Warner B., 1995, Cataclysmic Variable Stars. Cambridge University Press, Cambridge

Warren S., 2002, Scientific goals of the UKIRT Infrared Deep Sky Survey, Survey and Other Telescope Technologies and Discoveries, Society of Photo-Optical Instrumentation Engineers (SPIE) Conference Series, vol. 4836, p. 313-320

Watson C.A., Dhillon V.S., Shahbaz T., 2006, Roche Tomography of Cataclysmic Variables - III. Star-Spots on AE Aqr, Monthly Notices of the Royal Astronomical Society, vol. 386, p. 637-650

Weiler E.J., Stencel R.E., 1982, A Far Ultraviolet Spectroscopy Explorer (FUSE), Bulletin of the American Astronomical Society, vol. 14, p. 883

Welsh W.F., Horne K., Gomer R., 1998, Doppler Signatures of Hα Flares in AE Aquarii, Monthly Notices of the Royal Astronomical Society, vol. 298, p.285-302

Werner W.M., et al., 2004, The Spitzer Space Telescope Mission, The Astrophysical Supplement Series, vol. 154, p. 1-9

West S.C., Berriman G., Schmidt G.D., 1987, The Discovery of Near-Infrared Polarized Cyclotron Emission in the Intermediate Polar BG Canis Minoris, The Astrophysical Journal Letters, vol. 32, p. L35

White N.E, Holt S.S., Accretion Disk Coronae, NASA STI/Recon Technical Report N, p. 20106

Williams R.E., 1980, Emission Lines from the Accretion Disks of Cataclysmic Variables, The Astrophysical Journal, vol. 235, p. 939-944

Wolff M.T., et al., 1999, X-ray and Optical Observations of BL Hydri, Astrophysical Journal, vol. 526, p. 435-444

Wolf M., 1924, Astronomische Nachrichten, vol. 220, p. 255

Wood J.H., et al., 1995, The Discovery of an X-ray Eclipse during a Low State of the Dwarf Nova HT Cassiopeiae, Monthly Notices of the Royal Astronomical Society, v. 273, p. 772-784

Woudt P., 2021, ThunderKAT and MeerLICHT: a multi-wavelength study of astrophysical transients, Conference of the African Astronomical Society, p. 35

Wright E.L., et al., 2010, The Wide-Field Infrared Survey Explorer (WISE): Mission Description and Initial On-Orbit Performance, The Astronomical Journal, 140:1868–1881

York D.G., et al., 2000, The Sloan Digital Sky Survey: Technical Summary, The Astronomical Journal, vol. 120, p. 1579-1587

Zead I., et al., 2017, Spectral and Photometric Behavior of SU UMa During Quiescence and Outburst States, New Astronomy, vol. 52, p. 122-132

Zhang L., Cheng K.S., 1997, Gamma-Ray Production through Inverse Compton Scattering with Anisotropic Photon Field from Accretion Disk in AGNs, Astrophysical Journal, vol. 488, p. 94-108

Zinner E., 1938, Mitteilungen über veränderliche und verdächtige Sterne, Astronomische Nachrichten, vol. 265, p. 345